NASA/TM–202300012644

# A Summary of Structural Test and Simulation Results for Hawker 4000 Composite Fuselage Hardware

*Justin D. Littell, Jacob B. Putnam, and Nathaniel W. Gardner*
*Langley Research Center, Hampton, Virginia*

December 2023

# NASA STI Program Report Series

Since its founding, NASA has been dedicated to the advancement of aeronautics and space science. The NASA scientific and technical information (STI) program plays a key part in helping NASA maintain this important role.

The NASA STI program operates under the auspices of the Agency Chief Information Officer. It collects, organizes, provides for archiving, and disseminates NASA's STI. The NASA STI program provides access to the NTRS Registered and its public interface, the NASA Technical Reports Server, thus providing one of the largest collections of aeronautical and space science STI in the world. Results are published in both non-NASA channels and by NASA in the NASA STI Report Series, which includes the following report types:

- TECHNICAL PUBLICATION. Reports of completed research or a major significant phase of research that present the results of NASA Programs and include extensive data or theoretical analysis. Includes compilations of significant scientific and technical data and information deemed to be of continuing reference value. NASA counterpart of peer-reviewed formal professional papers but has less stringent limitations on manuscript length and extent of graphic presentations.

- TECHNICAL MEMORANDUM. Scientific and technical findings that are preliminary or of specialized interest, e.g., quick release reports, working papers, and bibliographies that contain minimal annotation. Does not contain extensive analysis.

- CONTRACTOR REPORT. Scientific and technical findings by NASA-sponsored contractors and grantees.

- CONFERENCE PUBLICATION. Collected papers from scientific and technical conferences, symposia, seminars, or other meetings sponsored or co-sponsored by NASA.

- SPECIAL PUBLICATION. Scientific, technical, or historical information from NASA programs, projects, and missions, often concerned with subjects having substantial public interest.

- TECHNICAL TRANSLATION. English-language translations of foreign scientific and technical material pertinent to NASA's mission.

Specialized services also include organizing and publishing research results, distributing specialized research announcements and feeds, providing information desk and personal search support, and enabling data exchange services.

For more information about the NASA STI program, see the following:

- Access the NASA STI program home page at http://www.sti.nasa.gov

- Help desk contact information:

https://www.sti.nasa.gov/sti-contact-form/
and select the "General" help request type.

NASA/TM–202300012644

# A Summary of Structural Test and Simulation Results for Hawker 4000 Composite Fuselage Hardware

*Justin D. Littell, Jacob B. Putnam, and Nathaniel W. Gardner*
*Langley Research Center, Hampton, Virginia*

National Aeronautics and
Space Administration

Langley Research Center
Hampton, Virginia 23681-2199

December 2023

Available from:

NASA STI Program / Mail Stop 148
NASA Langley Research Center
Hampton, VA  23681-2199
Fax: 757-864-6500

# Table of Contents

# Table of Figures

# Introduction

The increased use of composite materials for aircraft primary structure such as fuselage skin, stringer and frame sections necessitate a complete understanding of their material properties under expected operational and emergency conditions. Material behavior specific to dynamic events such as hard or crash landings is important to understand due to the differences in composite performance when compared to traditional metallic aircraft components. Because of this intrinsically different behavior, data sets for composite aircraft structures undergoing dynamic loading are necessary for both their design and analysis. There is some data available on composite structures undergoing impact conditions [1], however, data on large scale aircraft components utilizing composite materials are still uncommon in the public domain and therefore testing on composite aircraft structures is still needed to expand current data sets.

Within the NASA Revolutionary Vertical Lift Technology (RVLT) Project, there is ongoing research to characterize advanced composite structures undergoing dynamic loading through the use of full- and sub-scale testing, while also using the resultant dynamic test data to generate calibrated and validated composite material models for use in computational finite element (FE) computer codes. The project expects to obtain these objectives through a variety of test and analysis programs.

NASA Langley Research Center (LaRC) was able to obtain a partially fabricated Hawker Beechcraft Model 4000 (Hawker 4000) aft aircraft section to use for study. The Hawker 4000 is a medium sized business jet (14 Code of Federal Regulations Part 25 – Transport Category Aircraft) with seating for 8 to 14 people and fabricated out of carbon composite. The Hawker 4000 was designed in the early 2000s to compete with Gulfstream and Bombardier business jet units. The Hawker Beechcraft business unit declared bankruptcy in 2012, and abruptly halted production of the 4000 series aircraft. As a result, only 73 full production aircraft were built [2].

This all-composite aft fuselage section was an ideal candidate to utilize for investigations of composite structures undergoing dynamic loading in order to satisfy RVLT project objectives. Thus, a team at NASA LaRC embarked on a test and simulation program in late 2021 in order to generate test data of composite structures undergoing dynamic loading conditions. As a part of these investigations, methods including reverse engineering the geometry, conducting as-fabricated materials testing and using non-destructive evaluation (NDE) techniques such as ultrasonic through transmission were utilized in order to develop digital twin finite element models for use in computational simulations.

# Test Article Overview

The test article began as an aft section of a Hawker 4000 fuselage which was donated to NASA LaRC in 2015. The test article was transported to the Landing and Impact Research (LandIR) Facility in 2018 for storage while the formulation of the test and analysis program began. The section starts at approximately fuselage station 414 and ends at the tail of the aircraft. The interior is bare of components other than metallic mounting brackets intended to hold avionics and other equipment. Furthermore, there is no subfloor or seats present, so it represents a finished outer shell but unconfigured aircraft section. An exterior view of the Hawker 4000 fuselage aft section, resting in its transport trolley is shown in Figure 1.


Figure 1 - Hawker 4000 aft section exterior view.

## Objectives

The test article did not have any interior components which could be used to conduct detailed tests utilizing seats and anthropomorphic test devices (ATDs, a.k.a. crash test dummies) to evaluate the extent of occupant injury. In this way, the test article differed from the one used at the National Institute for Aviation Research (NIAR) in 2018 [3]. This program, instead, focused on utilizing the aft section as a testbed to generate test data for the examination of full-scale composite response subject dynamic loading and failure. Specifically, the program was formulated to accomplish the resultant objectives:

1. Generate dynamic composite impact test data for use in material model correlations. The test data were generated from two full-scale drop tests of instrumented subsections of the test article. The data were primarily acquired from sensors measuring impact accelerations and loads, along with displacements and strains determined from photogrammetric techniques. The mixture of sensor and camera data provided a comprehensive picture of the performance of the test article undergoing a dynamic loading event.

2. Develop and evaluate techniques including reverse engineered methods, as-built materials testing and other non-destructive techniques to create computational digital twins used for simulations. The evaluation of the techniques used to develop reverse engineered computer models of the test article was also an important item to study. When creating computational models of large structures, there are necessary considerations to determine the amount of detail required to accurately simulate a given loading condition. Considerations specific to simulations of composite material structures typically include constituent material property characterization, the handling of composite layer representation, delamination, failure criteria, and mesh quality. The determination

of these parameters is often based on established modelling techniques, the fidelity needed, the test data available, and the analyst's experience.

To expand on the subject of model fidelity, the amount of fidelity needed in the model is highly dependent on what is being sought from the model results. The goal of this study was not necessarily to capture all of the delamination and failure mechanisms occurring at a microscale level, but rather to create a model capable of capturing the failure mechanisms at a macroscopic level with accurate prediction of acceleration and loads throughout the structure. This type of information is important because simulations of large-scale aircraft structures under impact events at NASA LaRC [4] [5] are typically conducted to evaluate the energy absorption capabilities and ultimately the amount of injury an onboard occupant would experience under a particular loading condition. Thus, if acceleration levels, failure propagation, and overall deformations are similar between the test and the simulation, a degree of confidence is established in the model results for the prediction of overall response and ultimately occupant protection, even if some of the microscale structural behaviors may not be entirely comparable.

Model development relied heavily on a combination of NDE, photogrammetry, and component level material property characterization and full-scale testing data, all of which will be described in the following sections.

## Test Article Inspections

The Hawker 4000 was visually inspected to determine whether there was any delamination, tears, punctures, or other notable defects to document prior to the beginning of the test campaign. Visual inspections indicated that the test article did not contain known visible damage to the structure itself. However, the vehicle structure did contain manufactured features which are documented in the following figures. An overall interior view is shown in Figure 2.

Figure 2 - Hawker 4000 interior view.

There were two large holes on the belly in the foreground of the picture are noted, along with a large square hole on the right side of the picture. There are other numerous smaller holes that are also present, which were also made at the time of manufacture.

Examining the interior in more detail, some of the metallic brackets that were installed via rivets at the time of manufacture can be seen. In addition, a series of small metallic studs were bonded onto the interior skin prior research programs, and not present at manufacture. However, these studs did not penetrate the interior skin and therefore were assumed to not affect the overall material response. The studs can be identified by the orange circular base, and a silver numbering scheme present next to the base. All brackets and studs remained in the articles when conducting the testing. A detailed interior view is shown in Figure 3.

Figure 3 - Hawker 4000 interior close up.

Additionally, based on the visible inspections, it was determined the fuselage section was fabricated using a sandwich construction and the materials appeared similar throughout out the entire section. However, there were notable thickness differences in spots.

There was a flange approximately 2 inches wide at the forward end of the section. The flange appeared to be entirely fabricated of carbon layers, though the exact number was not determined, and the thickness measurements varied around the perimeter. The flange can be seen in Figure 2 and Figure 3, however is also highlighted in Figure 4 for clarity.

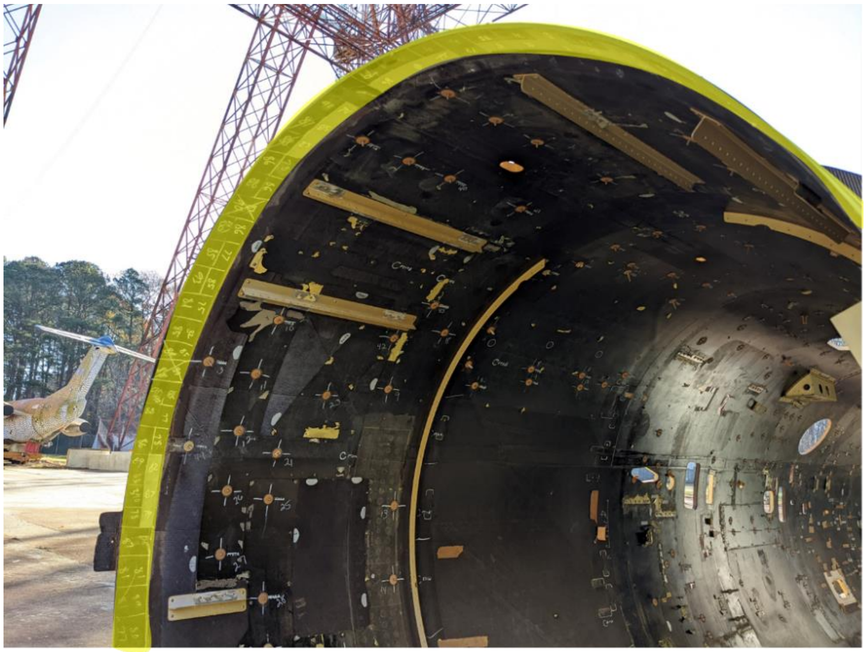

Figure 4 - Hawker 4000 forward composite flange highlighted.

Finally, the visual inspections revealed that there was a filled honeycomb sandwich core around most of the manufactured openings, and it appeared the sandwich material was the same color and density throughout the section where it was visible. A close-up view of the interior filled honeycomb sandwich material is shown in Figure 5.

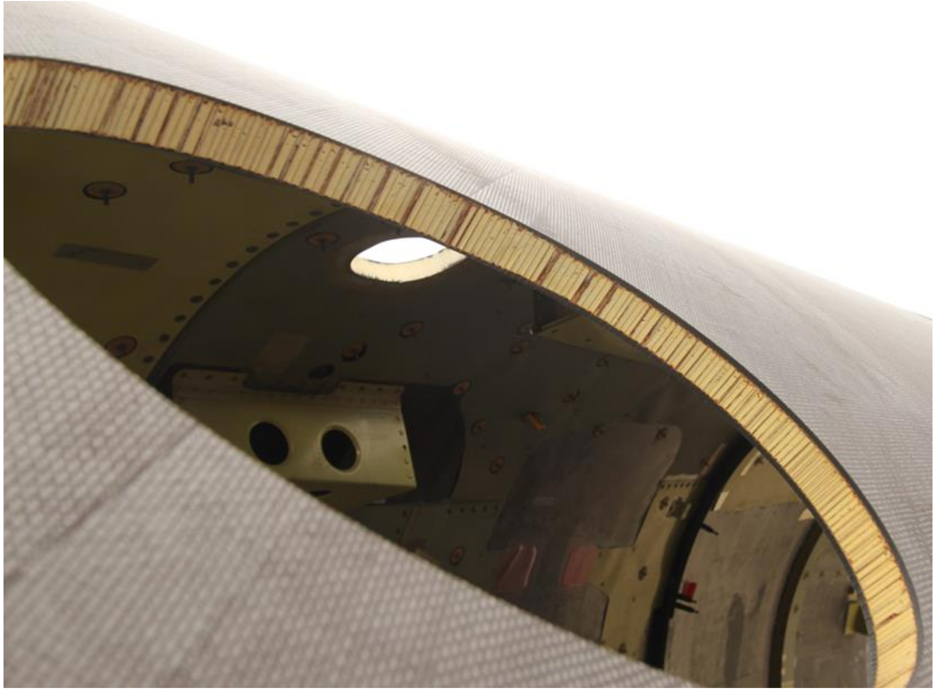

Figure 5 - Honeycomb sandwich core close up.

The test article was scanned using three-dimensional (3D) point cloud scanning techniques to create point clouds of both the exterior and interior of the test article as it was resting in its cradle. The point cloud scans provided both a documented "before" condition of the Hawker 4000, but also provided the baseline geometry for the creation of the computer models. The scans were completed outside at the LandIR facility in December of 2021.

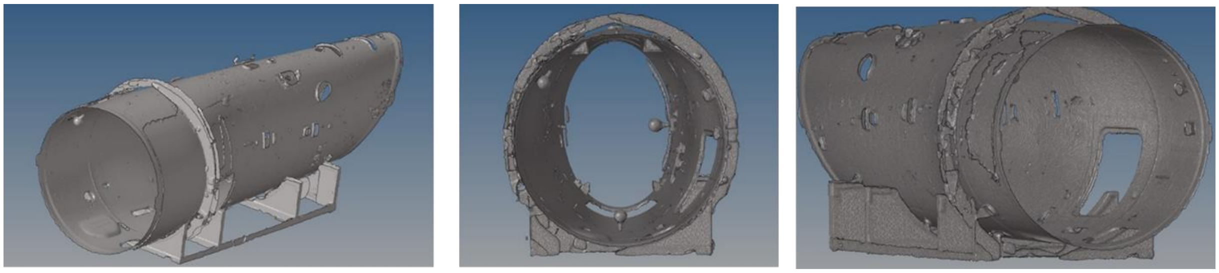

Figure 6 - Point cloud scan results. Iso-port view (left), front view (middle) and Iso-starboard view (right).

## Full-Scale Test Section Development

After the inspections were completed, the test article was sectioned into three pieces. The first piece was cut approximately 87 inches behind the forward flange, which created the Forward Section. The second cut was approximately 100 inches from the aft end, which created the Aft Section. The remaining section was an approximate 80-inch long section between the two, named the Middle Section. The Forward and Aft Sections were used for full-scale drop testing, while the leftover Middle Section was used for materials characterization testing. Since it was assumed the entire fuselage section was similar in design and construction, the material properties obtained from the tests from the middle section would be input into the Forward and Aft Section computer models.

Next, the three sections were moved to their respective preparation areas. The Forward Section was removed from the cradle, weighed and then placed in the shop for buildup. The empty weight of the test article was 299 lb. The Forward Section removal is shown in Figure 7.

Figure 7 - Forward Section test article.

Next the Aft Section was cut and removed from the test article. This section was not weighed, however, and was placed into the shop area next to the Forward Section. The Aft Section is shown in Figure 8. The Middle Section was moved to a separate building to be further sectioned into smaller test specimens.


Figure 8 - Aft Section test article.

Prior to the addition of sensors or ballast to the Forward Section necessary for the full-scale dynamic test, a series of ultrasonic through transmission (UTT) scans were conducted to determine the areas where the honeycomb sandwich with both filled and unfilled since the sectioning of the test article revealed interior locations where not all of the interior honeycomb sandwich was filled. In order to accurately simulate the test article and test, a map depicting the locations of the filled and unfilled locations in the test article was necessary.  This map was generated by utilizing an UTT transducer at discrete points around the Forward Section.  First, the entire exterior was painted white, and then UTT data were taken at a density of a grid with 12-inch spacing, with measurement density increasing when locating closer to the openings.  A filled section from the UTT scans was determined by examination of the waveform through an oscilloscope and determining if wave reflection occurred.  A measurement of a wave reflection at the far facesheet represented a filled section, while an unfilled section did not produce a wave reflection at the far facesheet. The nominal 12-inch spaced measurement grid is shown in Figure 9.

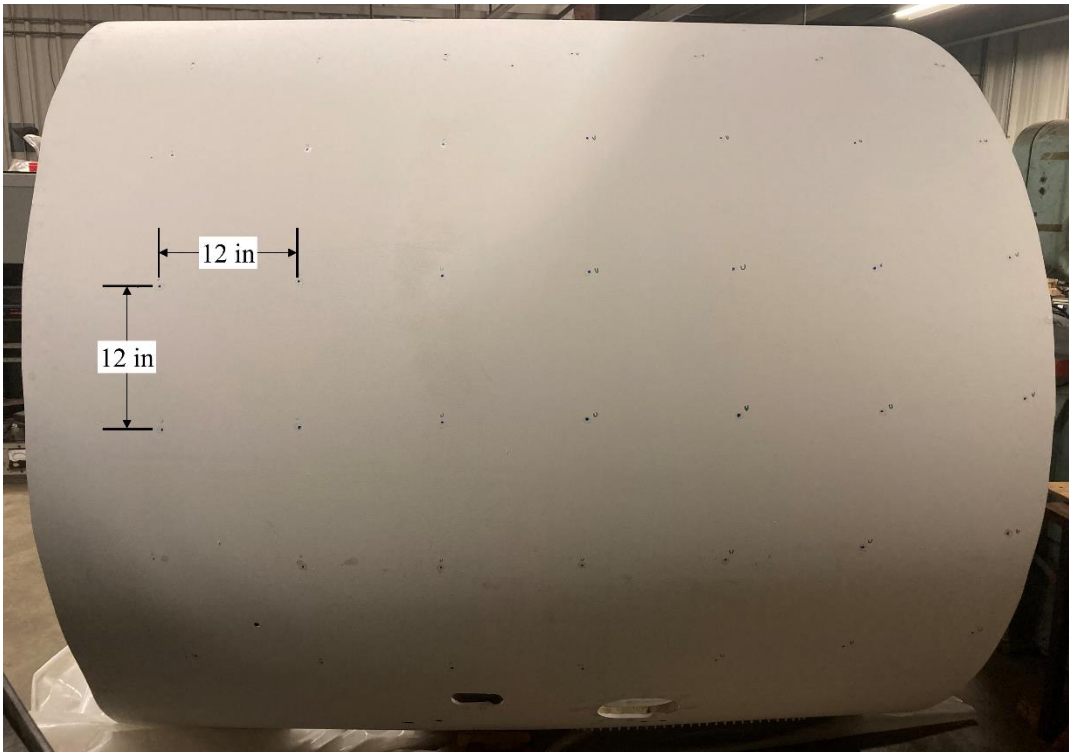

Figure 9 - UTT measurement grid layout.

The collected oscilloscope data is shown in Figure 10, noting that the waveform located below the green marker shown on the display indicates reflection at the far facesheet.

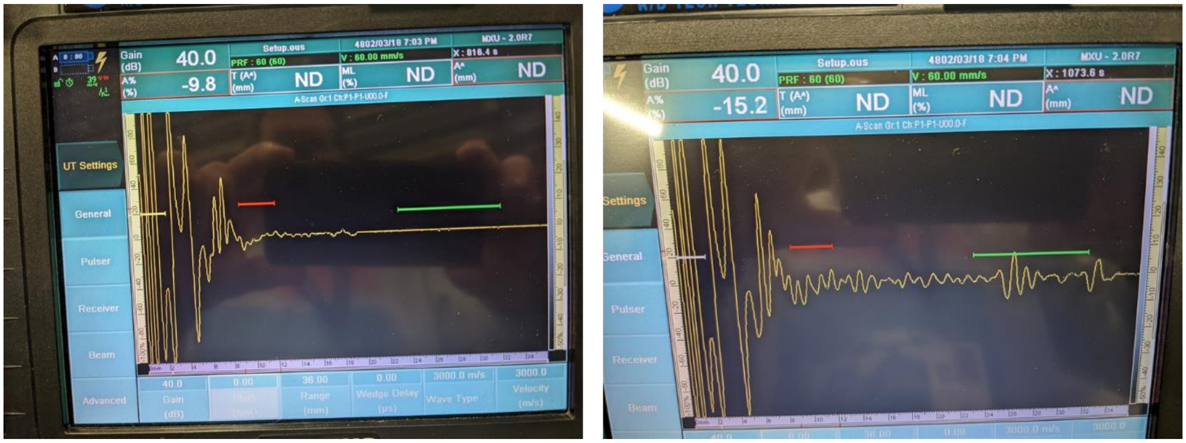

Figure 10 - UTT oscilloscope data.  Unfilled (left) and filled (right) measurements.

After point measurements were made, the general trend emerged showing that filled honeycomb was primarily around the factory created openings in the fuselage, presumably to add some structural reinforcement at these locations. The area of the honeycomb that was filled was typically on the order of 1 inch around the holes, though the measurement positions were not precise. Where a filled honeycomb measurement occurred, the skin was marked, and then the marks were interpolated to show the picture of the fill. An example filled honeycomb measurement around a factory produced opening is shown in Figure 11. These locations were documented and used as references for building up the computational models.

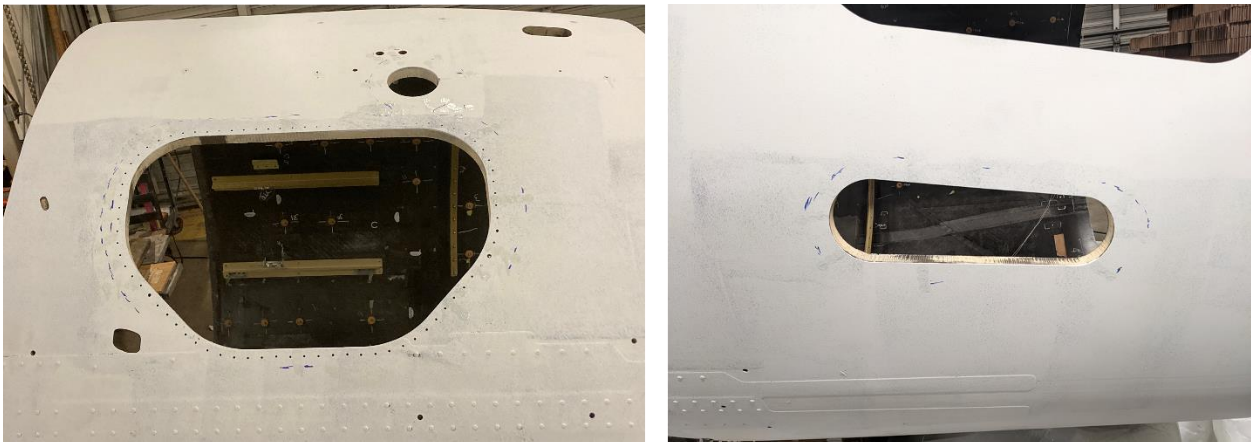

Figure 11 – Filled honeycomb around factory produced openings in the Forward Section (left) and Aft Section (right).

Once the scans were completed, both sections remained in storage until the materials test program was completed. The material test program utilized the left-over Middle Section, with specimens being removed for component level static and dynamic testing. This testing is described in the next *Component Level Materials Testing* section.

## Component Level Materials Testing

All components were removed from the left-over Middle Section, with the exception of a 2-inch-wide ring around the forward end of the Forward Section. This flange was unique because it was the only area on the entire test article that was comprised of a solid composite (without sandwich honeycomb) material. Four specimens were cut of this ring and cut into curved rectangular specimens ranging between 14.3 inches to 14.9 inches long and nominally 2 inches wide. They were removed from various locations on the flange to produce a data from a variety of locations around the circumference of the structure. Two of the specimens, 8176, and 8278 are shown in Figure 12.

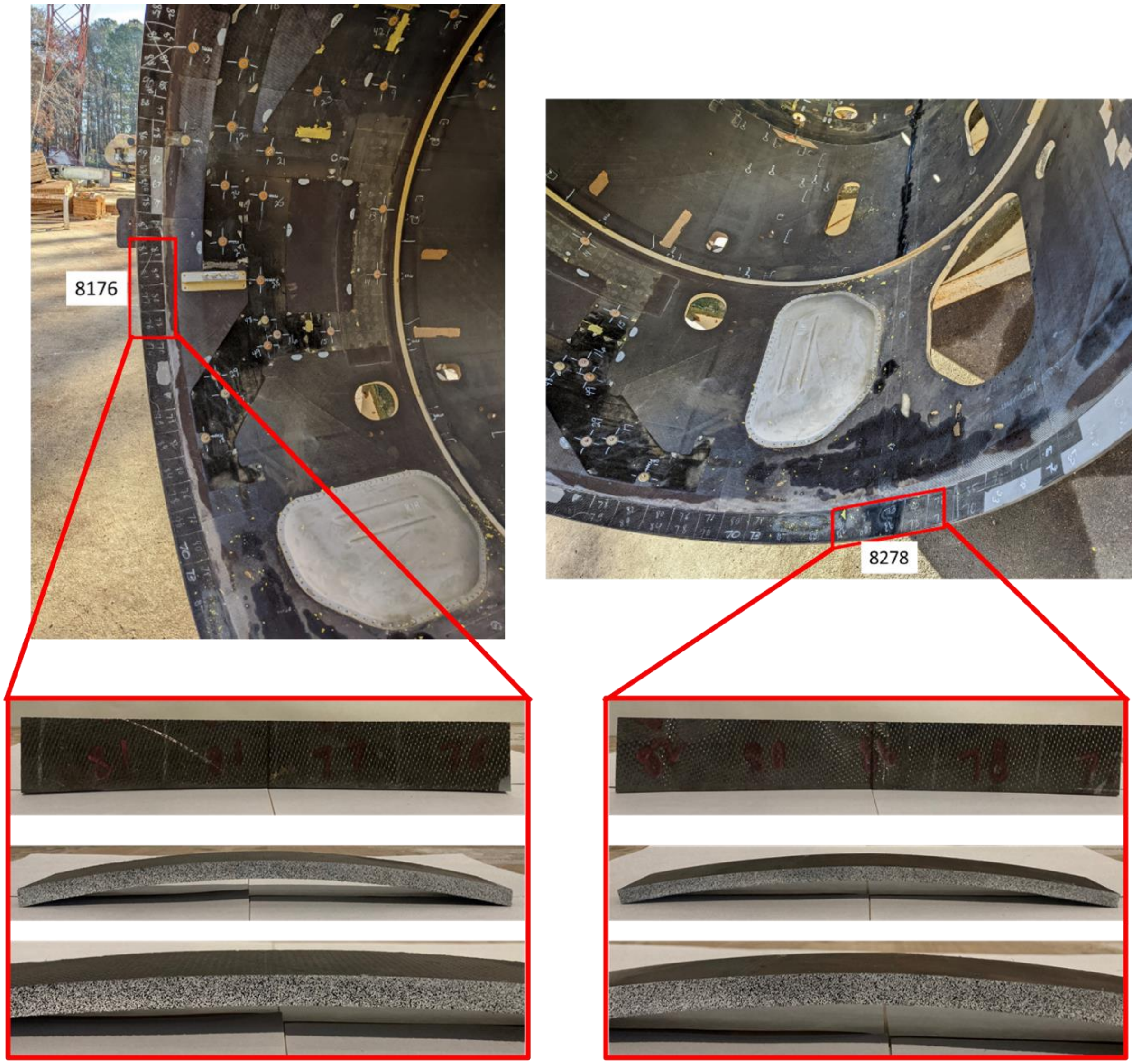

Figure 12 – Flange three-point bend specimens 8176 (left) and 8278 (right).

The other two specimens, 7479 and 7088 are shown in Figure 13. Four specimens were used to allow for one repeat for two separate test conditions.

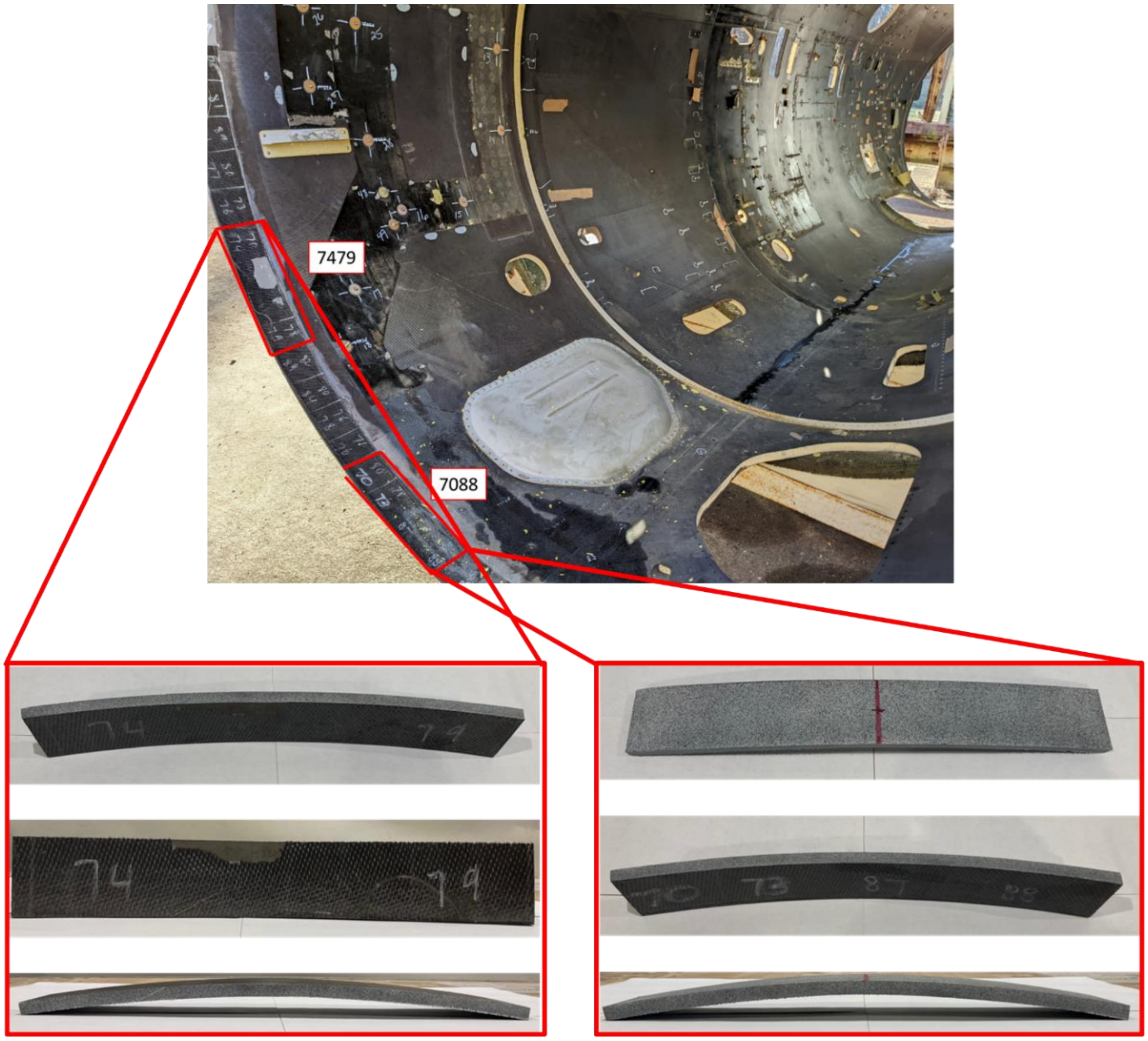

Figure 13 – Flange three-point bend specimens, 7479 (left) and 7088 (right).

## Solid Flange Static Three-Point Bend Tests

Samples 8176 and 8278 were tested under a “convex” configuration where the arch of the specimen was pointed downward, while samples 7479 and 7088 were tested in a “concave” configuration where the arch of the specimen was pointed upward. A high-contrasting, random speckle pattern was applied to the side and top of each test article for use with three-dimensional digital image correlation (DIC) during the test, and specimens were all measured prior to testing. The measurements are shown in Table 1.

Table 1 – Flange three-point bend specimen dimensions.

| Specimen | Test | Avg. Length (in.) | Avg. Width (in.) |
|---|---|---|---|
| 8176 | Convex | 14.250 | 2.063 |
| 8278 | Convex | 14.875 | 2.072 |
| 7479 | Concave | 14.438 | 2.002 |
| 7088 | Concave | 14.375 | 2.001 |

A static shape measurement was completed on all specimens so the simulation models could be made as accurate as possible. The shape measurement for specimen 7088 is shown in Figure 14 as an example.

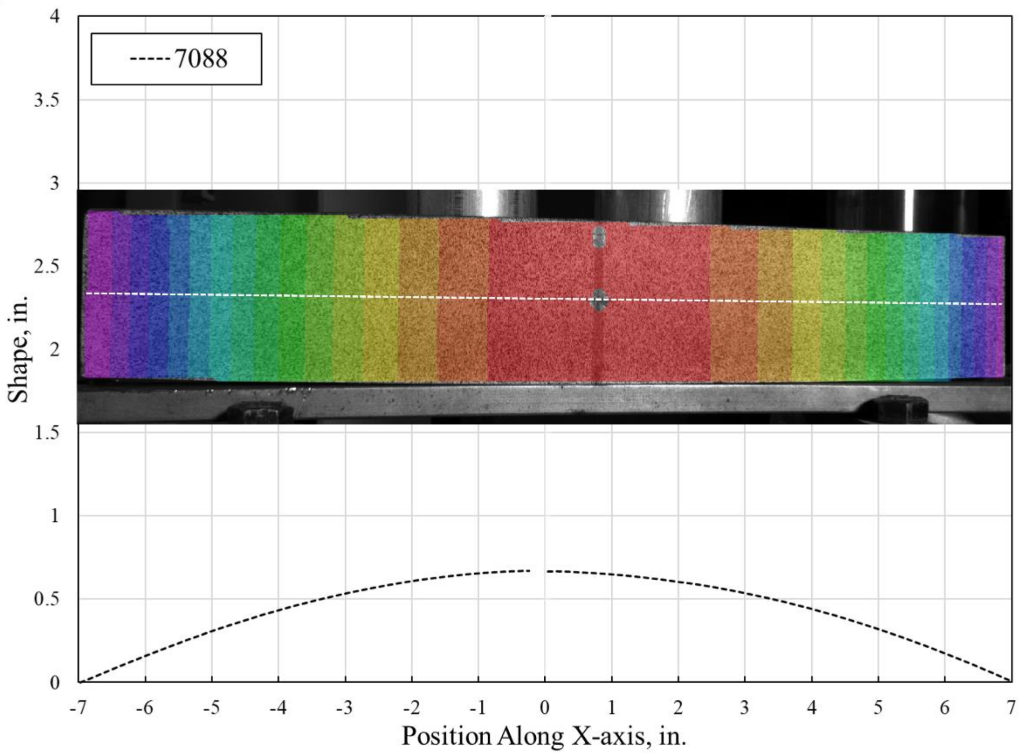

Figure 14 - Shape measurements on three-point bend specimen 7088.

The specimens were tested on an MTS servo hydraulic test machine with a three-point bend test fixture. The test fixture consisted of two 2-in diameter rollers spaced 12 inches apart, with a 1-in fixed roller in the middle. The loading rate was 0.25 in./min. up to a maximum displacement of 3 in. A convex test setup is shown in Figure 15.

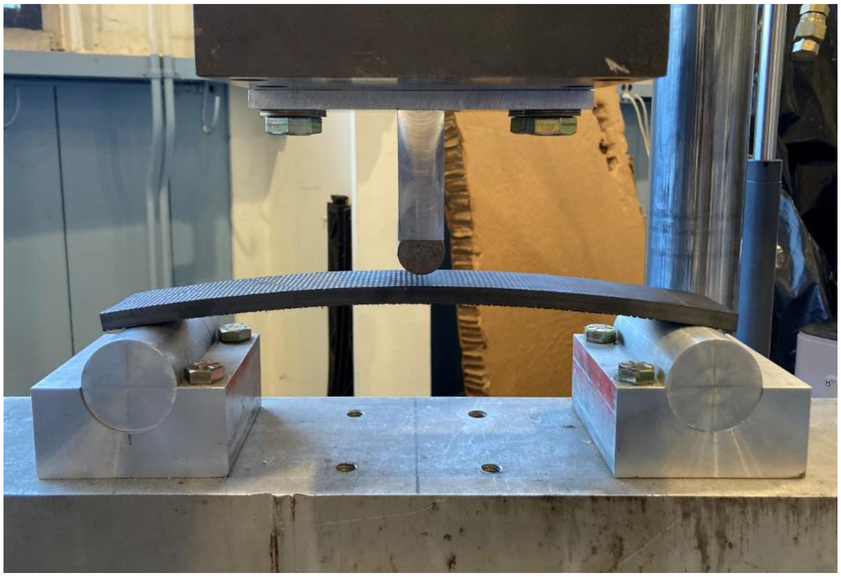

Figure 15 – Static three-point bend convex test setup.

Load and displacement data were collected from the MTS machine itself along with the 3D-DIC deformation and strain measurements acquired from the side of the specimen. These measurements verified MTS stroke, but also provided for a greater insight into the bending characteristics of the specimen, along with flagging areas of failure during the later time history in the test. The time history of the load-displacement results of the testing are shown in Figure 16.

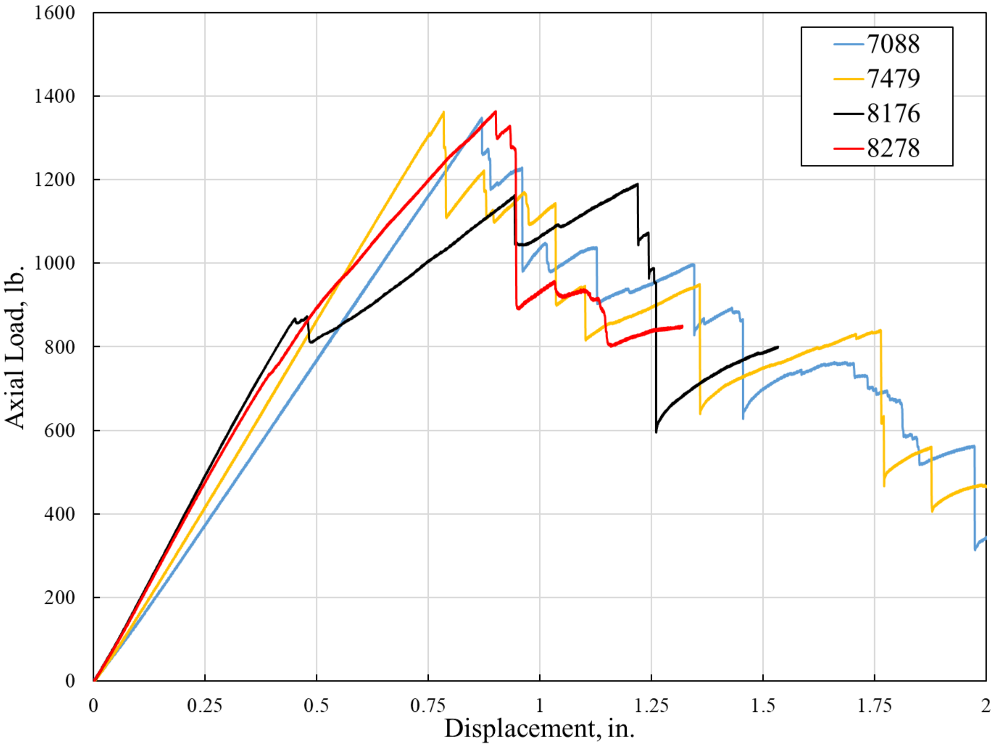

Figure 16 – Flange three-point bend results.

Upon examination of the data, three of the four specimens exhibited similar maximum load, with values of 1358 lb., 1348 lb. and 1364 lb. for specimens 7479, 7088 and 8278, respectively. Only specimen 8176 fell out of family, which was likely due to a failure occurring early in the loading history, which is shown as an abrupt change in loading stiffness at the approximate 0.4-in. loading mark. The bending stiffness for concave specimens 7479 and 7088 were similar and primarily linear until failure occurred. The slope was 1566 lb./in. for 7088 and 1768 lb./in. for 7479. The slopes in both convex specimens showed a distinct change around the 0.4 in loading mark, with specimens 8176 experiencing some type of failure at this point. Slopes prior to this point were 1989 lb./in. and 1905 lb./in. for specimens 8176 and 8278, respectively.

The maximum displacement contour plot just prior to the initial damage/failure and subsequent load drop observed in Figure 16 is shown in Figure 17 for Specimen 8278. The displacement in the specimen is uniform and symmetric which is denoted by an examination of the color iso-lines.

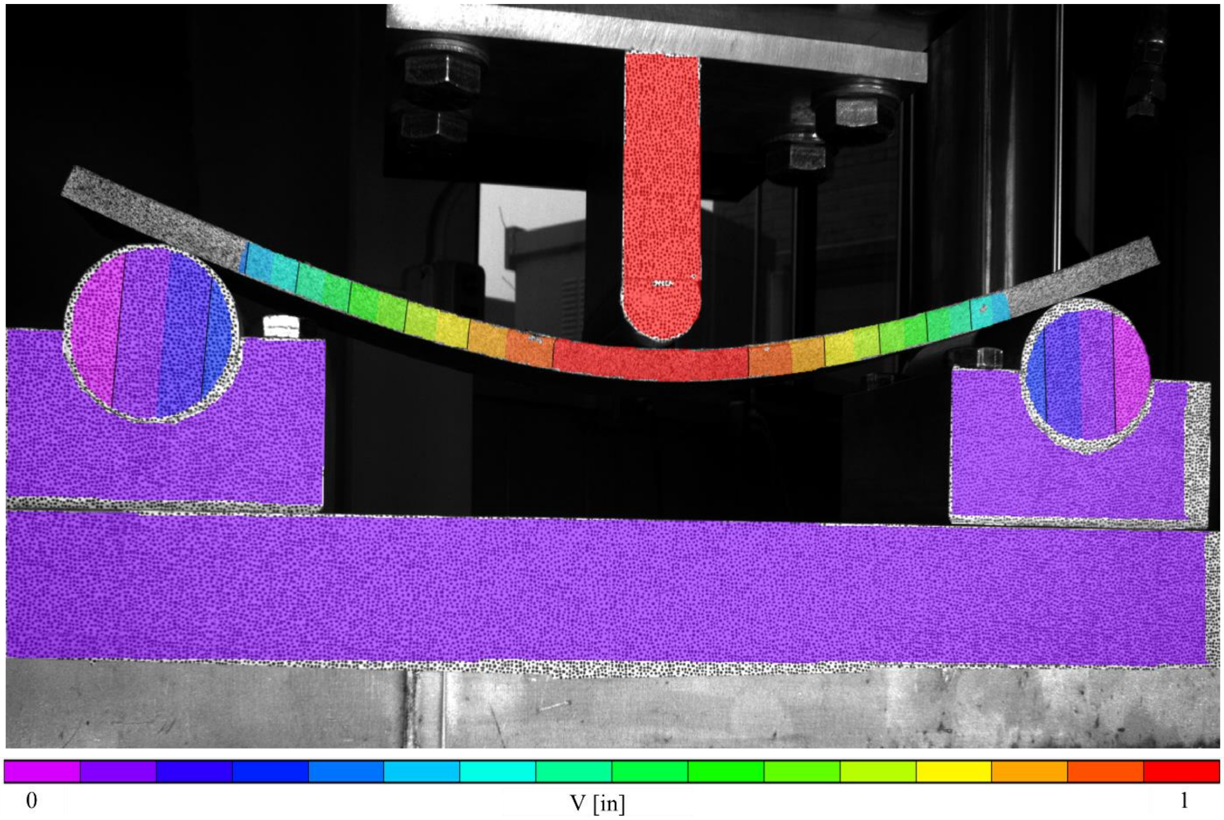

Figure 17 – Maximum displacement just prior to initial damage (Convex – 8278).

The corresponding axial bending strain, εxx, just prior to the load drop (initial damage) is shown in Figure 18. After the peak load, all specimens exhibited a “stair step” type of behavior where the load would stagger downward in defined steps toward zero. The strain developed in the specimen was primary on the outer edges, which was due to the bending loading condition. The initial damage appeared in the upper edge of the specimen, which exhibited compressive (negative) strain, while the lower edge exhibited tensile (positive) strain. The strain distribution was approximately equal and opposite between the upper and lower edges, with a zero-strain neutral axis in the middle.

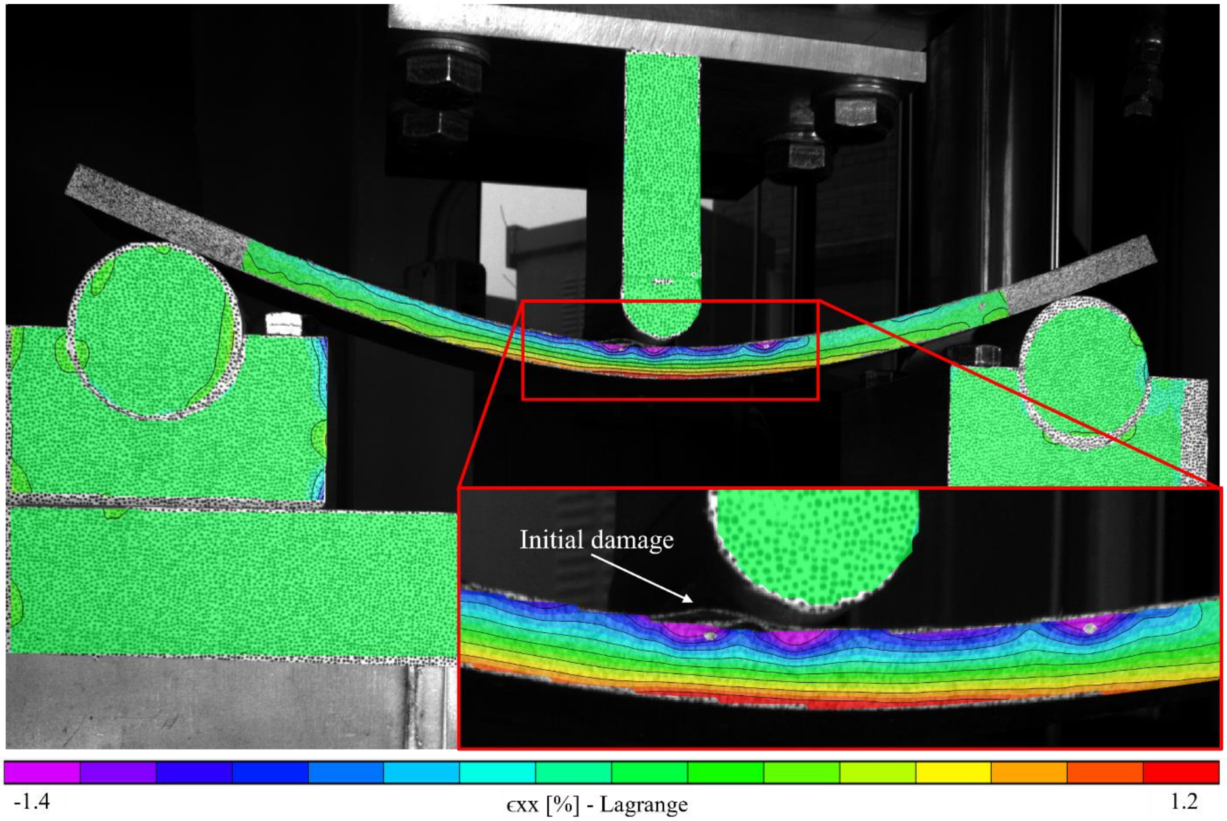

Figure 18 – Maximum axial bending strain, εxx, just after initial damage (Convex – 8278).

The delaminations in the specimen are shown in Figure 19. The upper portion of the specimen contains all of the visible damage from the test. The top layers show fiber failure due to the compressive loading. The bottom of the specimen appears to still be intact after the test.

Figure 19 – Close-up view of failure location and interlaminar damage (Convex – 8278).

The next set of specimens tested were of the sandwich core material itself. Both filled and unfilled honeycomb core sections were removed out of the Middle Section for use in materials testing. The testing of these specimens was divided into two parts. The first was compressive tests of the core material (both filled and unfilled) itself, and the second was additional three-point bending testing of longer curved specimens which were all unfilled, similar to the tests conducted on solid flange specimens.

## Sandwich Core Three Point Bend Static Tests

The unfilled core sandwich specimens were cut to the approximate dimension of the solid composite specimens. The measurements are shown in Table 2.

Table 2 – Sandwich three-point bend specimen dimensions (Unfilled core).

| Specimen | Test | Avg. Length (in.) | Avg. Width (in.) |
|---|---|---|---|
| 1 | Sandwich-Concave | 15.250 | 2.004 |
| 2 | Sandwich-Concave | 16.563 | 2.012 |
| 3 | Sandwich-Concave | 14.375 | 1.999 |
| 5 | Sandwich-Concave | 16.375 | 1.972 |

For the three-point bend of the unfilled core sandwich specimens, an identical loading rate and displacement was used as that used above on the flange specimens (0.25 in./min. up to a maximum displacement of 3 inches) on the same fixturing on the same testing machine also utilizing digital image correlation techniques to gather strain and displacement data. The test setup is shown in Figure 20.

Figure 20 – Three-point bend core material test setup.

Multiple specimens were cut for both static and dynamic three-point bend testing. Four static three-point bend tests were conducted. A sandwich specimen with unfilled honeycomb core is shown in Figure 21, and a speckle pattern applied to the composite facesheet for use with 3D-DIC.

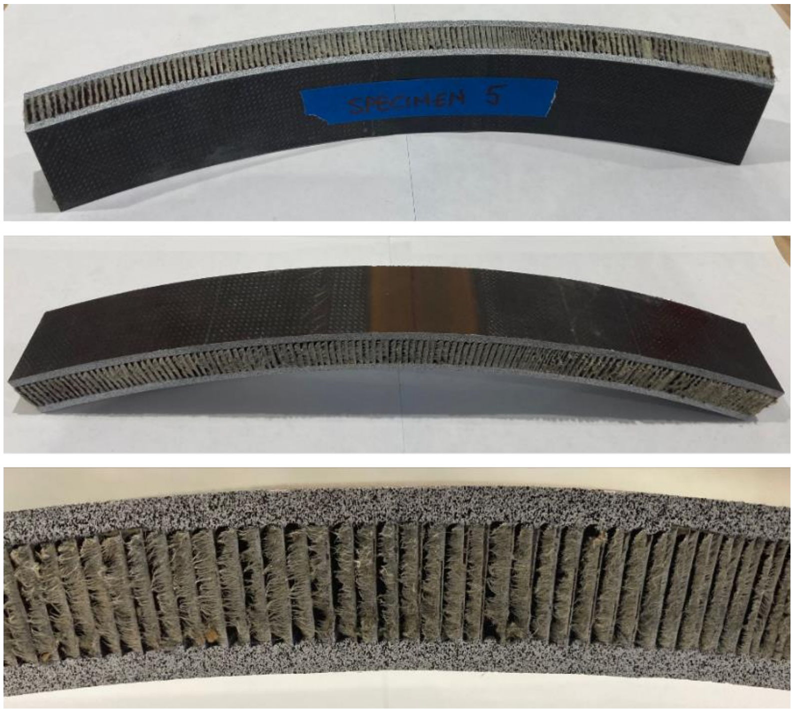

Figure 21 –Sandwich three-point bend specimen (Specimen 5).

The results from the three-point bend testing on the four sandwich panels with unfilled honeycomb core are shown in Figure 22. All four of the specimens behaved in a similar manner, reaching maximum loads between 900 lb. and 975 lb. at displacements between 0.2 in. and 0.24 in., respectively, followed by subsequent load drops as shear failure occurred within the honeycomb core. The bending stiffness for all four specimens was almost identical with an average slope of approximately 4850 lb./in.

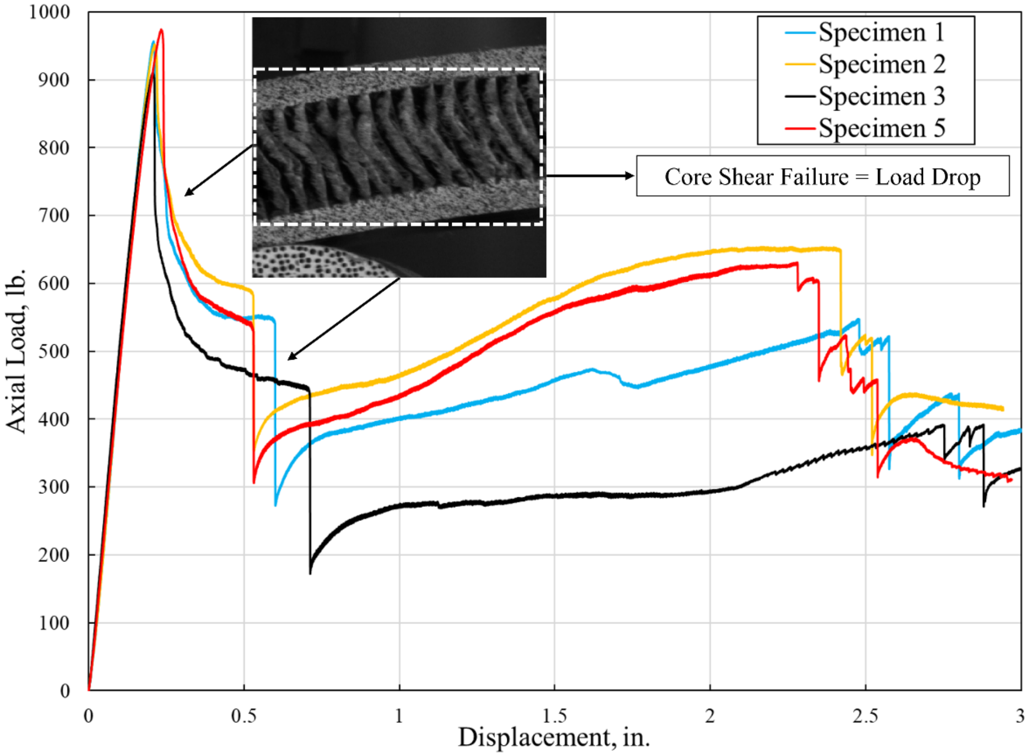

Figure 22 – Static three-point bend results for sandwich specimens (Unfilled Core).

## Filled Core Compression Tests (1 square inch size specimens)

All core specimens both filled and unfilled were tested on an MTS servo hydraulic test machine, which is shown in Figure 23. For the compression testing of the filled and unfilled core sections, a loading rate of 0.1 in./min. up to a maximum displacement of approximately 0.6 in. (selected based on the core thickness), or until core compaction was achieved, was used. Only load and displacement data were recorded from the MTS machine, and no measurements were taken using 3D-DIC.

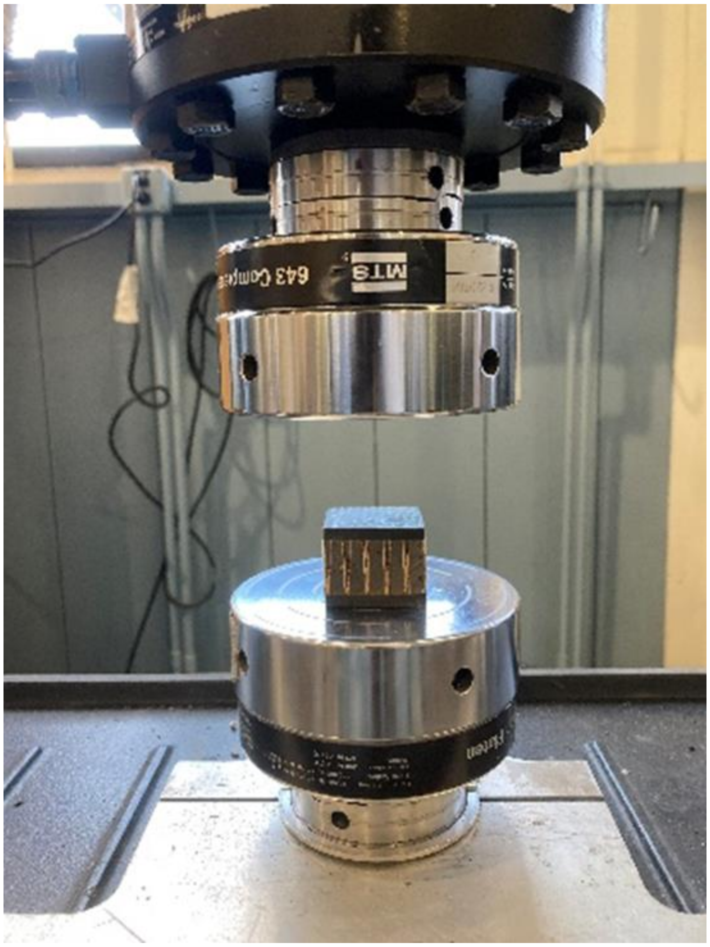

Figure 23 - Compression test setup of sandwich core specimens.

As previously noted, the filled sections of the sandwich core were primarily around openings, and only extended approximately 1 inch away from the opening. Because of this design choice, the specimen sizes were constrained to a little greater than one inch for the width and depth, leading to a cross sectional area of approximately 1.5 in.$^2$. Three variations of the specimens were tested, one with both facesheets, one with a single facesheet and one with the core only to determine differences in face-sheet bonding on the core boundary conditions. Specimen 2 represented the specimen with both facesheets (sandwich), specimen 4 represented a core only specimen, and specimen 6 represented a specimen with a single facesheet and core. For specimens without facesheets, the facesheets were removed by cutting them off during the specimen preparation process. All specimen types are shown in Figure 24.

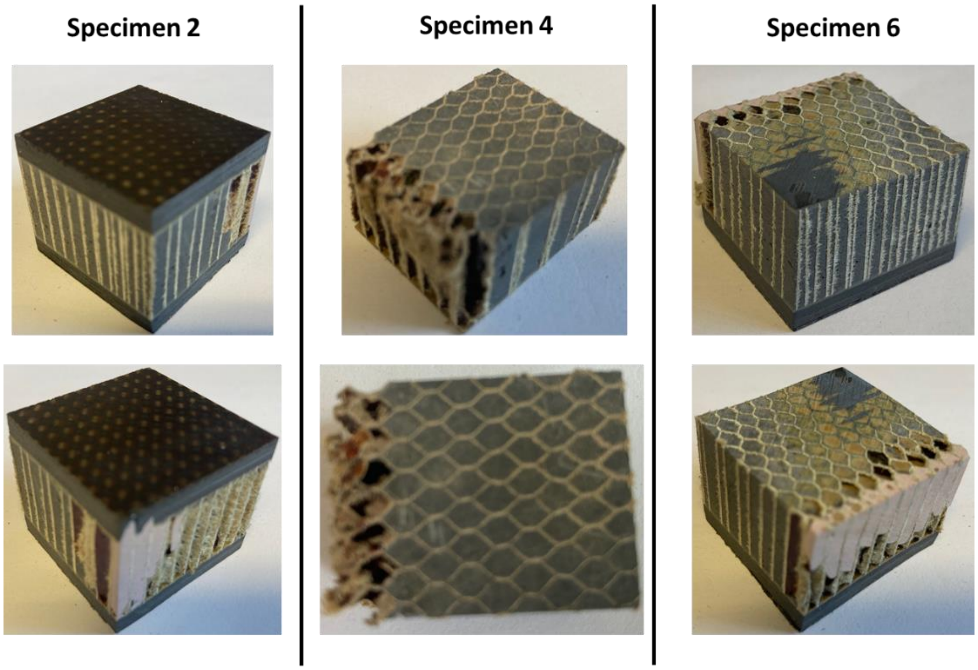

Figure 24 - Filled core specimens (1 inch).

All specimens were measured with average material properties computed and shown in Table 3. Note that the facesheets themselves were also measured to compute an average facesheet thickness value. Each configuration is noted in the table.

Table 3 - Compression specimen dimensions (Filled Core).

| Specimen | Test | Avg. Length (in.) | Avg. Width (in.) |
|---|---|---|---|
| 2 | Sandwich | 1.306 | 1.280 |
| 3 | Sandwich | 1.389 | 1.383 |
| 4 | Core | 1.290 | 1.027 |
| 5 | 1 Facesheet + Core | 1.286 | 1.250 |
| 6 | 1 Facesheet + Core | 1.276 | 1.286 |
| Facesheet | - | - | - |

The test data are plotted in Figure 25. Only three plots are shown in the figure, which represent nominal results obtained from the complete test series. A single facesheet test was not conducted.

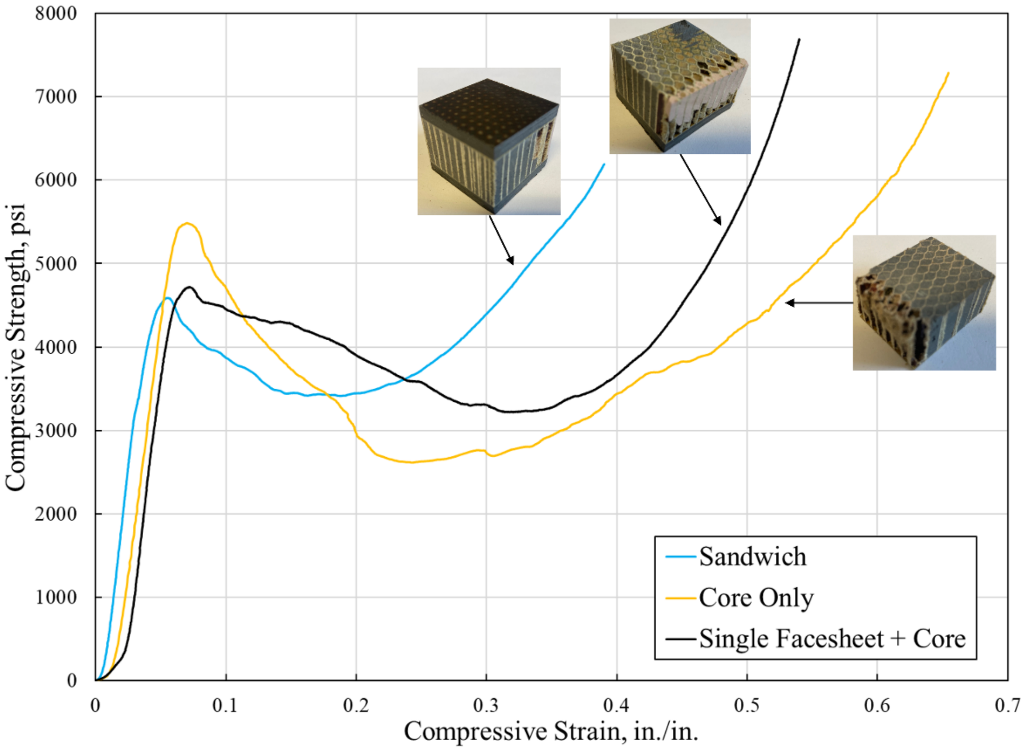

Figure 25 – Static compression results showing nominal response (Filled Core).

The three types of specimens all behaved very similar, reaching maximum compressive strength between 4500 lb./in.$^2$ (psi) and 5500 psi at approximately 5% strain, followed by an average plateau strength of approximately 3000 psi and compaction strain between 30% and 45%, respectively. The core only specimens exhibited slightly higher compressive strength and compaction strain, while the sandwich specimens and single facesheet plus core specimens exhibited slightly lower compressive strength and compaction strain, however the overall response of the specimens were very similar. These results may be attributed to the filled honeycomb core. The compressive moduli were almost identical for all three types of specimens with the filled honeycomb core at approximately 120 ksi.

## Unfilled Core Compression Tests (4 square inch size specimens)

Three cross-section specimen variations were also tested using the unfilled core locations - one with both facesheets, one with a single facesheet and one with the core only to determine differences in facesheet bonding on the core boundary conditions. Specimen 1 represented the specimen with both facesheets (sandwich), specimen 5 represented a core only specimen, and specimen 3 represented a specimen with a single facesheet and core. They are shown in Figure 26.

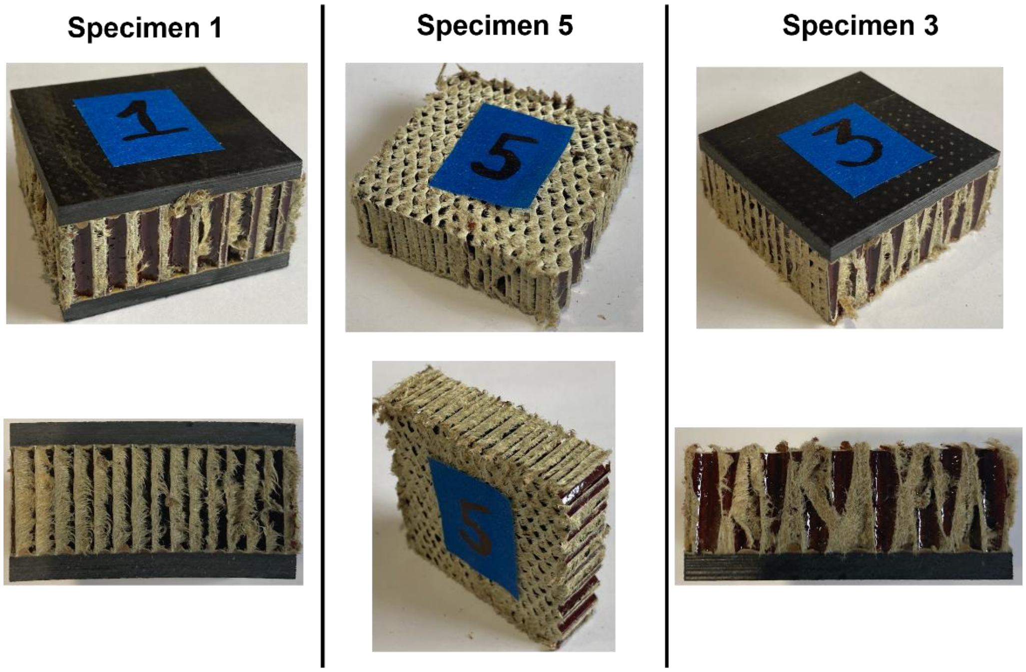
Specimen 1

Specimen 5

Specimen 3

Figure 26 - Unfilled core specimens (2 inch).

All specimens were measured with average material properties computed and shown in Table 4. As with the filled specimens, the facesheets themselves were also measured to compute an average facesheet thickness value. Each configuration is noted in the table.

Table 4 – Compression specimen dimensions (Unfilled Core).

| Specimen | Test | Avg. Length (in.) | Avg. Width (in.) |
|---|---|---|---|
| 1 | Sandwich | 1.993 | 1.966 |
| 2 | Sandwich | 1.972 | 1.962 |
| 3 | 1 Facesheet + Core | 1.941 | 1.989 |
| 4 | Core | 1.962 | 2.004 |
| 5 | Core | 1.968 | 1.972 |
| Facesheet | - | - | - |

The test data are plotted in Figure 27. Only three plots are shown in the figure, which represent nominal results obtained from the complete test series. As with the filled sections, a single facesheet test was not conducted.

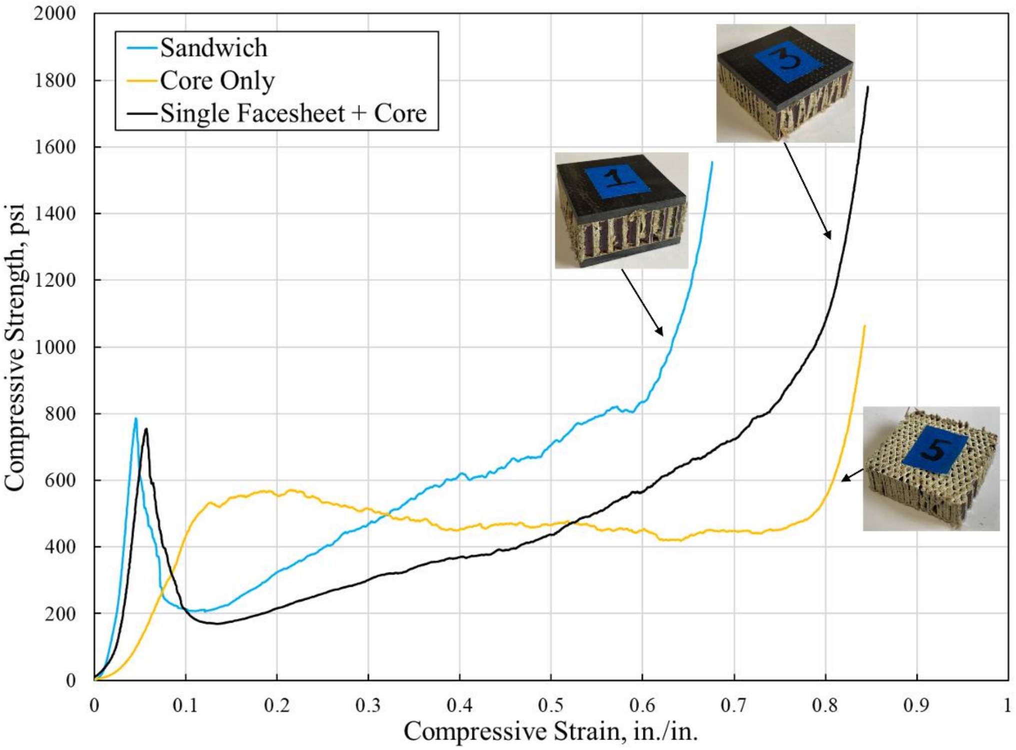

Figure 27 – Static compression results showing nominal response (Unfilled Core).

Unlike the compression results for the specimens with filled honeycomb core, the results for the specimens with unfilled core showed varying results. The specimens with a bonded facesheet, i.e., sandwich specimens and specimens with single facesheet plus core, exhibited similar behavior, reaching a maximum compressive strength of 800 psi at approximately 5% strain, followed by a sharp drop in strength to approximately 200 psi, and compaction strain between 60% and 70%. On the other hand, the core only specimen exhibited a lower compressive strength of 600 psi at approximately 20% strain, followed by a long stress plateau of approximately 450 psi and a compaction strain of approximately 80%. The compressive moduli for the specimens with bonded facesheet were approximately 23 ksi and 25 ksi, for single facesheet plus core and the sandwich specimens respectively, while the compressive moduli for the core only specimens were approximately 6 ksi.

## Flange and Sandwich (Unfilled) dynamic three-point bend tests

Finally, a series of dynamic three-point bend tests were conducted on two types of specimens: the composite flange and the unfilled sandwich core. All specimens were loaded in the concave direction using a 14-ft. drop tower. The test setup consisted of a 119-lb. instrumented impactor falling from a drop height of 18 in. to achieve a desired 10 ft./s. impact velocity. An accelerometer was mounted to the drop mass to record acceleration along the impact direction, recording at a sample rate of 50 kHz. The three-point bend fixture consisted of two 2-in. diameter rollers spaced 12 in. apart stationary on the reaction mass, with a 1-in. fixed roller attached to the falling impactor. A single high-speed camera was positioned to view the impact and study the failure dynamics during the event, imaging at a frame rate of 5,000 frames/s. The drop tower test setup is shown in Figure 28.

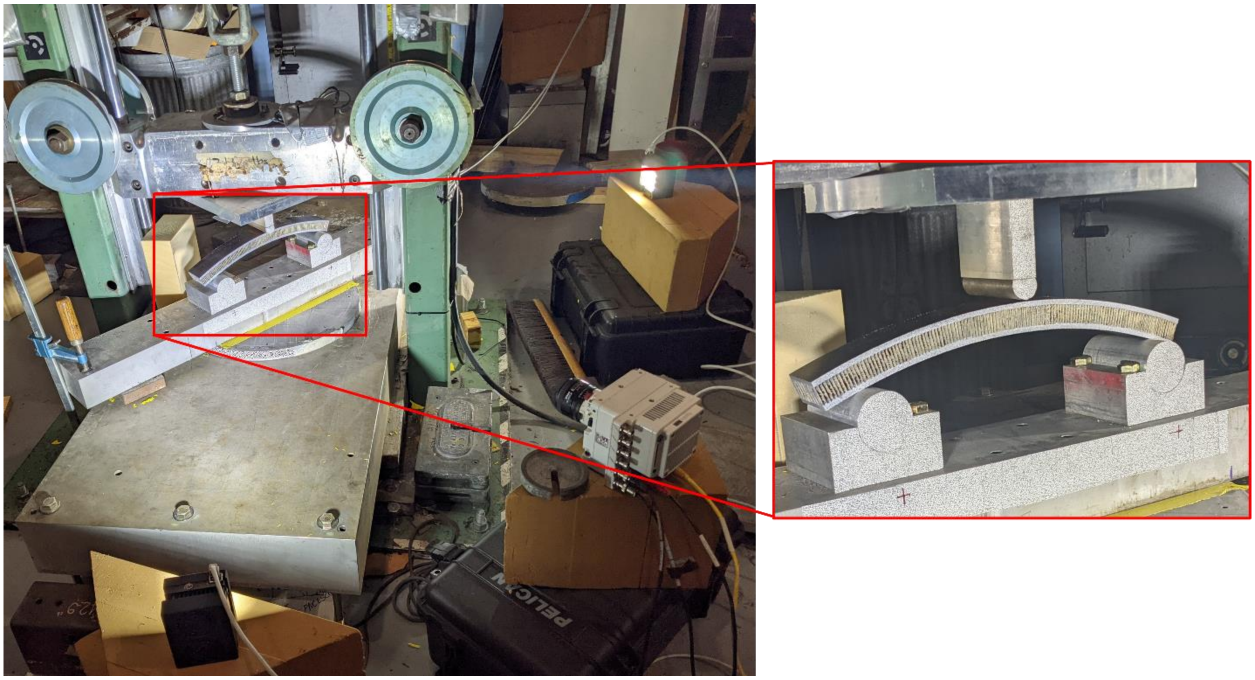

Figure 28 – Drop tower setup for dynamic three-point bend testing.

The two types of specimens that were tested are shown in Figure 29. Both specimens had the black and white speckle coat pattern applied to the facesheet edges for use in two-dimensional (2D) DIC data acquisition. The unfilled sandwich core portion of the specimen was not painted and DIC was not conducted on it.

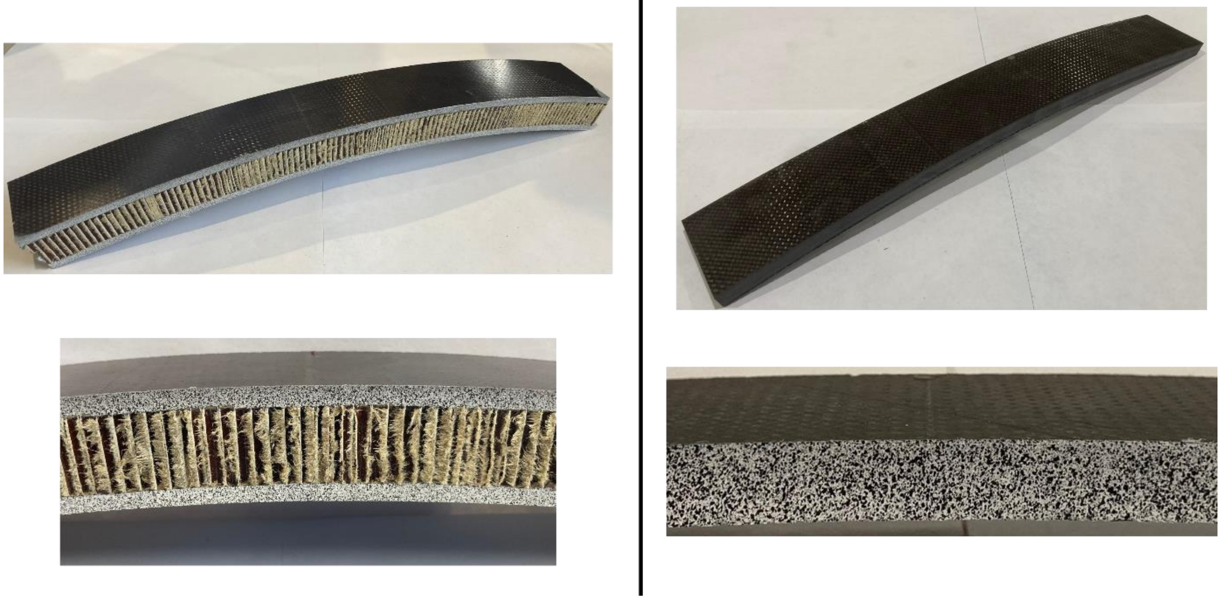

**Specimen 4**

**7076**

Figure 29 – Specimens for dynamic three-point bend testing, sandwich (left) and flange (right).

The overall dimensions of the specimens are shown in Table 5. These dimensions were similar to other specimens cut for use in static testing. While the sandwich specimens were slightly longer, the 12-inch spacing on the fixed end rollers in the three-point bend fixture essentially gave both configurations the same gage area.

Table 5 – Dynamic three-point bend specimen dimensions (Unfilled Core).

| Specimen | Test | Avg. Length (in.) | Avg. Width (in.) |
|---|---|---|---|
| 4 | Sandwich-Concave | 14.250 | 1.996 |
| 6 | Sandwich-Concave | 16.250 | 1.981 |
| 7076 | Flange-Concave | 14.250 | 2.015 |
| 8687 | Flange-Concave | 14.750 | 1.998 |

The test data are plotted in Figure 30. Only two plots are shown in the figure, which represent nominal results obtained from the complete test series.

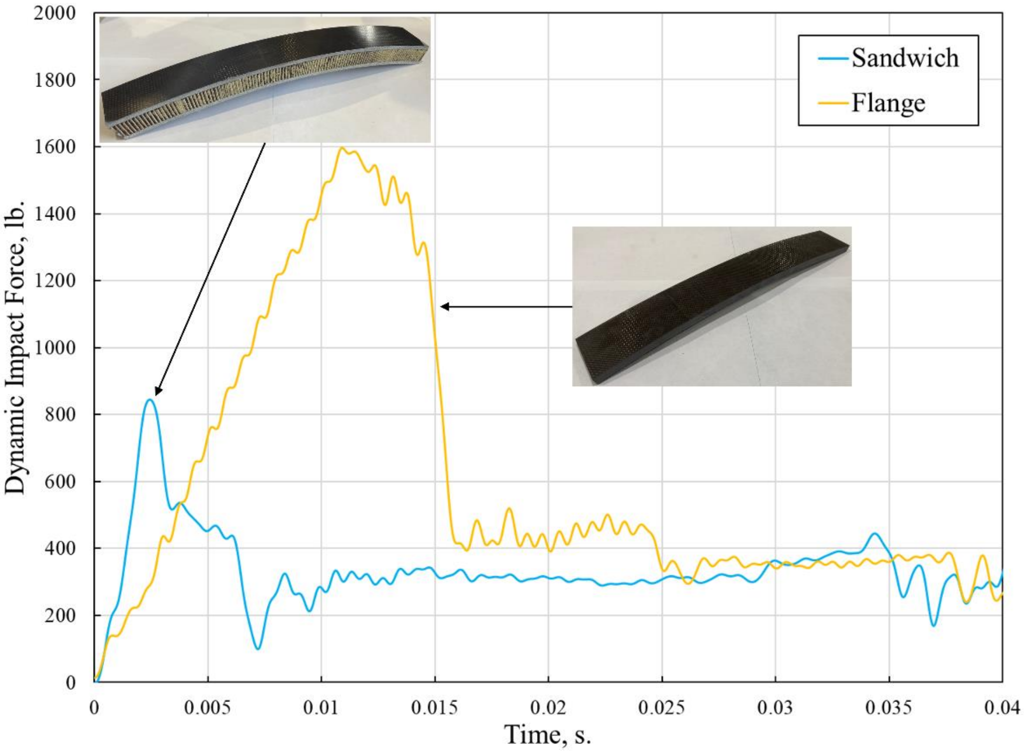

Figure 30 – Dynamic three-point bend results showing nominal response.

The data show the sandwich panel with unfilled honeycomb core was able to withstand a dynamic impact force of approximately 800 lb. prior to damage initiation (core crushing and/or core shear failure), while the composite flange panel was able to withstand approximately twice the impact load before damage initiation (cracking and fiber delamination) began. The damage initiation and failure observed for both types of specimens can be seen in Figure 31. For the sandwich specimen, post-peak damage continued which primarily consisted of crushing of the core at a sustained load of approximately 400 lb. The post-peak damage consisted primarily of tensile fiber failures on the bottom edge of the specimen.

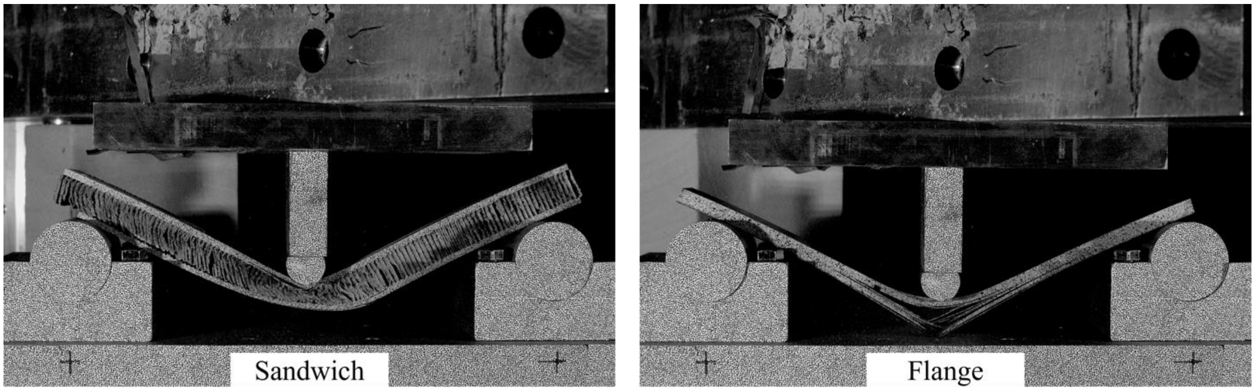

Figure 31 – Damage progression and failure during dynamic three-point bend test.

All of the material data collected were critical in developing the finite element models eventually used in the full-scale test campaign. The model development methodology is presented next.

## Full-Scale Model Development

FE models of the Hawker 4000 Fuselage test articles were reverse engineered from the full test article. The FE model geometry was generated from the 3D scan taken of the test article prior to sectioning. Constituent material properties of the sandwich composite structure were generated from testing of isolated material samples cut from the Middle Section. The combined sandwich structural model was calibrated using representative components tests and validated using the dynamic tests conducted. This reverse engineering process comes with inherent simplifications of both the geometric representation of the physical test article and the representation of the composite material structure. Using 3D scans to generate model geometry limits the representation of finite details in the geometry. Generating material models from full-fabricated composite specimens does not allow for precise representation of composite layup variations throughout the structure. The primary purpose of the full-scale test to model correlation effort was to evaluate the effects of these simplifications on FE model prediction of structural damage, deformation, and acceleration.

To generate FE model geometry from the 3D scan of the test article, an outer mold line (OML) was first isolated from the scans at the Forward and Aft Section locations. Large openings in the Forward and Aft sections were included within the OMLs. The fidelity of the 3D scans did not allow for finite details such as small holes and deviations in skin thickness to be captured. Surface geometries were then constructed from the extracted OMLs. A mesh template was generated on the surface geometries using 0.9-in. quadrilateral shell elements. Solid elements representing the carbon composite skin and honeycomb interior were then extruded from the template mesh to match the thickness of each component measured on the test articles. The composite skin and the honeycomb were then extruded to their appropriate thicknesses. Each component part mesh was separated and tied contact with failure was implemented between the carbon composite and honeycomb parts to represent the bonding agent used in the sandwich structure. The 3D scan and generated FE model geometries of the Forward and Aft Section test articles are shown in Figure 32.

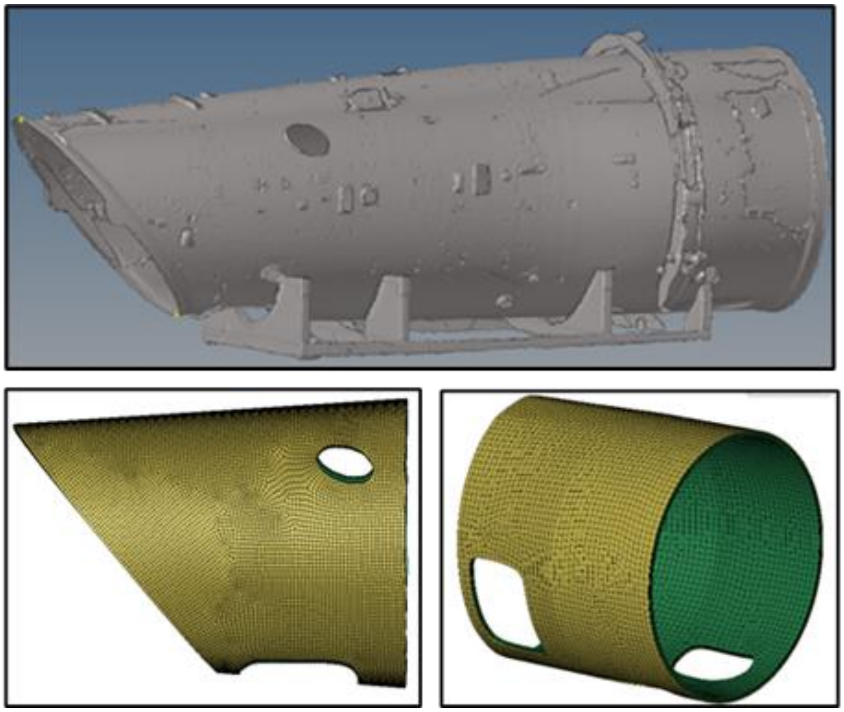

Figure 32 – 3D scan of Hawker 4000 test article (top) and FE models developed from scan: Aft Section model (left) and Forward Section model (right).

Material model characterization began with the constituent parts making up the sandwich composite structure of the fuselage. A model of the composite skin material was generated first using data from the static three-point bend testing of the composite flange samples. To replicate the three-point bend-testing a model of the three-point bend test fixture was generated. The model consisted of the two support rollers rigidly fixed in space and an indenter mass with curvatures matching that of the test fixture. The support rollers and mass were modeled using shell elements with a rigid aluminum material model. The indenter mass and impact velocity were prescribed using *Part_Inertia to represent the test setup described in the *Flange and Sandwich (Unfilled) dynamic three-point bend tests* section. The composite flange test article was modeled using solid elements with a mesh size of 0.1 in. and the *Mat 59: Composite Failure Solid material model. The geometry of the flange test article model was generated to match the geometry of the test articles used in testing, characterized through DIC. Models were generated to represent the concave and convex tests conducted. The developed three-point bend test with the composite flange model is shown in Figure 33.

Figure 33 – Flange three-point bend test and representative model setup.

Simulations were performed to replicate the as tested conditions of the flange three-point bend tests. All component simulations described in this report were carried out using LS-DYNA SMP version R10.10 single precision on a Linux computer cluster. The moduli and strength parameters of the composite material model were calibrated through simulation of the concave and convex three-point bend test conditions to replicate the force displacement data recorded in test. The concave and convex testing exhibited a similar data spread, indicating minimal difference in force displacement response between the two conditions. Simulations of the two test conditions similarly showed near identical force displacement response. Due to similarity in responses, data correlation is shown with the concave and convex data combined. The calibration of the composite material model moduli and strength parameters resulted in close prediction of the linear force-displacement response of the tested specimens. The predicted force-displacement slope was within the range measured in the tested specimens. In addition, the initial drop-off in force, indicating specimen failure, was predicted at the axial displacement and load measured in the specimens. To verify realistic bending behavior of the developed model, localized strain measurements, gathered during test using DIC, were also compared between test and simulation. Results showed similar location of strain initiation and progression through the specimen during bending. These results provided confidence to the developed composite skin model. The static three-point bend test to simulation comparisons of DIC measured strain and force-displacement response is shown in Figure 34.

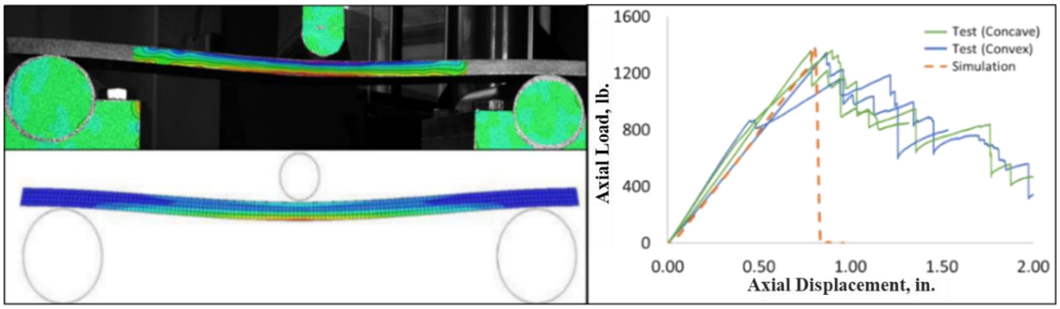

Figure 34 – Test to simulation correlation of composite flange three-point bend testing. DIC results (right) and time history plots (left).

Models of the honeycomb core materials, both filled and unfilled, were generated using the honeycomb core compression test data. During the honeycomb core testing, it was found that the composite skin stabilized the boundary of the honeycomb during compression and thus provided the most consistent crush response. For this reason, the sandwich specimen configuration was used to generate the honeycomb material model. A model of the tested sandwich specimens was generated which included the composite skin boundaries and honeycomb core. The honeycomb core was modeled as a single layer of solid elements with material model *MAT 126: Modified Honeycomb. The developed honeycomb core model is shown in Figure 35. A single element thickness was used in the honeycomb model because multiple layer element thickness models were found to produce unrealistic crush behavior in preliminary simulations.

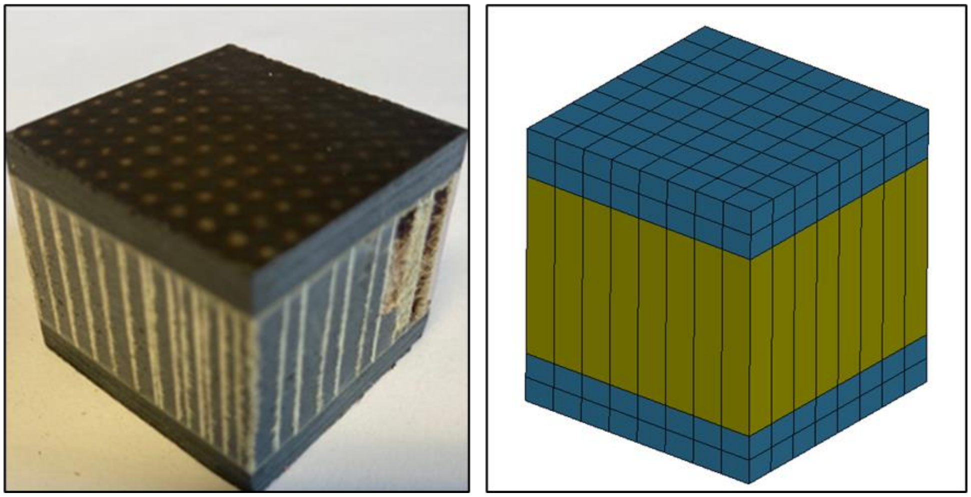

Figure 35 – Honeycomb sandwich specimen and representative model.

The sandwich core specimen model was simulated in the tested conditions. The material model parameters of the honeycomb core along the axis of compression were calibrated to match the tested material response. Parameters defining response in the remaining directions were calibrated through subsequent three-point bend test correlation. Unique material parameter sets were generated for both the filled and unfilled honeycomb material. Comparison between the test data and simulation results for both the unfilled and filled honeycomb is shown in Figure 36. The developed material models closely tracked the stress required to initiate crushing of the honeycomb core as well as the stress-strain response during crushing. Results diverged from the core only specimens due to the boundary effects of the sandwich panel but closely matched the test specimens with the composite skin. Results provided confidence in using the developed material model to predict the honeycomb material response under compressive load normal to the sandwich surface. Next, testing was conducted to characterize the bending load response of the honeycomb sandwich composite.

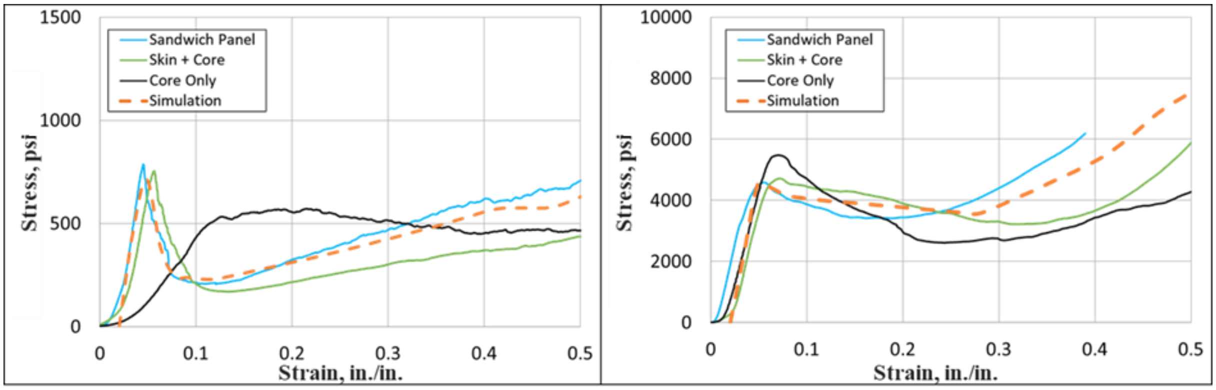

Figure 36 – Stress strain correlation results for unfilled (left) and filled (right) honeycomb compression tests.

The static three-point bend tests of the sandwich composite specimens were used to calibrate the remaining material axes of the honeycomb model and the bonding model used between the honeycomb core and composite skin. A representative model of the sandwich composite test configuration was generated using the component models developed from the composite shell and honeycomb tests. The test and representative model configuration are shown in Figure 37. Initially, the honeycomb and composite shell elements were joined using shared nodes. During calibration, it was found that this limited prediction of rotation and re-orientation of the honeycomb during specimen bending which was observed during test. To represent the glued bond between honeycomb and composite skin, the shared nodes were replaced using tied contact with failure between the face surfaces of each part.

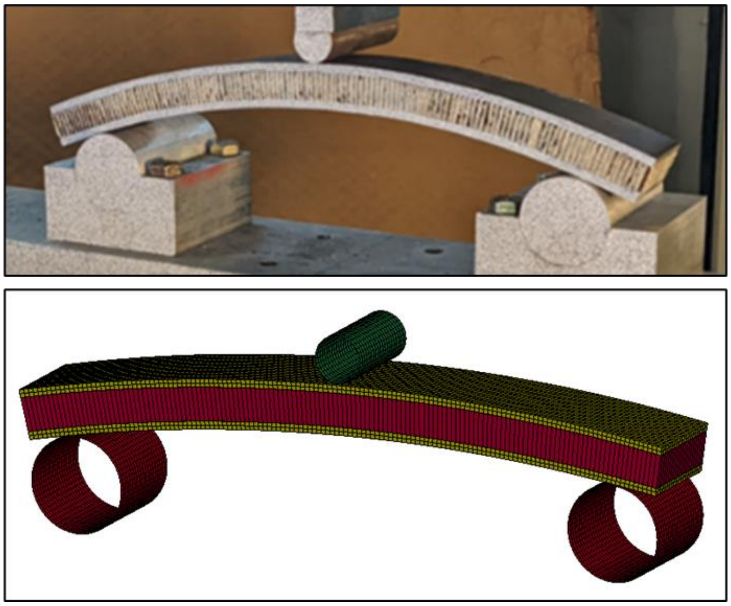

Figure 37 – Composite sandwich three-point bend test and representative model setup.

The sandwich composite static three-point bend test to simulation comparisons of DIC measured displacement and force-displacement response is shown in Figure 38. During the test there were four distinct phases of loading measured in the force-displacement response of the sandwich specimens. The first phase was elastic compression of the sandwich composite, indicated by a linear increase in compressive force with displacement. Correlation to this response required minimal tuning as it was driven by previously calibrated stiffness parameters of the component materials. High-speed imaging of the tests indicated the first two drops in compressive load were caused by isolated shearing of the honeycomb material at the outer edges of the specimen. The shape and magnitude of the response curve over this time were used to calibrate the parameters defining shear stiffness within the honeycomb material model. After the second drop the honeycomb material re-oriented with the bending of the sandwich composite allowing compressive force to increase as displacement progressed. This behavior was achieved by implementing the tied contact between honeycomb and composite skin. The final drop in compressive load, occurring after displacement of approximately 2.25 in., was caused by honeycomb shearing which spread through the center of the specimen followed by delamination of the skin. The timing of this response was used to tune the element failure parameters of the honeycomb material model. With thorough calibration of the honeycomb material model and the part constraint definition, the composite sandwich model closely replicated each distinct loading phase measured in test.

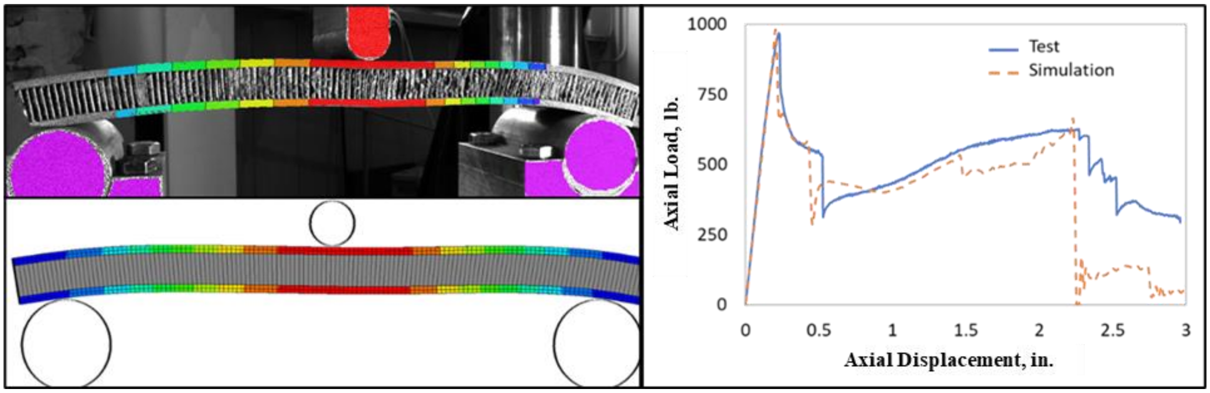

Figure 38 – Test to simulation correlation of composite sandwich three-point bend testing.

After developing the component material models through static test correlation, the predictive capability of the models under dynamic loading conditions were verified using dynamic three-point bend tests performed on specimens of both the carbon composite flange and carbon composite honeycomb sandwich. The model replicated the test condition of 119-lb. mass with indenter impacting the test specimens with an impact speed of 10 ft./s. This boundary condition was represented in the FE model by applying a point mass and initial velocity to the indenter component. The response of the test specimens under dynamic load was quantified by vertical acceleration measured on the indenter mass. A picture of the composite flange test and representative simulation at initial observable composite failure and acceleration time history correlation is shown in Figure 39. The composite flange exhibited a linear increase in acceleration which peaked at approximately 15 g. After peak acceleration the carbon composite began to fail which led to a sharp drop in acceleration. The composite flange model, which was calibrated to the static tests, was shown to closely predict the onset of acceleration of the indenter as it crushed the carbon composite material but slightly underpredicted peak acceleration. The composite flange model predicted composite failure approximately 0.002 s. earlier than the test which resulted in the underprediction of peak acceleration. Damage location and progression was similar between test and simulation.

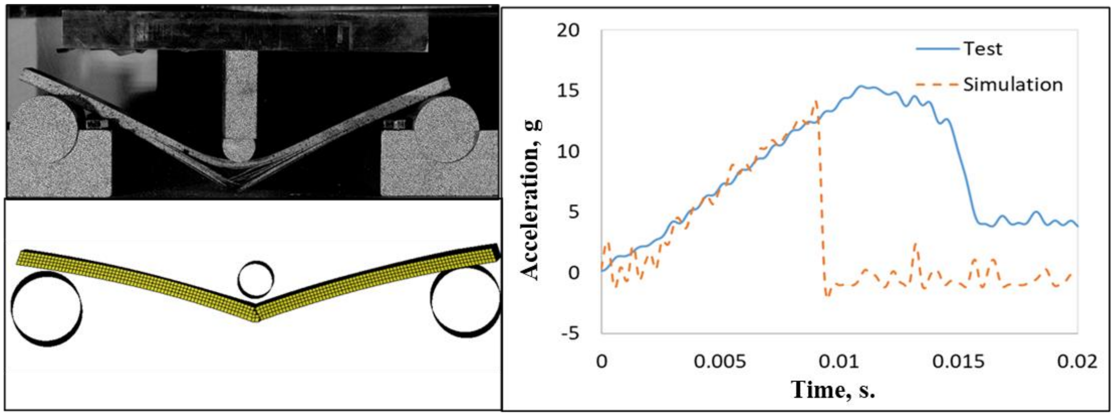

Figure 39 – Test to simulation correlation of composite flange dynamic three-point bend test.

A comparison between the sandwich composite dynamic three-point bend test and simulation is shown in Figure 40. The sandwich composite exhibited linearly increasing acceleration to approximately 8 g, followed by a two phased drop in acceleration. This tiered acceleration drop mimicked the stress strain response observed in the static three-point bend testing which was driven by shearing of the honeycomb. After significant shearing and compression of the honeycomb, the carbon composite shell also failed. Although there were some differences in acceleration prediction with the flange only model, the sandwich composite model accurately predicted the shape, phase, and peak response of the indenter as it induced progressive failure in the sandwich material. These results provided confidence that the combined material models of the Hawker 4000 fuselage, calibrated under the static test conditions, were effective at predicting dynamic impact response up to and through component failure.

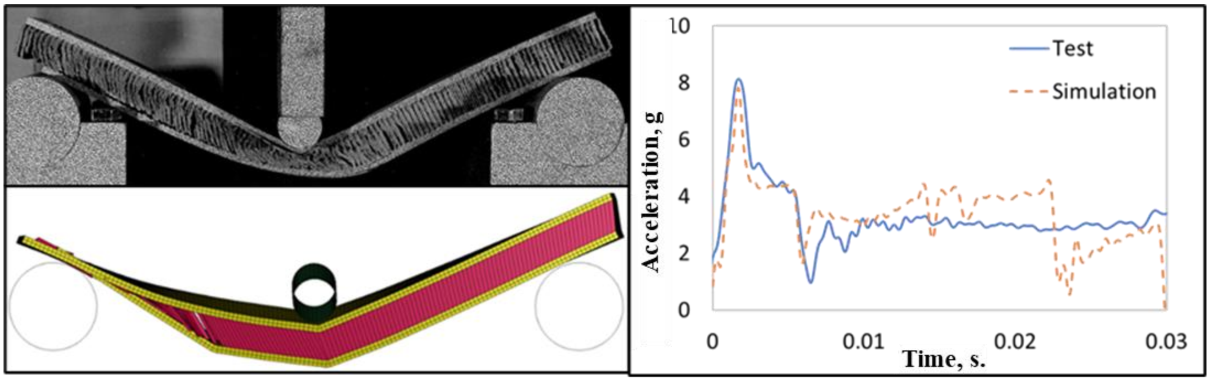

Figure 40 – Test to simulation correlation of composite sandwich dynamic three-point bend test.

Once the component level models were deemed adequate in their prediction of response, the calibrated material models were integrated into the Forward and Aft Section FE models. As one goal of this study was to evaluate prediction of composite structure material failure, the generated FE models were then simulated to identify impact conditions which would induce significant amounts damage into the composite structure to satisfy the test objectives. Impact velocity, test article pitch angle, and ballast mass were adjusted within the pre-test models to identify the test conditions. Based on this analysis notional test conditions for the Forward Section of 30 ft./s. vertical velocity, 20 degrees pitch down, and 350 lb. of ballast weight was selected. Notional test conditions of the Aft Section were 30-ft/s vertical velocity, 20-degrees pitch up, and 200 lb. of ballast weight. The full-scale test conduct of the Forward Section is described next.

## Full-Scale Testing – Forward Section

Based on the predictive computational modelling efforts, a vertical drop condition of 30 ft./s. nominal velocity at a 20-degree nominal downward pitch angle was chosen. Ballast in the test article was included by using seven 25 lb. weights on both sides, located on the interior walls and mounted 72 in. above the belly as shown in Figure 41. Four of the weights were located forward of the geometric centerline, while three of the weights were located aft of the center line, with a 2.5 in. spacing between block edges. They were mounted into c-channels for stability and through bolts were used to secure. The location of the blocks would bias the center of gravity (CG) toward the forward end of the test article which was anticipated to contact the impact surface first in the test. The impact conditions and ballast were selected such that the test article would impact at the forward tip, introducing a point load into the structure for the initiation of failure.

Figure 41 - Ballast weight secured on the port side of the Forward Section.

Instrumentation in the form of biaxial and triaxial accelerometers were placed at locations around the test article. Triaxial accelerometers were placed on the forward and aft belly locations. A biaxial accelerometer measuring vertical (z) and horizontal accelerations (x) was placed in the belly middle location. Triaxial accelerometers were placed at the mid-height sidewall locations on the forward portion of the test articles on both the port and starboard sides. Biaxial accelerometers measuring vertical (z), and lateral (y) accelerations were placed on the mid-height sidewall locations on the aft portion of the test article.

Additional accelerometers were placed along the ballast locations. Triaxial accelerometers were placed on the most-forward and most-aft ballast locations for both the port and starboard sides. These accelerometers are labeled forward and aft, respectively. Biaxial accelerometers measuring horizontal (x), and vertical (z) accelerations were placed on the inner two ballast masses for both the port and starboard sides. These accelerometers are labeled Mid-Forward and Mid-Aft, respectively. All accelerometer locations are shown in Figure 42 and are intended to provide a near complete measurement of the loading environment from the test.

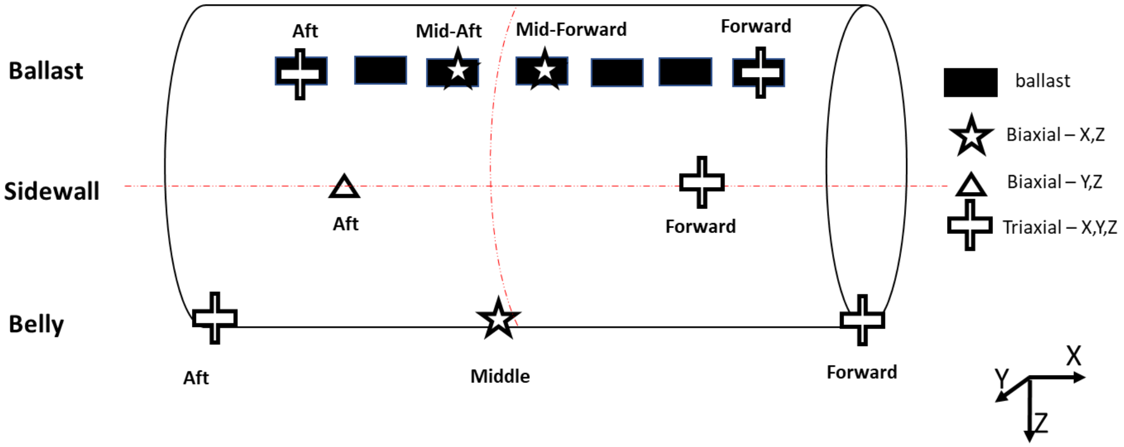

Figure 42 – Forward Section test article instrumentation.

In addition to the accelerometers, a suite of sensors designed to acquire structural health monitoring data were also installed. These included fiber optic strain sensors, eddy current coil sensors and surface acoustic wave sensors and were present to evaluate some typically non-traditional methods for measuring damage and failure during impact testing. The data from these sensors will be the subject of a separate report. The inclusion of the ballast and instrumentation yielded a final test weight of 740 lb.

The collection of high-speed 3D-DIC data was one of the primary objectives of the test, so time was taken to paint three of the test article surfaces with a high-contrasting black and white stochastic pattern, and to configure and calibrate three sets of high-speed cameras. The test article was first painted with a white base coat, and then a pattern consisting of ½-in. round black dots was hand painted onto both the port and starboard sides. Additionally, in the interior, the floor from the belly to the mid-height was hand painted with 3/8-in. round black dots. For the port side, cameras imaging at 1 kHz at 2 megapixels (MP) were used while on the starboard side, cameras imaging at 1 kHz at 4 MP were used. For the interior views, cameras imaging at 5 kHz at 1 MP were used. These views were supplemented by additional interior and exterior high-speed cameras covering various other views for use in quantitative and qualitative measurements.

A load platform was used as the impact surface. Four 50-kip load cells were secured to an 8 ft. by 12 ft. by 3 in. steel plate. The plate weight was 12,167 lb., and the plate was placed on the concrete pad at LandIR. The load cell legs were shimmed such that all four load cells were reading the approximate same load, indicating the plate was resting evenly on the four load cells with the largest differential in load reading of 206 lb. In addition to reading the impact loads, the load platform was instrumented in two corners with triaxial accelerometers.

All data were collected via offboard data acquisition systems using an umbilical cable bundle extending from back port side ballast location. Data were collected at a rate of 25 kHz. In addition, an IRIG timecode signal was input into both the data systems and high-speed cameras such that the collected data could be synchronized when examining post-test.

The Forward Section drop test was conducted on March 16, 2022. The test article was raised to a height of 14 feet, measured at lowest portion of the belly, and at an angle of 20 degrees by using various sized lifting straps, and then dropped onto the impact surface via a release hook. A picture of the test article at its drop height is shown in Figure 43.

Figure 43 - Forward Section Test article at drop height.

The test article impacted the load platform with a vertical impact velocity of 30 ft./s. and a pitch down angle of 19.7 degrees. An image sequence of the starboard side of the test article in shown in Figure 44, as recorded from the north side high speed camera. The general test sequence is described as follows:

- The test article first contacted the impact surface at the forward edge, thus initiating failures in this region.
- After the forward edge contact, the test article rotated such that the middle belly portion of the test article made contact with the impact surface, while damage in the forward edge progressed.
- After middle belly contact was made, the test article rebounded and became fully airborne.

- After the rebound, the test article made a second contact with the impact surface and came to rest, on its side, which is where it remained during post-test inspections.

An image sequence of the test as recorded by the starboard side camera depicting these notable events with timing is shown in Figure 44.

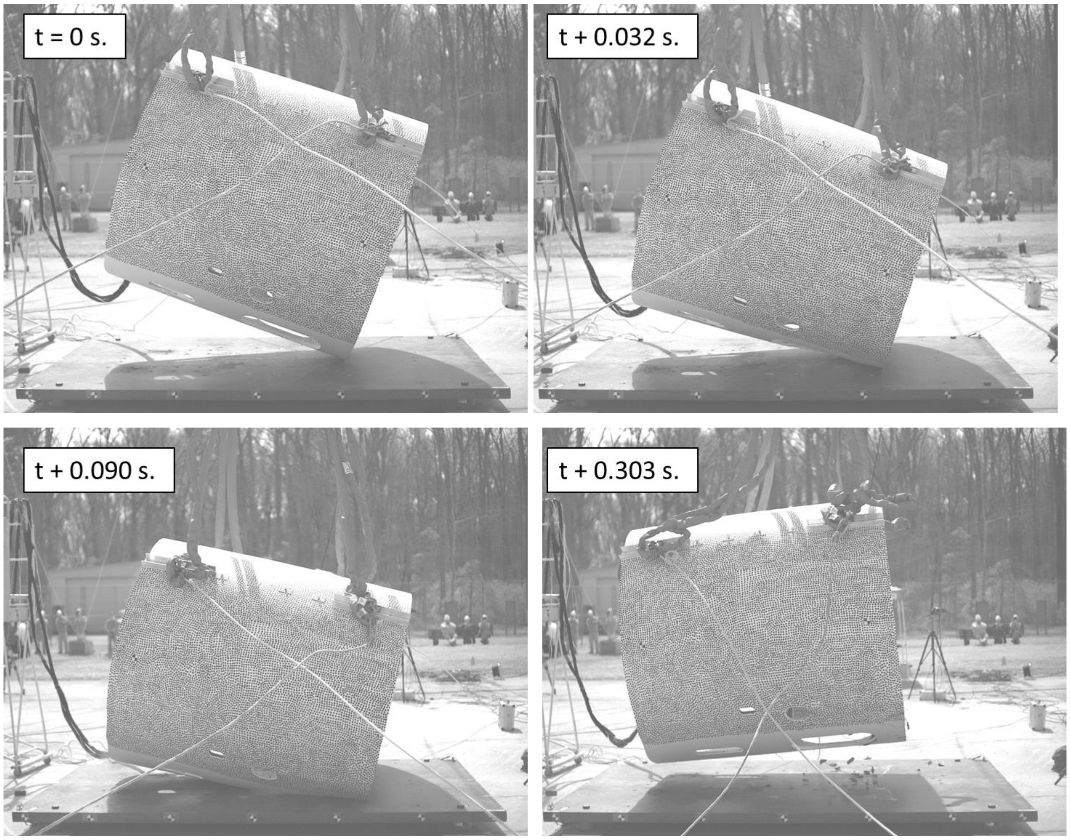

Figure 44 – Starboard side image sequence.

The images from this camera view provided relevant information to identify some of the notable events that occurred throughout the test sequence. The upper left image shows the test article at the time of impact, noting that the forward end, which is depicted on the right side of the image, has contacted the impact surface. The upper right image is taken at 0.032 s. after impact shows the test article at the time in which the composite sandwich structure in the forward end begins to delaminate. The lower left image shows the test article at the point of maximum vertical deflection, while the lower right picture shows the test article at the time of maximum rebound, 0.303 s. after initial impact.

The interior view was captured by a high-speed camera located on the forward port side of the test article. An image sequence, as captured by that camera, is shown in Figure 45.

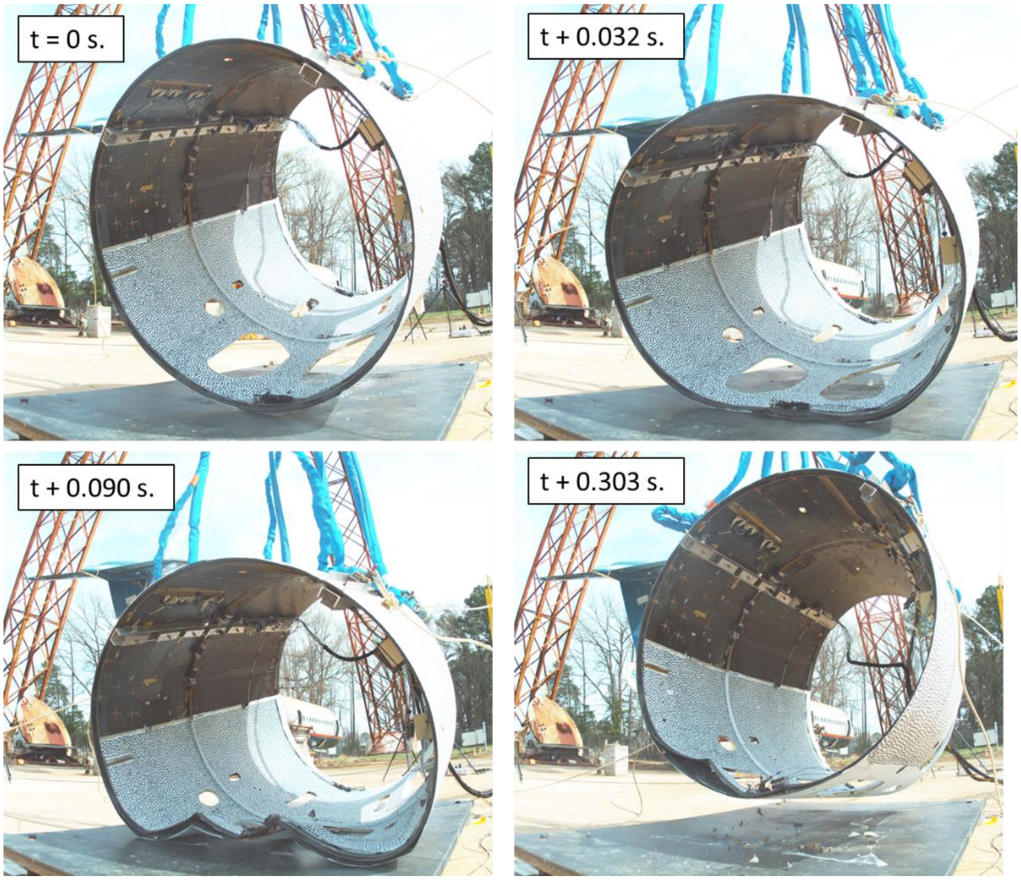

Figure 45 - Ground level forward side image sequence.

Paralleling the sequence shown in Figure 44, the test article at the time of impact is shown in the upper left image of Figure 45, noting that the forward end has contacted the impact surface. The upper right image shows the test article at the time in which the composite sandwich structure began to delaminate. The lower left image shows the test article at the point of maximum vertical deflection, noting the large amounts of delamination and failures that have occurred at the forward impact location. The lower right picture shows the test article at the time of maximum rebound. The permanent delamination and damage are also visible in this image. The vertical displacement corresponding to the image sequences shown in Figure 44 and Figure 45, as measured using 3D-DIC, is shown in Figure 46. Note that the maximum and minimum values of the contour scale, as designated by the red and purple colors respectively, are adjusted for each notable event.

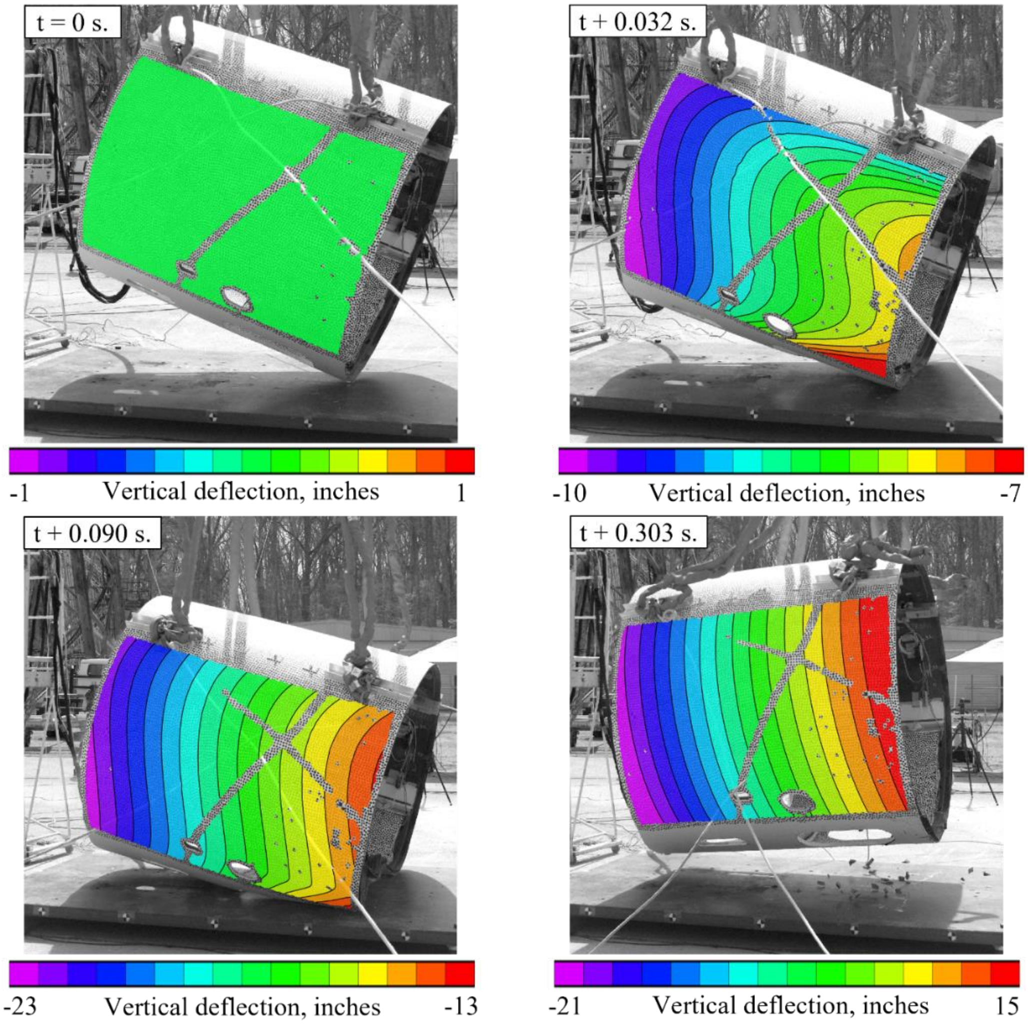

Figure 46 – Vertical deflection of starboard side image sequence.

The majority of the visible damage occurred in the forward half of the test article, at points starting at the impact location and extending aft until the center ring. At the impact location, the composite exhibited complete tensile failure on either side of the impact point, indicated by the breaking of the inner fibers, protruding inward, forming a "w" shape over a significant portion of the belly forward edge. Note the accelerometer suite measuring accelerations at the forward belly locations were fastened using a through-bolt through the skin. This fastening method created an artificial restraint that restricted any potential delamination that occurred at the point of impact. Detail of the forward edge delamination is shown in Figure 47.

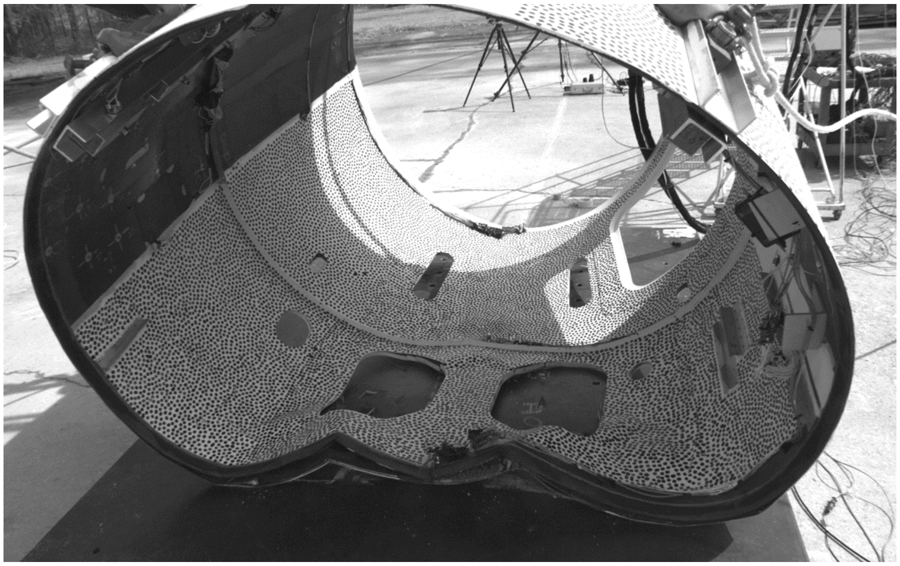

Figure 47. Internal view at time of maximum deflection.

Immediately after the test article came to rest, the post-test inspections began. Other areas in the forward half of the test article also exhibited visible delamination, including many locations around the two centerline openings. The two large openings on the belly near the forward impact location exhibited the most serious extent of the damage. Much of the opening delaminated, allowing numerous pieces of the center foam to break free. These failures are shown in Figure 48.

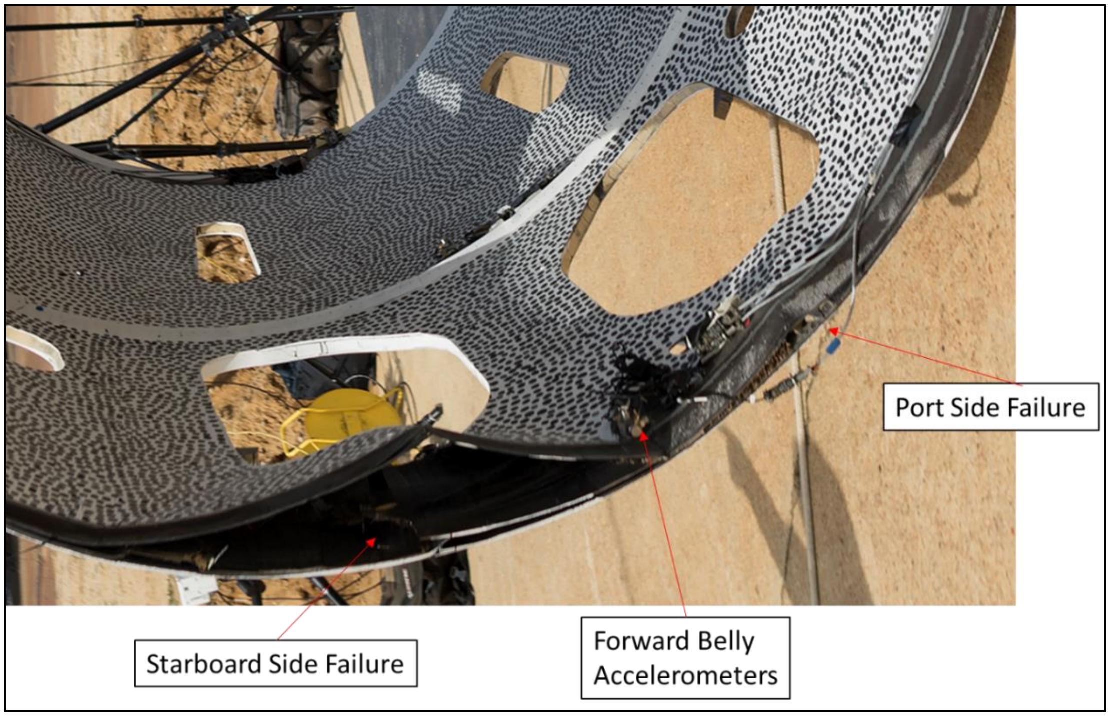

Figure 48 - Belly skin failure at impact point.

Additional delamination can be seen on the aft side of the forward holes. Around the middle stiffener area, the deformations causing the skin to protrude inward appear to have initiated. However, either due to the metallic ring stiffener being present or the lack of substantial residual kinetic energy remaining in the test article, a full inversion was not observed

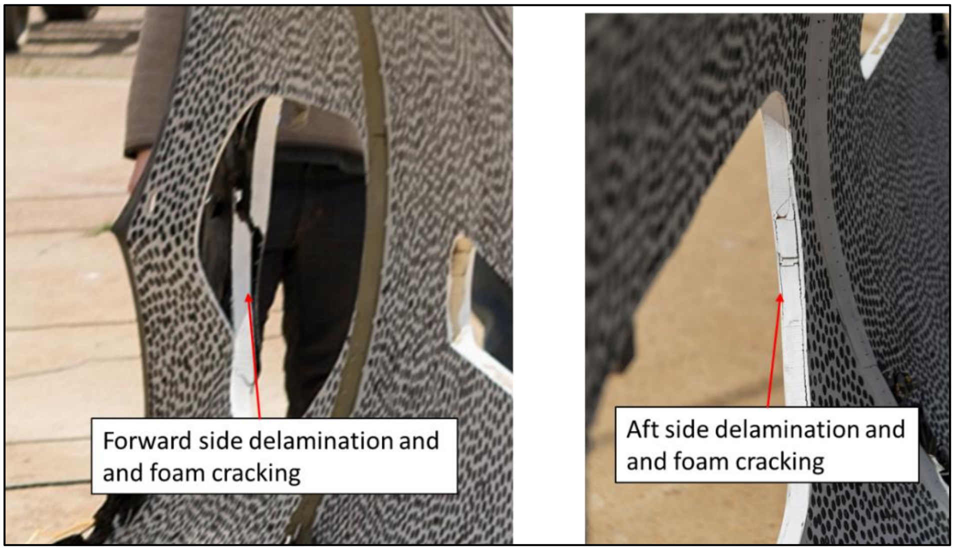

Figure 49 - Starboard side belly opening. Forward view (left) and aft view (right).

Utilizing the 3D-DIC technique, the visible damage and locations can be further illuminated. The photogrammetry data were examined using a multitude of computed variables, however the variable that most clearly shows the damage was the variable Sigma. The variable Sigma represented pixel deviation from a reference image, which, in this case, is the undeformed test article immediately prior to impact. Investigating the Sigma variable allowed for quick identification of locations with large deviations, indicating areas of potential damage. The Sigma variable colormap, shown in Figure 50

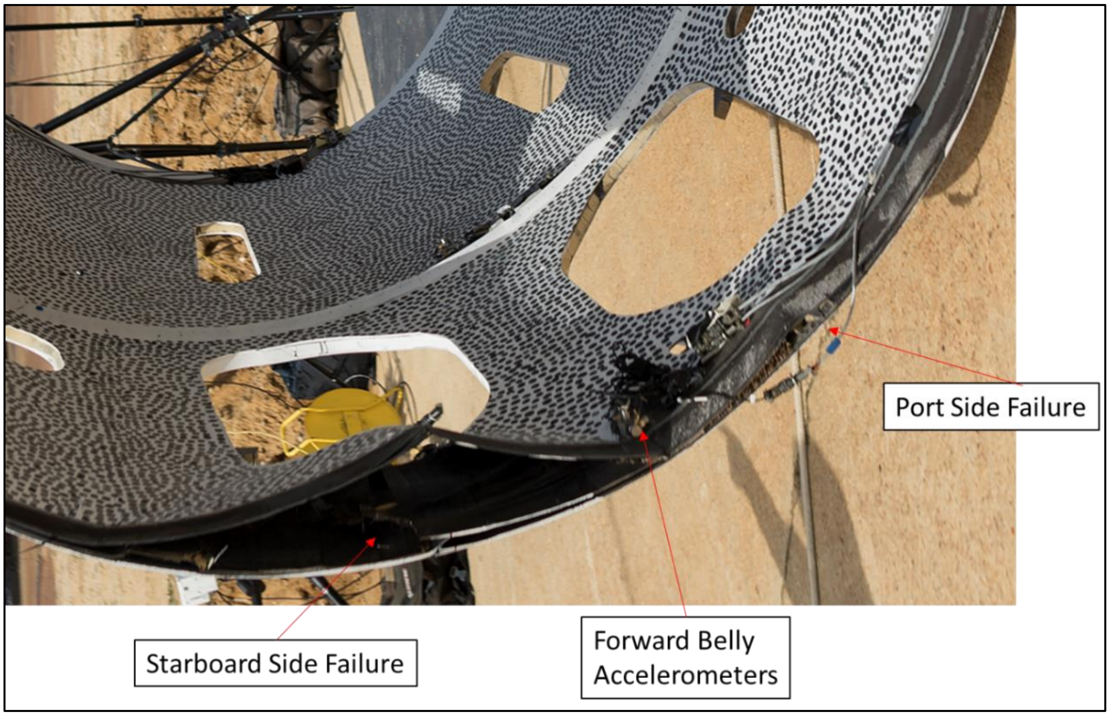

, highlights the significant amount of damage and failures located in the forward belly section, noted by the areas of green/red.

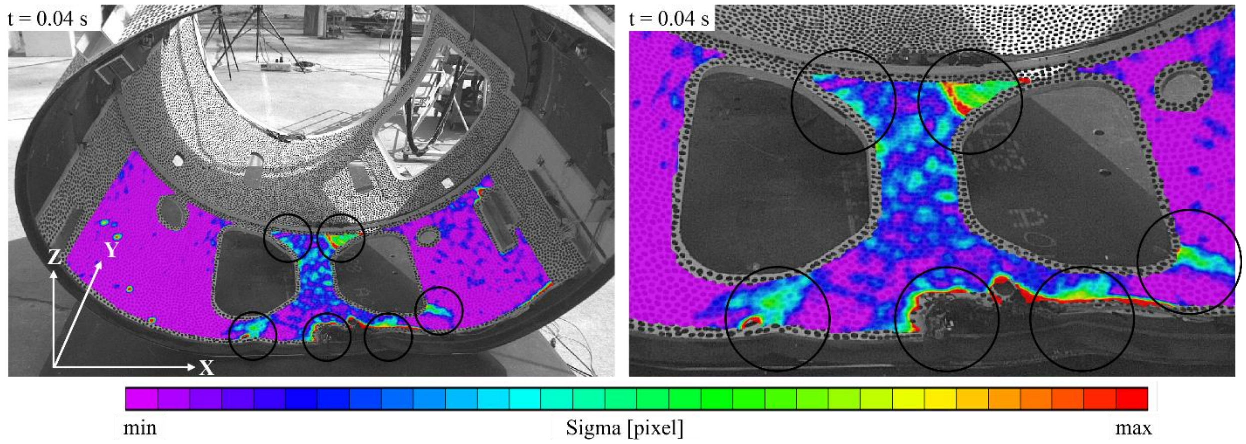

Figure 50 – Delamination and damage propagation observed in the inner mold line (IML) of belly.

Additional compression failures occurred on the port side of the test article, approximately midway up the vertical height. These failures are visible noted by a longitudinal crack in the inner sandwich facesheet composite approximately 10-in. long halfway between the port belly opening and the mid-plane of the test article. These cracks appeared on both sides of the test article in the same approximately location. A compressive failure crack on the port side can be observed in Figure 51.

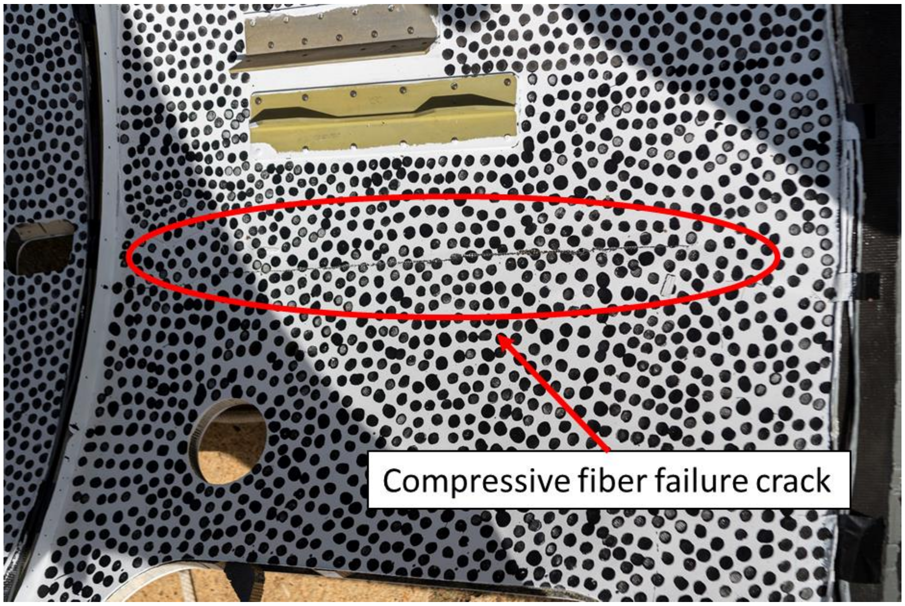

Figure 51 - Compressive fiber failure cracking (Port side).

Utilizing the computed Sigma variable within the 3D-DIC software, these compression failures become more pronounced, and are easily observed, along with the time at which initiation occurred. The compressive failures on both the port side and starboard side of the belly interior using the Sigma variable, which is noted by the blue/green symmetry in the Sigma results. The time at which the compressive failures occurred is also shown, approximately 0.0538 s. and 0.0668 s. after impact for the port side and starboard side, respectively. The Sigma variable depicting the compression failures in the sidewalls are shown in Figure 52.

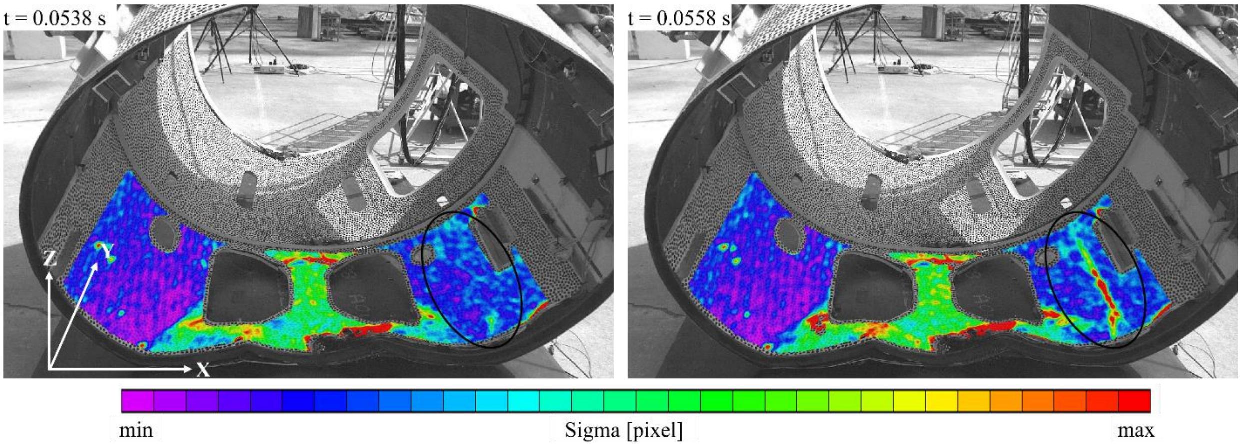

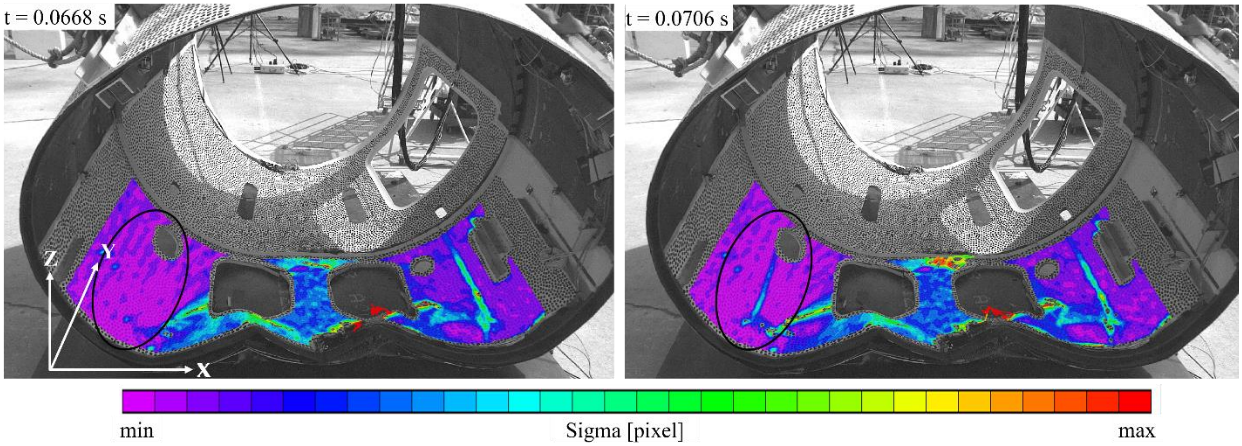

Figure 52 - Compressive fiber failure cracking observed in the belly post-impact. Port side (top) and starboard side (bottom).

Next, principal strains were also examined to determine the strain at which failure occurred. The minimum principal strain-time history, as well as the Sigma time-history, at the location of the port- and starboard-side compressive crack is shown in Figure 53.

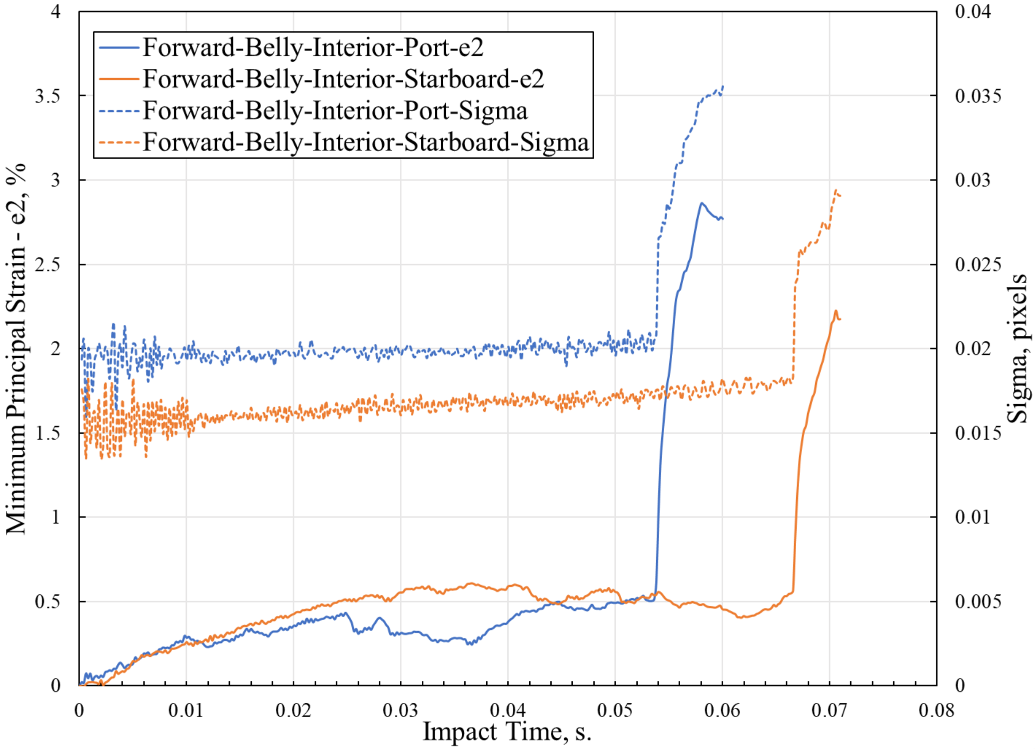

Figure 53 - Compressive fiber failure minimum principal strain-time history.

The minimum principal strain, ϵ2, and Sigma time-history for the port (blue) and starboard side (orange) compressive fiber failure cracking are shown in Figure 53 by the solid and dashed lines, respectively. The port side (blue) shows gradually increasing compressive strain for the first 0.053 s., until approximately

0.5% strain is reached. After 0.053 s., a sharp increase in strain occurs, shown by the sudden, sharp vertical ascent of the line, which is identical to the Sigma (damage) response, signifying a crack has occurred. Investigating the starboard side (orange) in the same manner, the compressive strain is gradually increasing for the first 0.066 s., until a similar level of strain is reached, followed by a sudden, sharp vertical ascent of the line signifying a crack has occurred.

The value of strain after failure is not important since failure has already initiated within the test article and localized damage generally results in erroneous strain values and decreased measurement accuracy, however the failure strain value prior to the onset of damage and cracking, of approximately 0.5%, is an important value to obtain, as this technique is one method to quantitively identify material property failure within the test article. The portion of the test article aft of the center did not exhibit any visible sign of damage when examining the 3D-DIC data.

The accelerometer data were next examined to determine the loading that occurred in the section. Vertical accelerations were first examined starting with the forward, middle and aft belly locations. Note that all accelerations plotted in this report are filtered in accordance with SAE J211 [6] guidelines, unless noted. The belly accelerations were first examined and are shown in Figure 54.

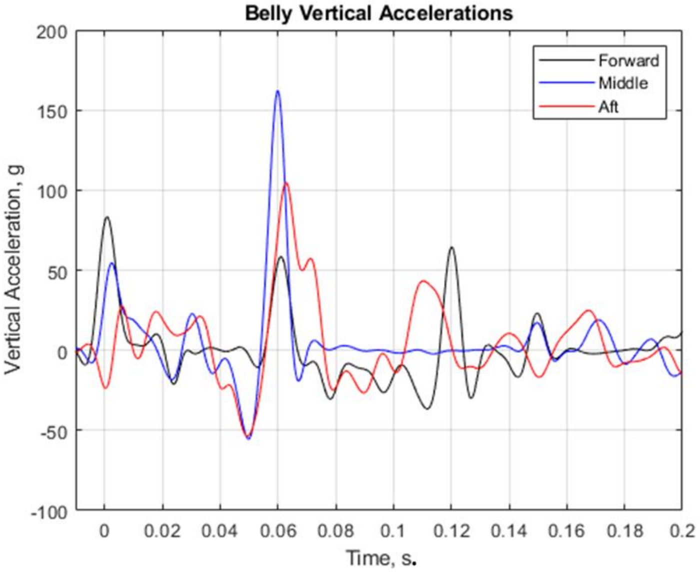

Figure 54 - Belly vertical accelerations.

The forward belly accelerometer recorded approximately 83.2 g at initial impact, followed by 54.3 g for the middle location and 27.3 g for the aft location. Approximately 60 milliseconds (ms.) after impact, a second event occurred. This event is the time where the middle of the test article impacted the load platform, which is shown in the measured accelerations as a second large spike. During the middle impact, the middle accelerometer registers the highest acceleration of the three locations, and additionally higher than the original acceleration measured by the forward accelerometer during the initial impact. The higher magnitude acceleration is due to the presence of an inner metallic stiffener restraining additional failure of the composite in the belly area.

Next comparisons in accelerations as a function of location were analyzed using the belly, sidewall, and ballast accelerometers in order to gain understanding into the deformation differences occurring in the test article. The vertical acceleration data obtained from these locations in the forward portion of the test article are shown in Figure 55 for both the port and starboard sides. Note that for figures showing port and starboard data, the starboard will be presented on the left side and the port on the right, mimicking standing in front of the test article and looking rearward.

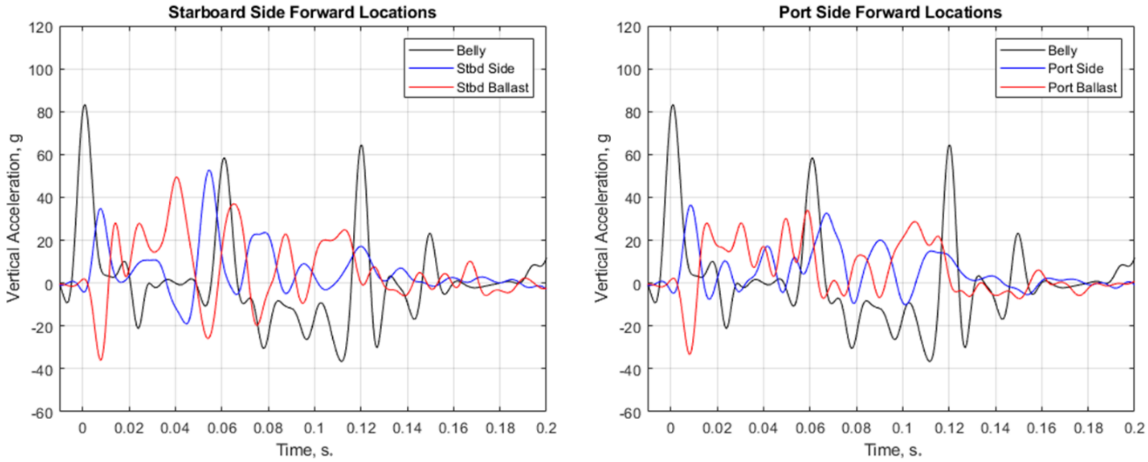

Figure 55 - Forward vertical acceleration location comparisons. Starboard side (left) and Port side (right).

The vertical acceleration data obtained from the belly, side, and ballast locations in the aft portion of the test article for both the port and starboard sides are shown in Figure 56. There are no discernable trends obtained when comparing the results from the three locations in the aft of the test article. The belly exhibits the large spike at the point of impact, while the sidewall accelerometers do not show a discernable pulse shape.

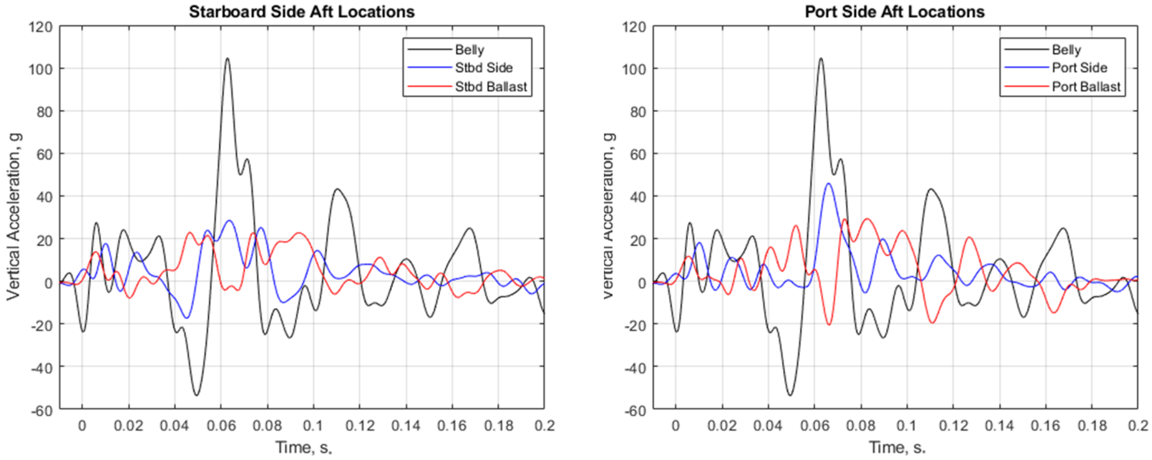

Figure 56 - Aft vertical acceleration location comparisons. Starboard side (left) and Port side (right).

The ballast locations show the potential for a sustained response; however, this response occurs at magnitudes not higher than 30 g for both sides. Investigations into the ballast response itself are examined next for both the horizontal and vertical directions. The horizontal accelerations in the ballast location were examined and the results are shown in Figure 57. There are pronounced oscillations in the data, which appear at all locations examined. The magnitudes of the accelerations are slightly higher on the starboard side than on the port, however, both sides show a defined pulse shape approximating a triangle or trapezoid, and lasting approximately 0.14 s. Peak values on the starboard side of 14.0 g, while the maximum value on the port side is 11.4 g. The oscillation frequency was between 40 Hz and 50 Hz for all sensors.

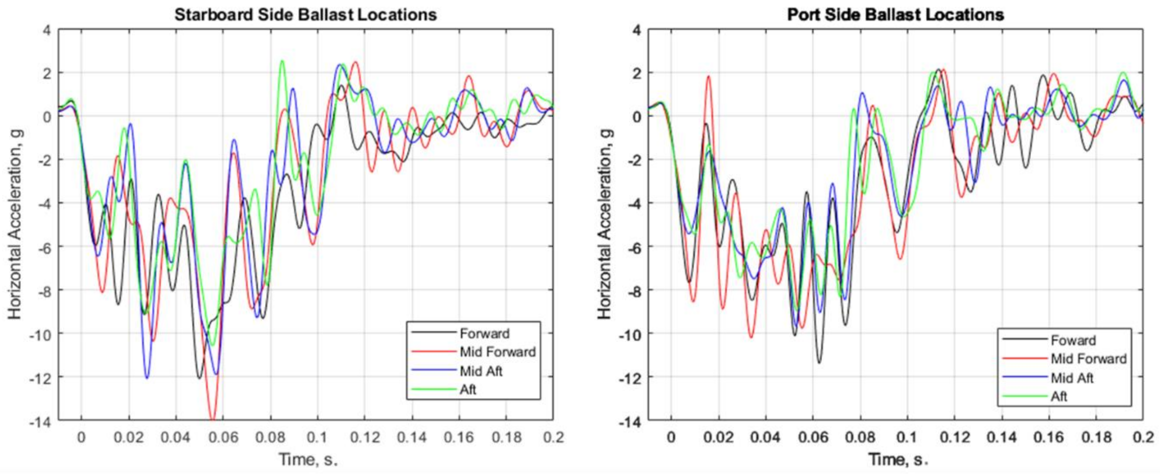

Figure 57 - Ballast horizontal acceleration location comparisons. Starboard side (left) and Port side (right).

The vertical accelerations in the ballast location are shown in Figure 58. Similar to what was examined in the horizontal data, the vertical accelerations show pronounced oscillations in their response. These oscillations are between 38 Hz to 48 Hz, which was in family with the results obtained in the horizontal data. The pulse shape is less defined, but still shows trends of a triangle or trapezoid, with duration of between 0.12 s and 0.16 s.

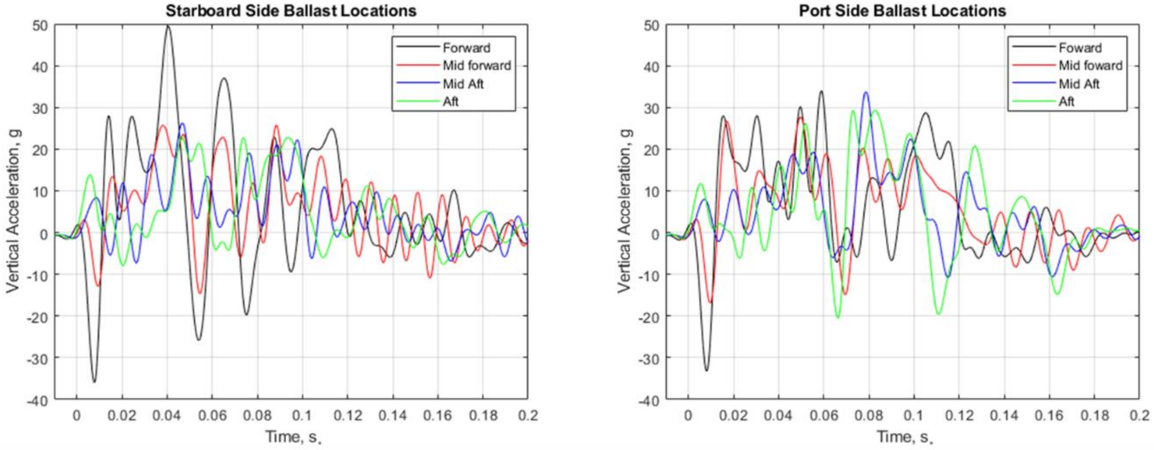

Figure 58 - Ballast vertical acceleration location comparisons. Starboard side (left) and Port side (right).

Finally, lateral accelerations were examined as a function of sensor location. Lateral accelerations were examined to investigate the sidewall motion and loading conditions that occurred during the test sequence during which the test article was undergoing significant delamination and failure. The forward locations were examined first and are shown in Figure 59.

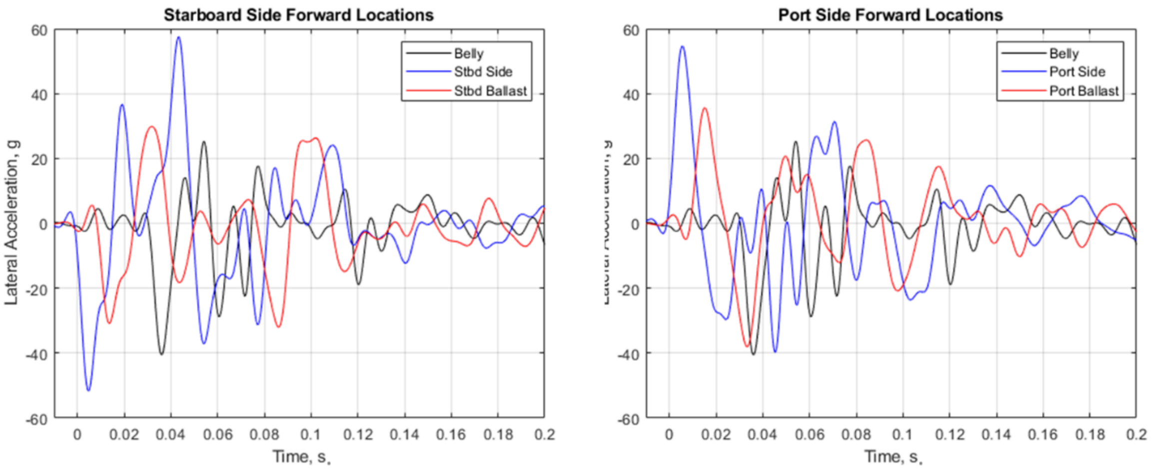

Figure 59 - Forward lateral acceleration location comparisons. Starboard side (left) and Port side (right).

The lateral motion showed pronounced peak values at multiple times after the impact in both the starboard and port sides. The peak value occurring immediately after impact is shown in both the starboard and port side data, in both the sidewall and ballast locations. Note the accelerations will be opposite in sign on opposite sides of the test article. On the starboard side, an outward motion was designated as positive acceleration and inward motion as negative. On the port side, outward motion is designated as negative acceleration and outward motion is designated as positive. When examining the sidewall data, the immediate motion of the test article after impact was inward motion until approximately 0.02 s. after impact, after which the test article exhibited sustained outward motion until approximately 0.08 s. after impact. Unlike the ballast data, the lateral accelerations did not show a defined pulse shape of a triangle or trapezoid, but did show a total pulse duration of between 0.12 s. and 0.16 s.

This pulse duration of the lateral accelerations aligned well with the 3D-DIC displacements of the sidewall. The sidewall displacements were measured using virtual extensometers placed within the post-processed data set of the interior of the Forward Section, at three locations (forward, mid-barrel in front of stiffening ring and mid-barrel behind the stiffening ring) between the port side and starboard side at approximately the same vertical height/position. The change in length, ΔL, was then extracted and plotted, as shown in Figure 60. The port and starboard side exhibited large combined outward deformation (between 5 in. and 8 in.) during the first 0.15 s., followed by lower amplitude oscillations of approximately 1 in. After 0.4 s., the photogrammetry was unable to correlate during the remainder of the event due to the angle of the test article relative to the cameras.

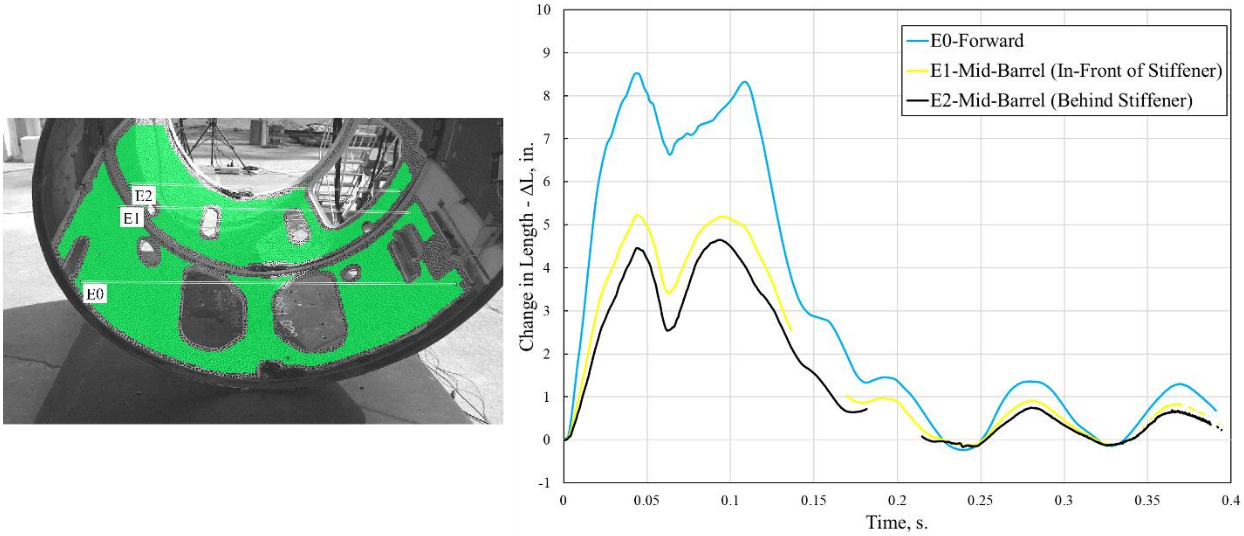

Figure 60 – Outward displacements of the sidewall.

Aft location lateral acceleration data is shown in Figure 61. Aft acceleration data exhibited less oscillations than the forward data, and clearly showed the middle belly impact event at approximately 0.06 s. after impact. Prior to this event, the data showed the test article sidewall motion inward which occurred between 0.037 s. and 0.055 s. after impact. Then, the belly middle impact occurred, which causes the behavior of the sidewalls to reverse and begin to protrude outward. After the outward motion, the sidewalls then reversed again, moving inward between 0.074 s. and approximately 0.1 s. This data aligns well with the timing shown in Figure 44 and Figure 45, which show maximum vertical compression occurring approximately 0.09 s. after impact.

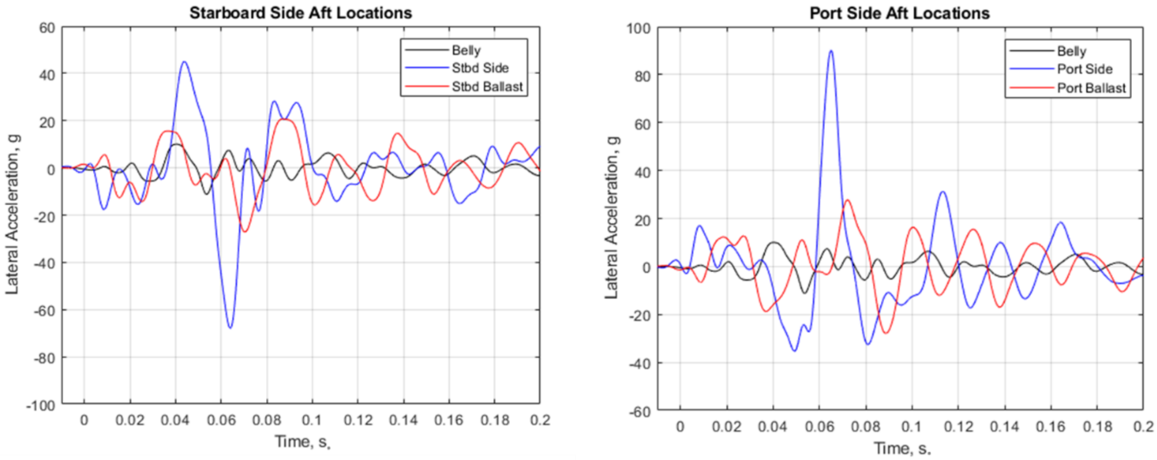

Figure 61 – Aft lateral acceleration location comparisons. Starboard side (left) and Port side (right).

Following the full-scale drop test of the Forward Section, an additional post-test set of full-field 3D-DIC data were computed using the static post-test shape of the test article and comparing it to the undeformed pre-test shape, which was measured prior to the test. These two measurements were compared to each other and a delta displacement measurement, representing permanent deformation, was obtained. An example of this measurement is shown in Figure 62, for which the vertical direction deformation data are plotted.

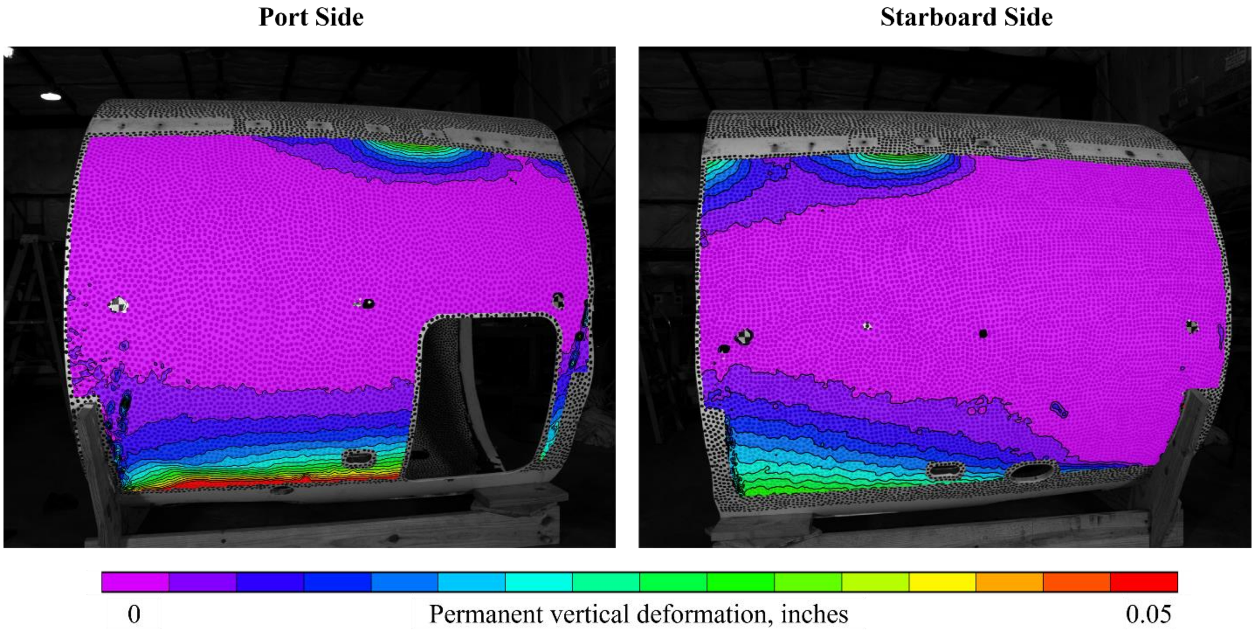
Port Side

Starboard Side

Figure 62 – Permanent vertical deformations. Port side (left) and Starboard side (right).

The permanent deformation in the vertical direction reveals two key findings. The first is there is a large amount of permanent vertical deformation in the forward belly area, which was the area that made first contact with the impact surface. The localization of the red also indicates that this permanent deformation is localized to the area immediately surround the two large openings of the forward belly section. There is also some additional deformation near the top of the test article at locations near the added ballast due to ballast motion during the test. This deformation is also localized toward the forward end of the test article.

The second item to note is the mid-height area of the test article exhibits little to no permanent vertical deformation. This data indicates that even though there was large amount of permanent deformation in the belly section, a large majority of the test article returned to its original pre-test shape. The obtained data were very helpful because these types of deformations would not be readily apparent through normal post-test inspections and provided insight into the nature of the behavior of the test article during the test. Additionally, these findings were used when examining the results from the full-scale simulations using the developed computational models, described next.

Post-test 3D point cloud scans were also conducted at the test area on the Forward Section immediately following test in order to capture the final resting position of the test article, along with shape, deformation and damage information. The 3D point cloud scans are shown in Figure 63.

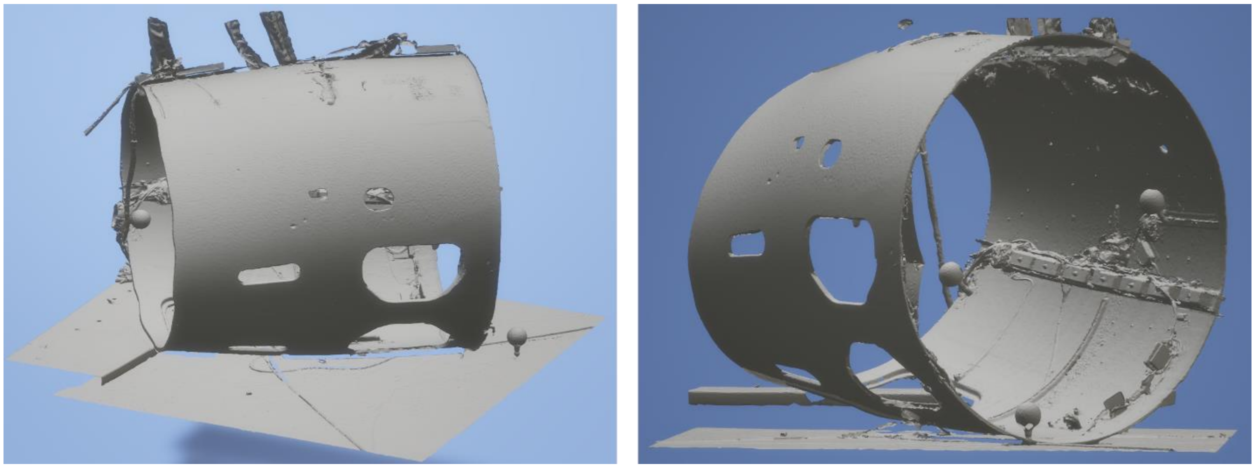

Figure 63 – Post-test 3D point cloud scan. Starboard side/belly (left) and Forward/IML (right).

## Full-Scale Simulations – Forward Section

After the Forward Section test was conducted, the FE model of the Forward Section was updated to match the as-tested configuration. The precise ballast mass integration and instrumentation used in test was updated within the FE model. The ballast blocks, which were attached to the test article using aluminum c-channels mounted across the test article, was represented in the FE model using point masses rigidly fixed to the composite sandwich elements through constrained nodal rigid bodies (CNRBs) defined at the c-channel mounting locations. The belly and sidewall accelerometers which were mounted to the interior skin of the test article and the ballast mass accelerometers were fixed to the test article through the c-channel attachment were represented within the model using seatbelt accelerometer models attached at the representative locations using CNRB attachments. A schematic of the Forward Section FE model with instrumentation and added mass is shown in Figure 64. The Forward Section test article weighed 760 lb. with all ballast mass and instrumentation included. The developed Forward Section FE model weighed 740 lb. compared to the 760 lb. weight of the test article. The slight difference in model and test article weight can be attributed to geometric simplifications made in the reverse engineering process. Although the mass of the FE model could have been artificially altered by adjusting material model density, this step was not taken because there was not enough information gathered from the test article to determine whether artificially adding mass across the entire structure would improve or worsen the estimation of test article CG.

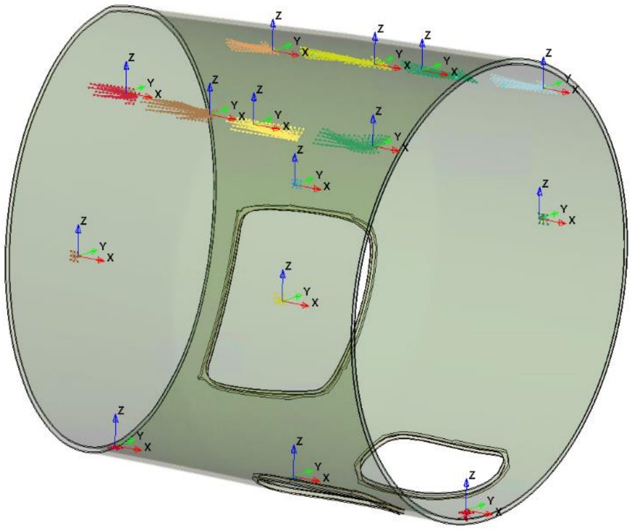

Figure 64 – Schematic of Forward Section FE model showing instrumentation and mass CNRB locations.

An FE model of the steel plate impact surface was next generated to represent the tested environment. The impact surface was modeled using three different methods to determine the most realistic way to replicate the boundary conditions of the test. All three methods included a model of the steel plate and pedestal load cells, modeled using solid elements with an elastic material model of steel. The models differed in how they represented the boundary at the feet of the steel plate. The first model fully constrained the feet of each pedestal load cell in space using a nodal constraint. The second model included a rigid wall contact below the feet. The third model included a solid element model of the concrete surface below the steel plate with the concrete model using an elastic material model. The concrete model was fixed in space using a nodal constraint along the bottom of the part. An automatic surface contact was applied between the concrete and steel plate in the third model configuration. Each boundary condition model was simulated using the reverse engineered Forward Section FE model in the tested configuration. A schematic of each model and resulting comparison of measured to predicted force in the platform load cells is shown in Figure 65. In the nodal constraint boundary condition model, oscillation frequency in the predicted load cell force is close to double what was measured. These results indicated the motion of the steel plate was over constrained at its boundary with the nodal constraint boundary condition. Both the rigid wall and elastic element boundary condition improved the frequency of the predicted force in the platform load cell. Both the rigid wall and elastic element contact boundary conditions only constrain motion of the steel plate in the downward direction which is more realistic to the tested condition. In both models load cell force was well predicted over the first 0.2 s. post impact. After this time, the force oscillations predicted by both models dampens out at a faster rate than was measured. The primary load transfer from plate into the test article occurred before 0.2 s. and thus differences after this timeframe were not considered essential to prediction of the impact response of the test article. Based on the results of the boundary condition evaluation, the rigid wall contact setup was used to model the test environment as it provided a simpler model then the elastic element contact while also providing realistic prediction of load during the impact event.

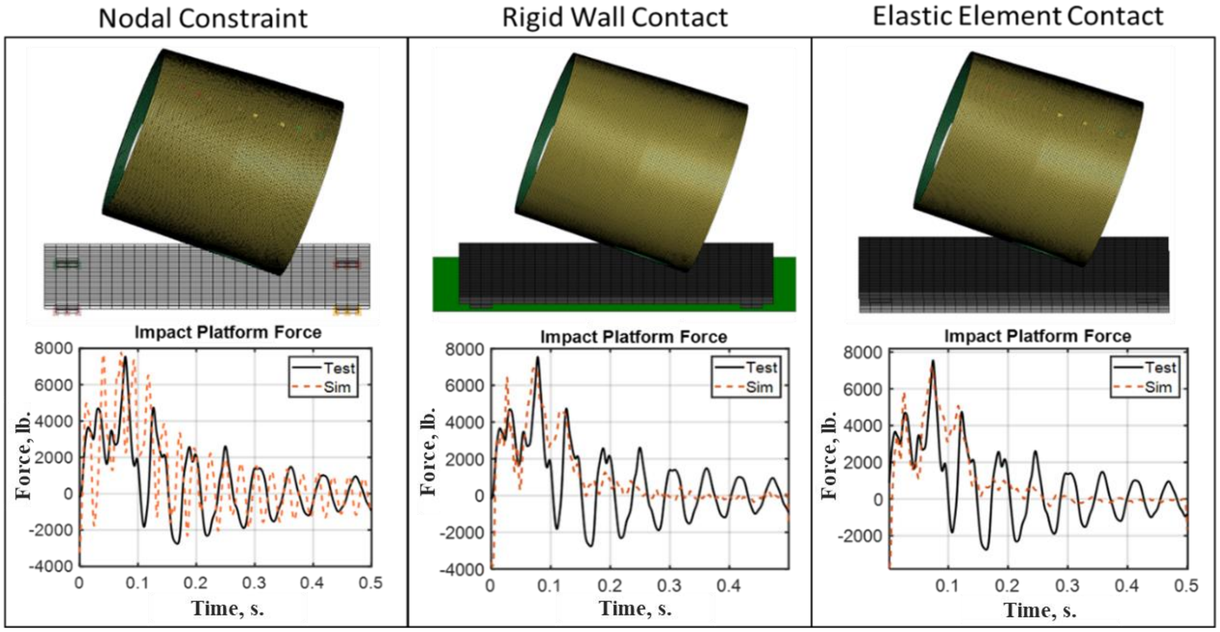

Figure 65 – Comparison of model boundary conditions on impact force predictions.

After updating the Forward Section FE model and generating the representative test environment model, simulation of the test was ready to be conducted. The measured impact velocity and pitch angle conditions were implemented within the simulation using an initial velocity definition on the test article part and by adjusting the pitch relative to impact surface. The test was simulated using LS-DYNA SMP version R13.10 single precision on a Linux computer cluster. The LS-DYNA solver was changed in the test article simulations from what was used in the component analysis due to an update of the Linux computer cluster used. Comparative simulation between R10.10 and R13.10 was conducted with the Forward Section FE model. Results showed no significant change in predicted response. Simulations were carried out to a termination time of 0.3 s. using eight processors. The simulation had an approximate run time of six hours.

The first aspect of model correlation to the test data evaluated was prediction of composite failure observed during test. The Forward Section test showed failure of the composite structure along the impact edge of the test article during the impact event. The impacting edge experienced delamination to both sides of the impact centerline, forming a “w” shape in the composite structure. The region behind the impact edge also flattened during the impact, exhibiting delamination of the composite sandwich up to the midline of the test article. At peak deflection the fuselage took on a slight oval shape. An image of the test article and FE model at peak deformation is shown in Figure 66. Damage to the composite structure along the impact edge up to the front midline of the test article was predicted by the reverse engineered model, though the distinct “w” shape observed in test was not replicated. The damage mechanism observed in test was primarily bond failure between the honeycomb and composite skin and delamination of the composite layers. This bond failure between honeycomb and the composite skin was predicted by the model though, delamination of the composite layers was not captured due to the simplification of the composite layup as a uniform solid element formulation.

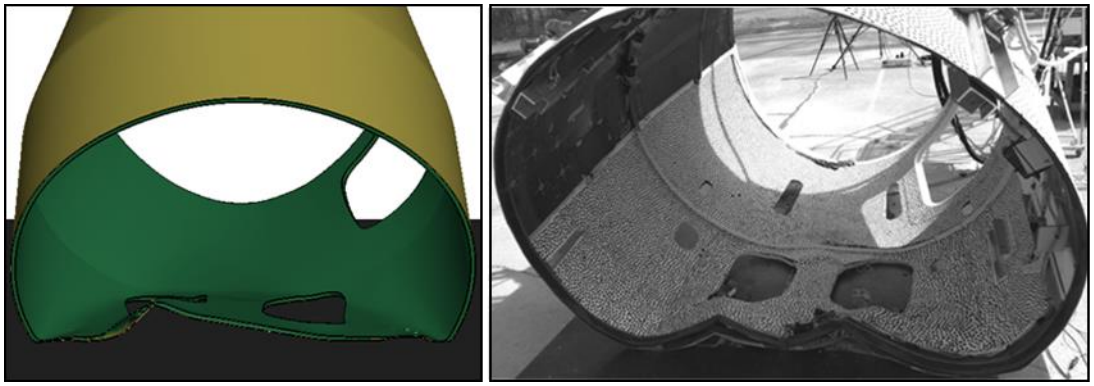

Figure 66 – Composite damage observed in Forward Section test and model prediction.

Next, displacement of the port side outer side wall in the Forward Section, measured during the test using 3D-DIC, was compared between test and simulation. Peak vertical displacement was compared in order quantify the effectiveness of each model in predicting changes in occupant compartment volume during impact. Comparison of vertical displacement at peak deflection in the test and each model is shown in Figure 67. The test measurement was limited to the area of test article perpendicular to high-speed video taken during the test and is thus compared along the horizontal face of the fuselage section. Overall, the FE model predicted greater vertical displacement than what was measured in the test. The overprediction was approximately 3 in. of displacement at both the forward and aft ends. The overprediction of displacement at the forward and aft end of the test article is likely due to increased damage in the floor of the model resulting in greater displacement of fuselage, while retaining similar overall shape to the test article.

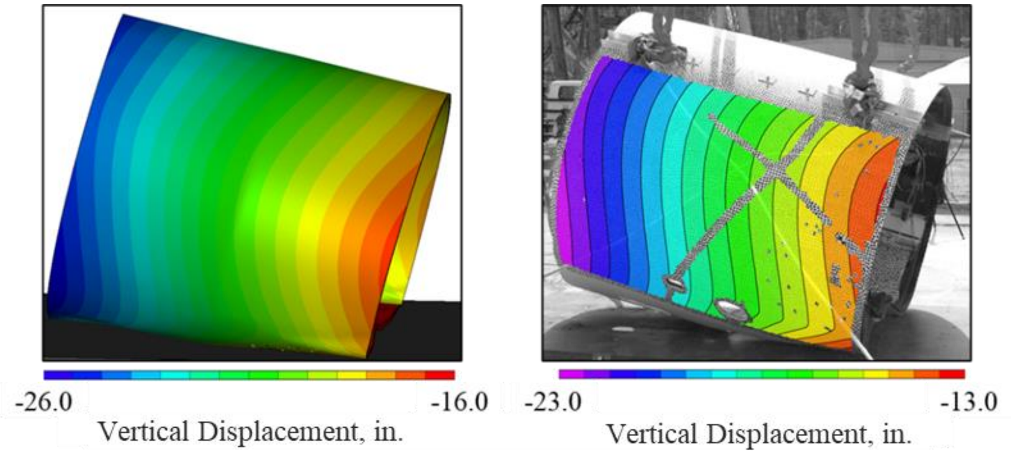

Figure 67 – Vertical displacement measured in Forward Section test article and predicted in the Forward Section FE model.

Acceleration time histories recorded in the test article were compared to those predicted the FE model to quantify the capability of the model to predict energy transferred from the impact into the occupant compartment of the composite structure. Acceleration data were originally filtered using a channel frequency class (CFC) 60 filter in accordance with SAE J211 guidelines. The data produced were highly oscillatory which made comparison between test and simulation difficult. To improve data legibility, a Butterworth low-pass filter with a 60 Hz cutoff frequency was applied to both test and simulation data. An example comparison between the CFC 60 and 60 Hz Butterworth filter applied to the forward port side ballast horizontal acceleration from test and simulations is shown in Figure 68. The lower cutoff frequency filter was found to retain overall shape and magnitude of the acceleration pulses while reducing the oscillatory responses recorded in both test and simulation data and was thus used in test to analysis comparisons.

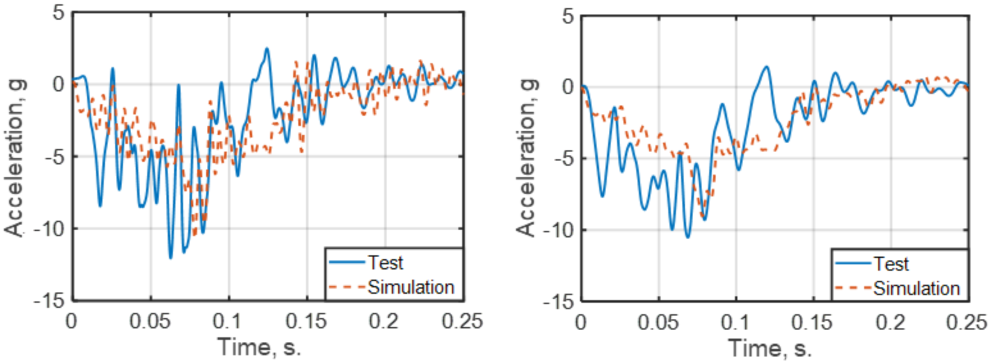

Figure 68 – Comparison of CFC 60 filter (left) and 60 Hz Butterworth filter (right) applied to measured and predicted acceleration response.

The accelerometers attached to the ballast mounts provided the most consistent accelerometer time histories during the impact event to allow for comparison between test and simulation. The accelerometers mounted directly to the vehicle skin tended to record large signal oscillations and in certain cases became detached from the vehicle during the impact event. Horizontal acceleration time histories measured in test and predicted using simulation at the forward, middle, and aft ballast locations are shown in Figure 69. Acceleration response was largely symmetrical across the width of the test article and thus only portside responses are compared to simulation in order to reduce repetitive evaluations. Peak horizontal acceleration and time of peak was well predicted across all ballast locations. The initial rise in horizontal acceleration was underpredicted in all locations. After the initial underprediction the acceleration time history shape was predicted by the model. Overall, consistent horizontal acceleration prediction correlation was recorded across the length of the Forward Section test, indicating close prediction of the longitudinal stiffness of the test article by the FE model.

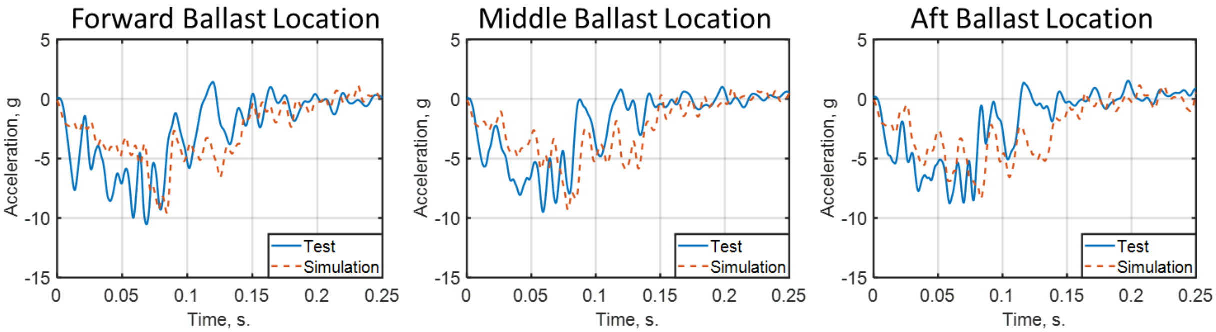
Forward Ballast Location
Middle Ballast Location
Aft Ballast Location

Figure 69 – Forward Section portside ballast horizontal acceleration time history comparisons.

Lateral acceleration time histories measured in test and predicted using simulation at the forward and aft ballast locations are shown in Figure 70. Lateral acceleration on the middle ballast locations were not recorded during test. Differences in lateral acceleration correlation can be observed between the forward and aft end of the test article. In the forward location of the test article, the model predicts peak acceleration but underpredicts initial acceleration response. In the aft location, the model predicts initial acceleration response but unpredicts peak value. In both sections, the model accurately captures the oscillating acceleration shape which is measured in the lateral direction. In the forward location there is a sharp rise in acceleration at impact which is not captured by the model, similar to what was observe in the horizontal acceleration. This sharp initial rise in lateral acceleration is not observed in the aft location, which results in improved prediction of initial acceleration at this location.

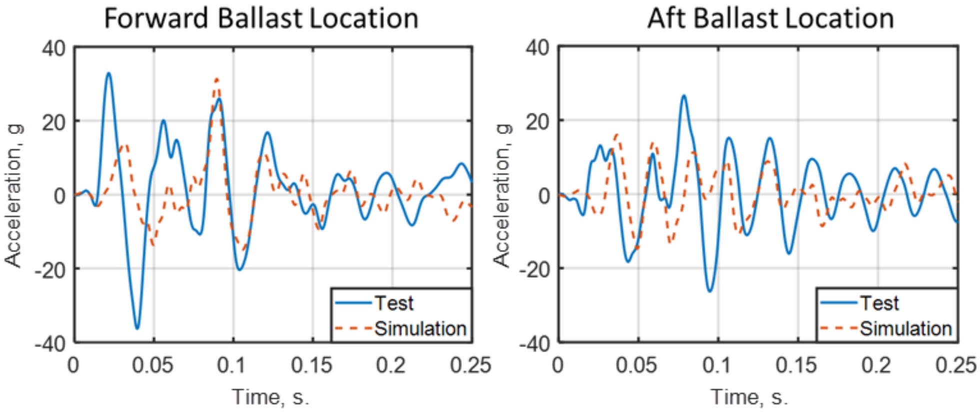

Figure 70 – Forward Section portside ballast lateral acceleration time history comparisons.

Vertical acceleration time histories measured in test and predicted using simulation at the forward, middle, and aft ballast locations are shown in Figure 71. Overall, the model predicted acceleration shape and peak value in the vertical direction. Differences in vertical acceleration correlation can be observed between the forward and the middle and aft end of the test article. In the forward location, there is a large negative acceleration measured at the onset of impact, while this acceleration is not observed in the middle or aft locations. The model does not effectively predict this initial negative acceleration and thus shows improved correlation in the middle and aft sections. After this difference in initial acceleration, correlation levels are similar across the remaining time history with the model predicting acceleration shape and rise to peak acceleration at approximately 0.075 s. In the forward locations of the test article, the model predicts peak acceleration but underpredicts initial acceleration response. In general, the Forward Section FE model captured acceleration shape and peak in each direction across the length of the test Forward Section test article. The primary discrepancy observed between test and simulation was an acceleration spike towards the front of the cabin which occurred at the time of impact and was not predicted by the simulation.

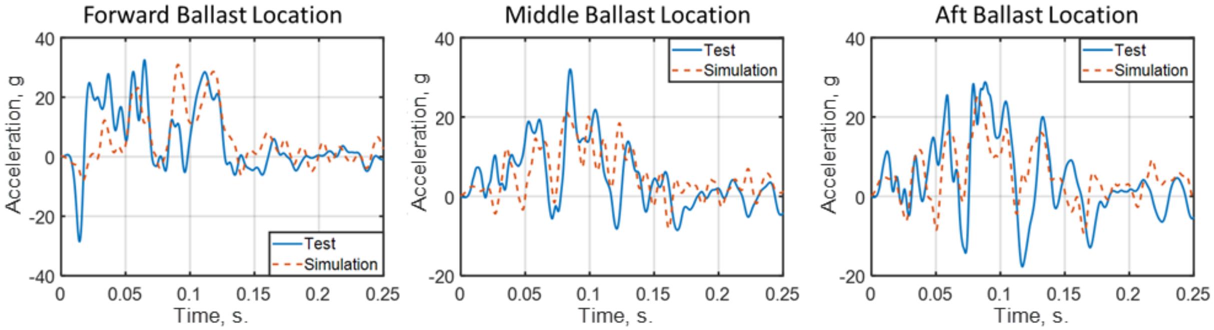

Figure 71 – Forward Section portside ballast vertical acceleration time history comparisons.

By examining the comparisons between the Forward Section FE model and the test data, confidence was gained regarding the use of the reverse engineered techniques and the generated material property data. The same techniques will be utilized in simulations for the Aft Section test, which is described in the next section.

## Full-Scale Testing – Aft Section

The Aft Section test article was prepped similarly to the Forward Section. After being cut out of the section, the test article was moved to the prep area to be painted and fitted with ballast and instrumentation. The Aft Section is shown in Figure 72, standing on its forward end, prior to test buildup.

Figure 72 – Aft Section test article.

Ballast was added evenly spaced between at the mid-height level, or approximately 36 inches up the section height. Four 25-lb. masses were used on each side, spaced approximately 7 inches apart mounted into c-channels for support. The lifting points were located on the outside of these locations and used to lift and orient the test article to the correct test orientation. Aft section ballast location on the port side is shown in Figure 73.

Figure 73 – Aft Section ballast location.  Port side shown.

The test article was instrumented similar to the Forward Section.  At the belly locations, two triaxial accelerometers were mounted at the forward and aft locations.  On the ballast locations for both the port and starboard sides, a triaxial accelerometer was mounted in the forward location, while biaxial accelerometers measuring vertical (z), and horizontal (x) directions were mounted in the middle and aft locations.  Finally, accelerometers were mounted to three locations on the ceiling of the test article – forward, middle and aft.  The forward and aft locations contained biaxial accelerometers measuring horizontal and vertical accelerations only, while the middle location was a triaxial measuring all three directions.  Both the port and starboard sides were painted with a stochastic black and white speckle pattern for use with full-field 3D-DIC.  Unlike the Forward Section, the interior of the test article was not speckle coated and 3D-DIC was not conducted.  As with the data presented in the Forward Section, the 3D-DIC results are used in conjunction with the accelerometer data when examining test behavior and response. An illustration of the instrumentation and ballast is shown in Figure 74.  All data were collected via offboard data acquisition systems using an unbillable cable bundle at a rate of 25 kHz.  An IRIG timecode signal was also used to synchronize the camera and data acquisition system (DAS) systems and the impact surface was the same load platform used in the forward test.

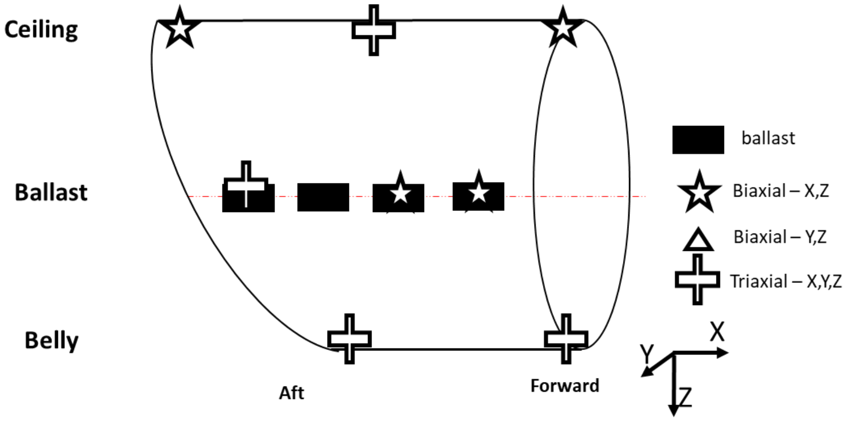

Figure 74 – Aft Section test article instrumentation.

The final drop weight was 490 lb. Lifting rings were added to the outside of the test article, opposite the forward and aft ballast blocks and used to lift the test article to the drop height. A nominal impact condition of 30 ft./s. vertical velocity with a 20 degree nose up pitch was chosen for the test. The Aft Section test setup is shown in Figure 75. There was a large opening in the belly, and therefore the impact location was a very small area for which to contact. It was intended to contact this small area to induce large amounts of deformation and failure in this and the surrounding areas. In addition, the large opening would allow for the forward belly area to experience a second contact due to the expected rotation of the test article upon impact. The Aft Section test occurred on March 23, 2022. The test article was raised 14 feet, measured at lowest portion of the belly, and then dropped onto the impact surface via a release hook. A picture of the test article, at its release height is shown in Figure 75.

Figure 75 – Aft Section test article at drop height.

The test article impacted the load platform with a vertical impact velocity of 26.7 ft./s. and a pitch up angle of 17.9 degrees. The general test sequence is described as follows:

- The test article first contacted the impact surface at the aft edge, thus initiating composite failures in this region.
- After the aft edge made contact, the test article rotated such that the forward portion of the test article in front of the belly opening made contact with the impact surface.
- After full contact was made, the test article compressed into the impact surface until a maximum vertical deflection was reached.
- Afterward, the test article rebounded, and landed upright in its final, post-test position.

An image sequence of the test as recorded by the starboard side camera depicting these notable events with timing is shown in Figure 76.

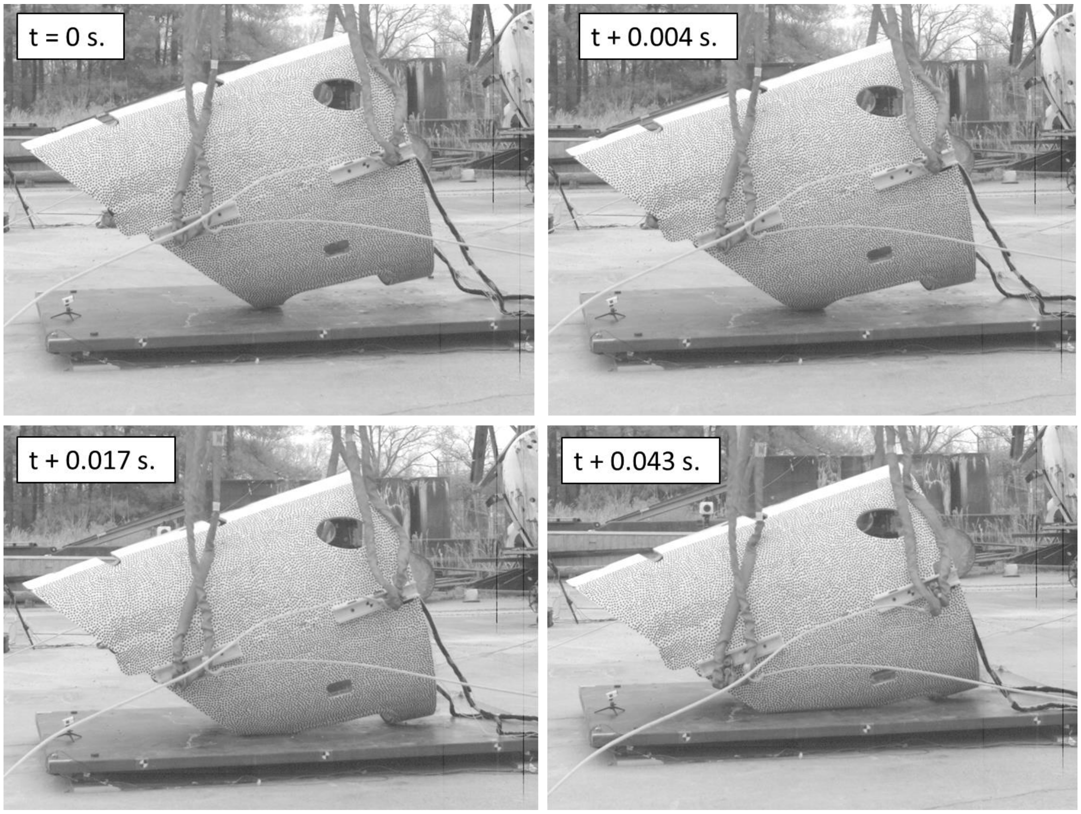

Figure 76 – Starboard side image sequence.

The image from this camera provided relevant information to identify some of the notable events that occurred throughout the test sequence. The upper left image shows the test article at impact. The pitch up orientation of the test article does allow for the small aft portion of the belly to contact the impact surface first. Almost immediately after impact, at 0.004 s., the contact at this location has caused the localized fracture in the aft belly impact location on the test article, as shown in the upper right image. It is also at this time where the measurement accelerometers have debonded from the inner surface. The lower left image shows the test article 0.017 s. after impact, which is the time at which the forward portion of the test article contacted the impact surface. The vertical motion of the test article continues until 0.043 s. after impact, which is at the point that the maximum vertical deflection of the test article has occurred. The same sequence of events from a camera located forward of the test article, facing aft and examining the interior, is shown in Figure 77.

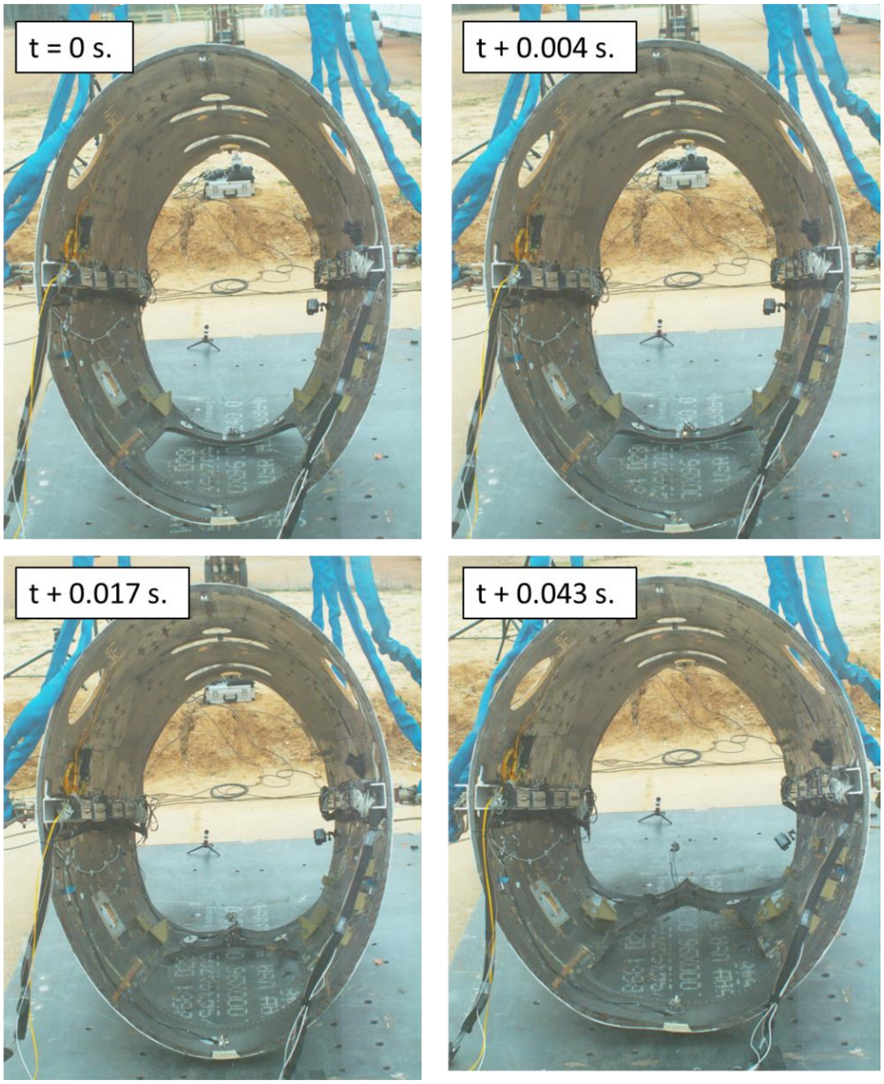

Figure 77 – Interior image sequence.

The impact is shown in the upper left image in Figure 77. The aft belly area, which is shown in the background for the image series can be seen to be in contact with the impact surface. The upper right image, which was acquired almost immediately after impact, shows the first fracture occurring in this same area. The lower left image shows the time of the forward belly area impact, also noticing that the aft belly section has begun to protrude inward due to the fracture. The lower right image shows the test article at maximum vertical deflection, which is depicted by the test article shape being noticeably different. Also shown in the lower right image is the large amount of inward protrusion in the aft belly section.

The vertical displacement corresponding to the image sequences shown in Figure 76 and Figure 77, as measured using 3D-DIC, is shown in Figure 78. Note that the maximum and minimum values of the contour scale, as designated by the red and purple colors respectively, are adjusted for each notable event.

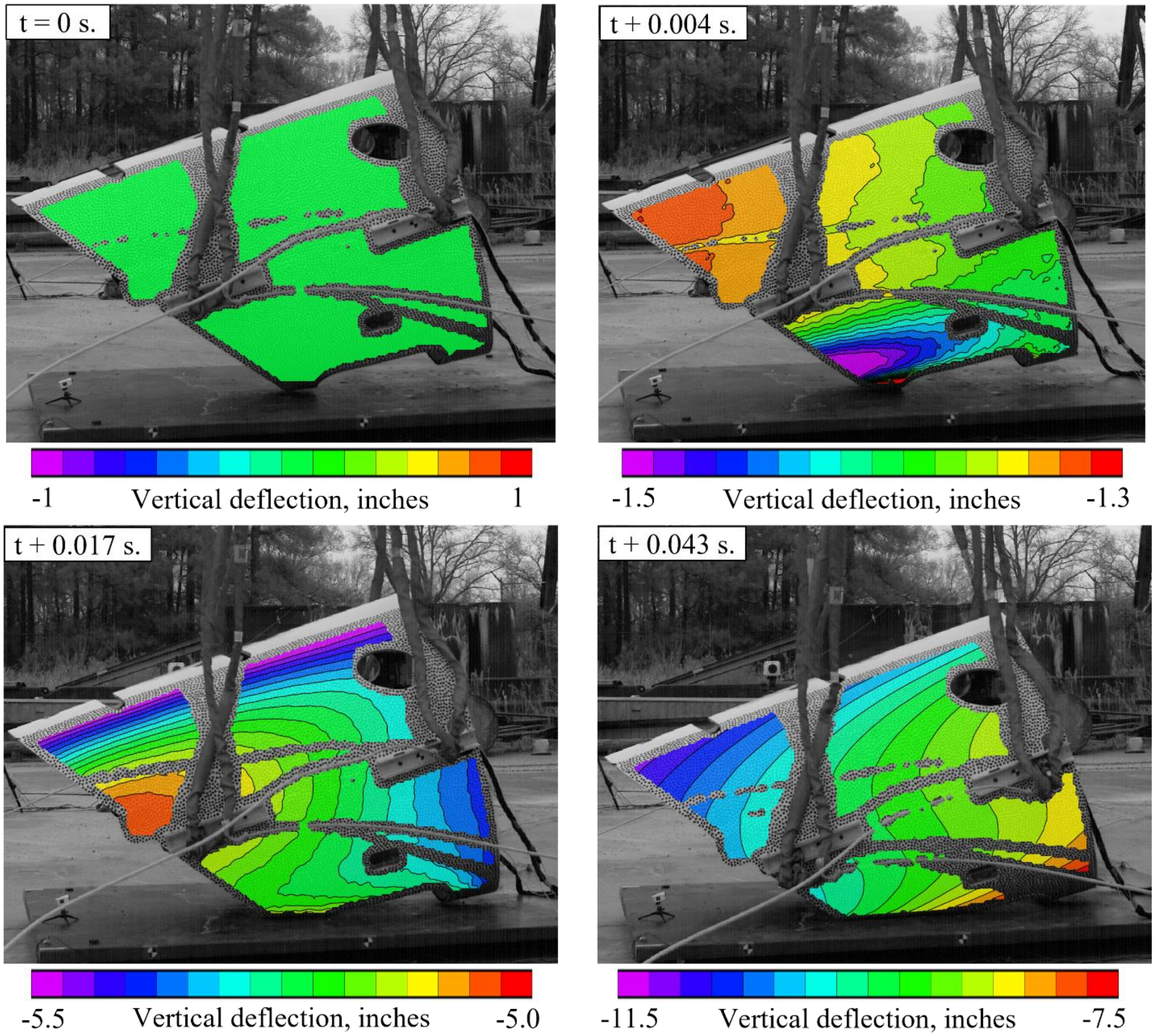

Figure 78 – Vertical deflection of starboard side image sequence.

An additional frame taken from the aft side high speed camera is shown in Figure 79. This image shows the belly skin area post-failure and protruding into the interior of the test article. As with the Forward section test, this shape resembles a “w” with the center of the belly being the interior vertex. This type of failure only occurred in the aft belly area. The forward belly area exhibited deformation, but not complete fracture.

Figure 79 – Aft Section internal view showing belly failure.

After the test article came to a rest, post-test inspection began. The post-test inspections designating the notable failures in the interior of the test article are shown in Figure 80, which were mainly concentrated in the belly area of the test article, immediately surrounding the forward and aft impact locations. A close-up image of the belly sections is shown in Figure 80, noting the large opening located between the forward and aft sections.

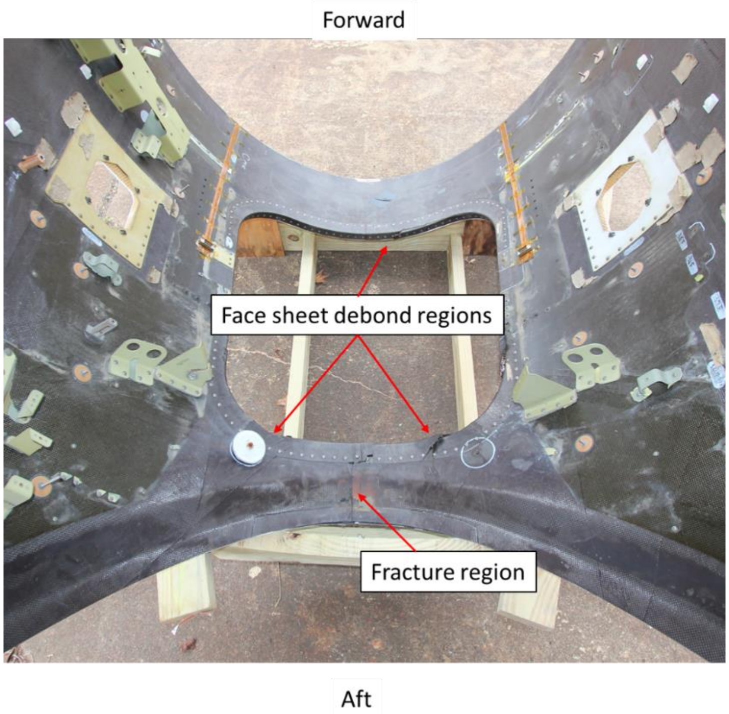

Figure 80 – Composite failures on belly.

The aft belly region, which is shown in the bottom of Figure 80, is the area that impacted first. There is a longitudinal fracture running along the middle of the belly section, in the position that contacted first. The fracture of this area led to facesheet debonding on the composite sandwich structure on the interior of the opening in both the forward and aft areas. The forward belly area did not exhibit any noticeable signs of fracture of other damage other than the debonding in the opening. No signs of fracture could be due to the forward belly area not making full contact with the impact surface during the impact, which is demonstrated by examining the position of the forward belly area in the lower right image of Figure 77. Another view of the facesheet debonding region is shown in Figure 81.

Figure 81 – Composite failures on belly. Forward viewing aft.

The view in Figure 81 is oriented in front of the test article, viewing aft. The facesheet debond regions are highlighted. Note that in the foreground of the image is the forward belly section, with no noticeable damage depicted. When focusing on the aft belly area of the test article, there were additional outer skin cracks that occurred approximately one-quarter of the way up the test article, on both the port and starboard sides. The location and closeup view of the crack on the port side of the test article is shown in Figure 82.

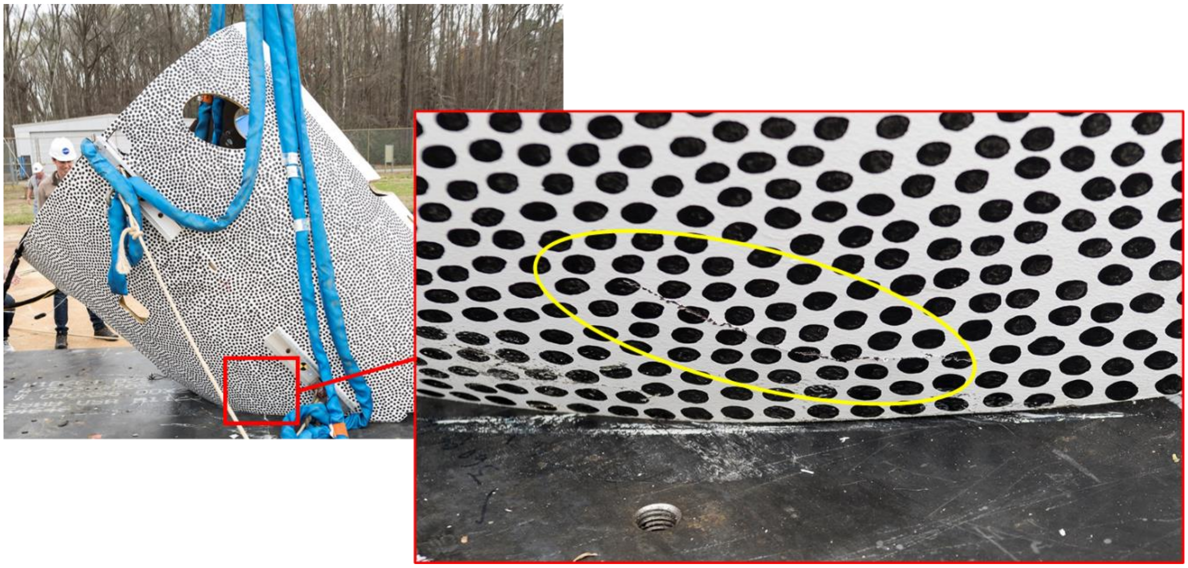

Figure 82 – Composite sandwich outer layer tensile fiber failure.

The cracks were representative of a tensile failure in the outer skin of the sandwich composite facesheet. The tensile failure cracks appeared in the same location as the delamination on the aft edge of the fuselage structure and were due to the large amount of bending and ultimate fracture that occurred in the aft fuselage area. Both the facesheet failure and the edge delamination on the aft end of the test article are shown in Figure 83.

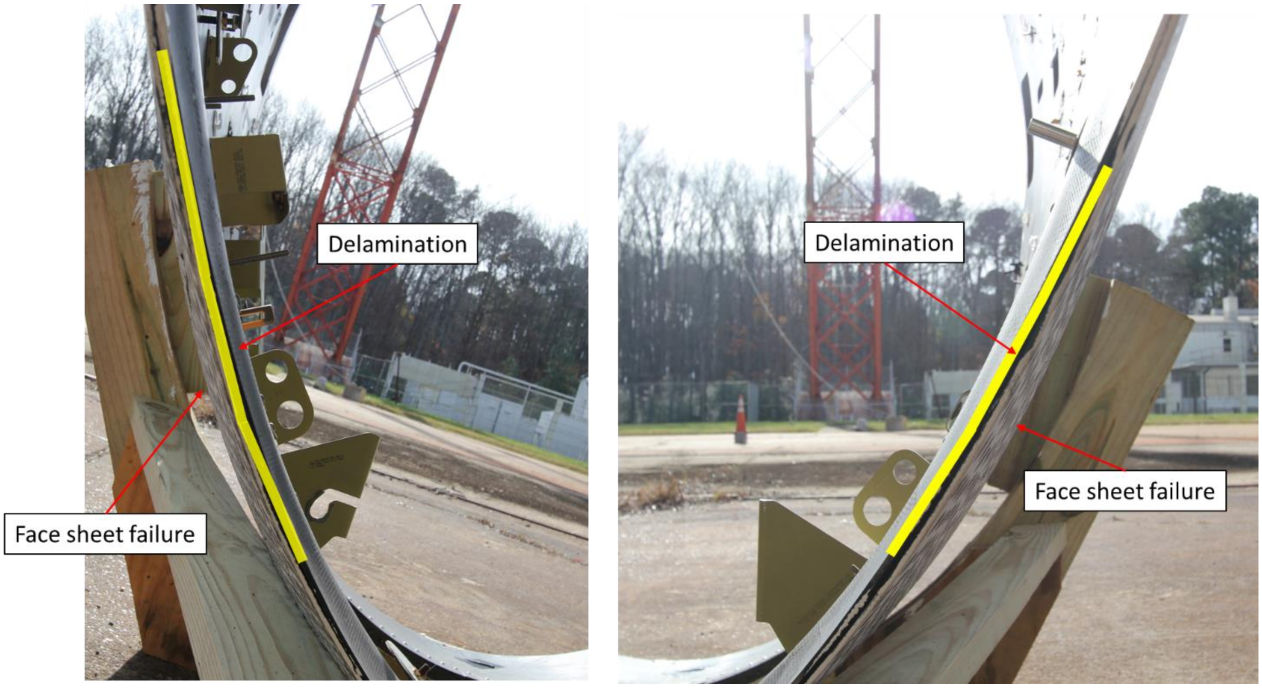

Figure 83 - Edge delamination. Port side (left) and starboard side (right).

The delamination was associated with the inward motion of the test article skin due to the impact point. As the belly area fractured and begin to protrude inward, it created bending in the walls, with the outer wall being in tension and the inner wall in compression. The tension on the outer skin caused the outer fibers to break, while the combination of tension and compression caused the composite to delaminate at its midplane on the aft edge. It should be noted that the aft edge is a solid ring of carbon fiber, and the only part of the structure that is not a sandwich composite. The delamination lengths are highlighted in yellow in Figure 83.

The collected acceleration data were next examined. The accelerations at the belly locations were not obtained because the sensors debonded from the attachment points immediately upon impact. Because using a fastener in the Forward Section appeared to affect the failure induced form the test, in the Aft Section test all accelerometer locations were bonded onto the structure using epoxy adhesive in order to mitigate the effects of the fasteners. The bond strength at the belly locations was not sufficient, and the sensors in both locations debonded. However, accelerations at the sidewall ballast locations were collected. The vertical accelerations obtained from the sidewall ballast are shown in Figure 84, with the starboard locations on the left and the port on the right.

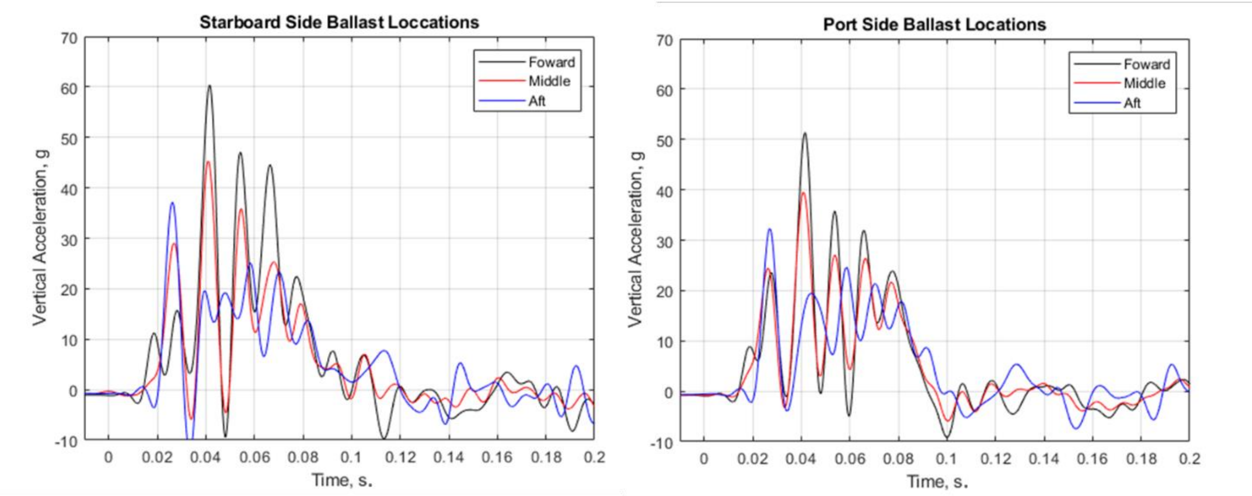

Figure 84 - Ballast vertical acceleration location comparisons. Starboard side (left) and Port side (right).

The collected accelerations at the ballast locations shows distinct trends present. The first is that the port and starboard sides pulse duration is approximately the same length at 100 ms. The second trend is a regular oscillation of approximately 75 Hz present in both sides in the data. The oscillations reach approximately 60 g on the starboard side and could be the due to the vibration in the test article or ballast mass upon impact. However, if the data are filtered at a lower cutoff frequency of 60 Hz, there is a noticeable plateau present which ends at 0.8 s. after impact. The plateau using a lower cutoff frequency of 60 Hz is shown in Figure 85.

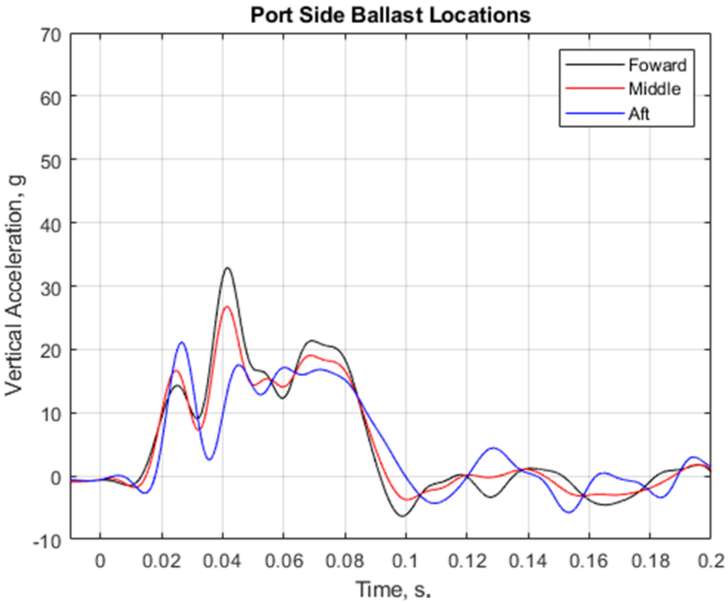

Figure 85 - Port ballast vertical accelerations filtered at 60 Hz cutoff frequency.

Horizontal accelerations were next examined. They are plotted in Figure 86. In the horizontal direction, there was difficulty interpreting the data. The horizontal direction was examined due to the nature of the slanted drop and the effect the pitch would have on the overall response, but the horizontal accelerations were unlike the vertical. There was no defined pulse shape and there were large oscillations present in the data, which was also shown for the vertical data. The oscillation peaks exceeded 10 g for the middle and aft locations but were below 10 g for the forward location.

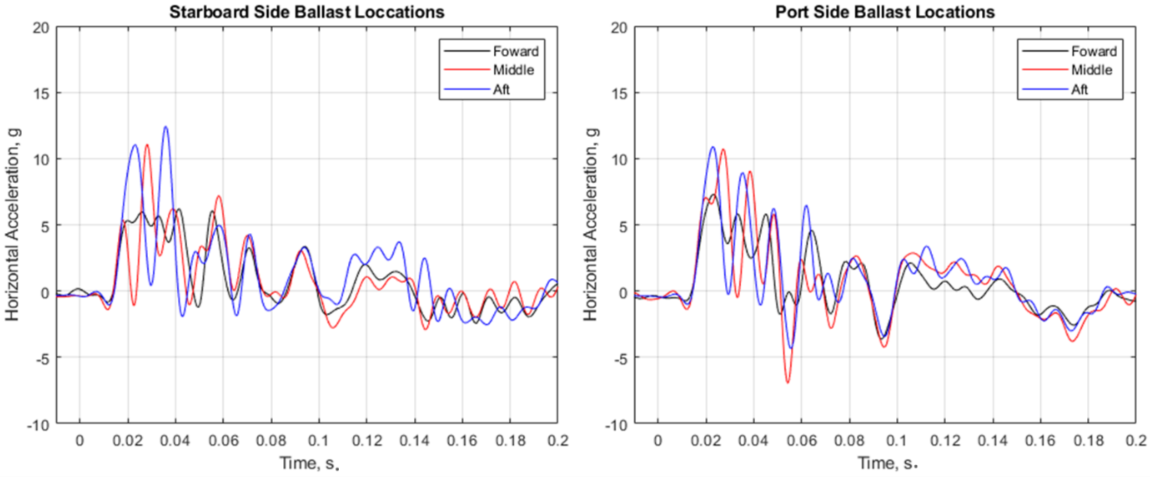

Figure 86 - Ballast horizontal acceleration location comparisons. Starboard side (left) and Port side (right).

Finally, the accelerations at the ceiling were investigated for the vertical direction. There are two plots shown in Figure 87. The left plot shows the ceiling location filtered in accordance with SAE J211, while the right plot shows the acceleration filtered with lower 60 Hz lowpass cutoff 4-pole filter. The ceiling acceleration data show large oscillations for all locations using the SAE J211 filtering guidelines. The pulse shape is difficult to interpret, so the data were additionally filtered with a 60 Hz lowpass filter. The resultant data still contains some of the oscillations, however it begins to resemble the pulse shape acquired from the ballast locations. The pulse shape is roughly trapezoidal with a duration of between 80 ms. and 100 ms. after impact. Peak values are acquired in the forward location and are 54.9 g in magnitude.

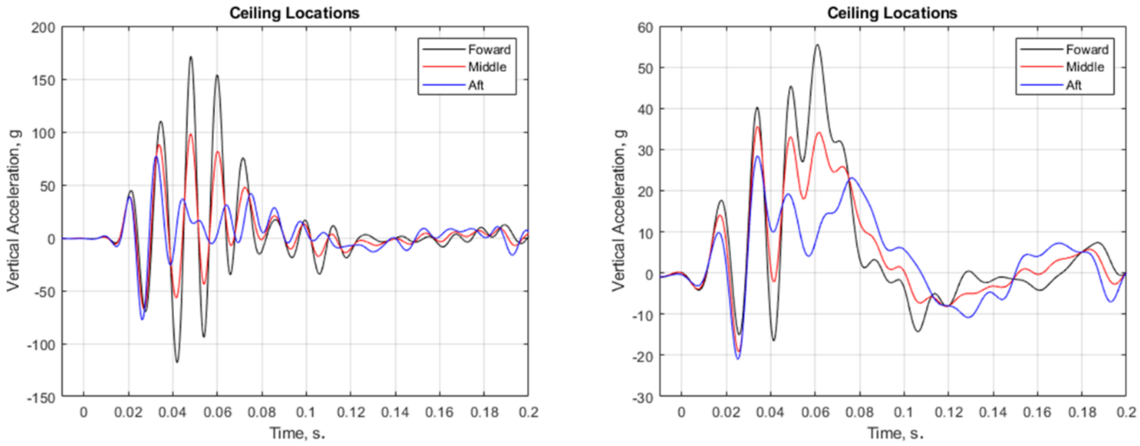

Figure 87 - Ceiling location comparisons. SAE J211 (left) and 60 Hz (right).

Following the full-scale drop test of the Aft Section, an additional post-test set of full-field 3D-DIC data were computed using the static post-test shape of the test article and comparing it to the undeformed pre-test shape, which was measured prior to the test. These two measurements were compared to each other and a delta displacement measurement, representing permanent deformation, was obtained. An example of this measurement is shown in Figure 88, for which the vertical direction deformation data are plotted.

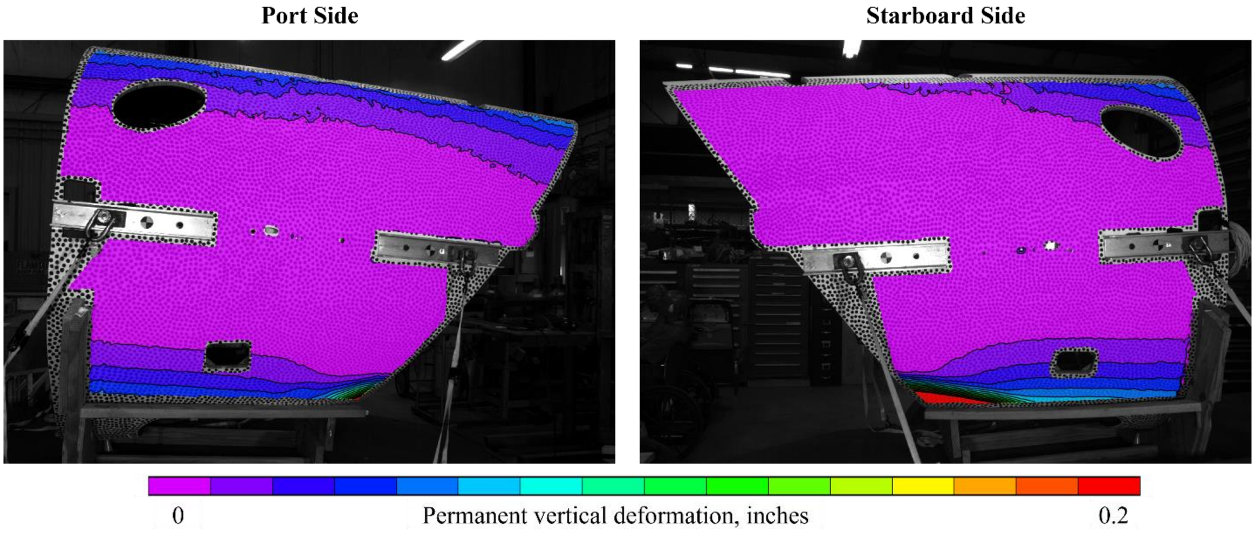

Figure 88 – Permanent vertical deformations. Port side (left) and Starboard side (right).

The permanent deformation in the vertical direction reveals two distinct items. The first is that there is a large amount of permanent vertical deformation in the aft belly area, which was the area that made first contact with the impact surface and experienced a large failure. The localization of the red also indicates that this permanent deformation is localized to the area immediately around the aft belly section. The second item to note is there is positive permanent vertical deformation at the top and bottom of the acquired data, while the mid-height area of the test article exhibits little to no permanent vertical deformation. This data indicates the test article experienced an elongation due to the flexing at impact from the test. The obtained data were very helpful because these types of deformations would not be readily apparent through normal post-test inspections and provided insight into the nature of the behavior of the test article during the test.

Post-test 3D point cloud scans were also conducted on the Aft Section, immediately following the drop test, to capture the final resting position of the test article, along with shape, deformation and damage, and are shown in Figure 89.

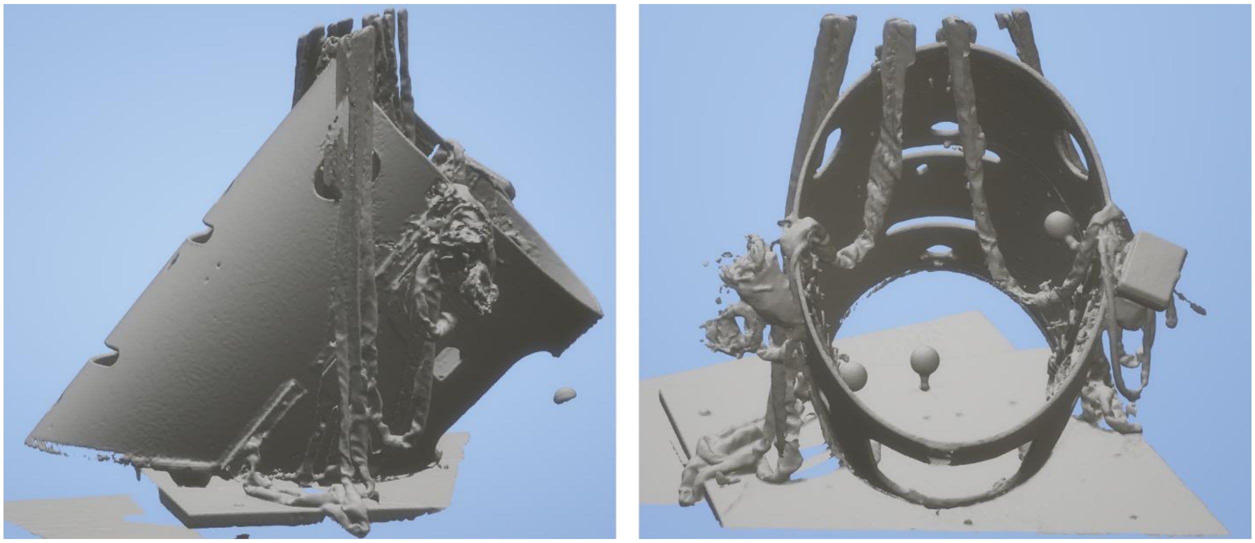

Figure 89 - Post-test 3D point cloud scan. Starboard side (left) and Forward (right).

## Full-Scale Simulations – Aft Section

After the Aft Section test, the FE model of the Aft Section was updated to match the as-tested configuration. The Aft Section test article included eight 25-lb. ballast blocks attached to aluminum c-channels mounted at the approximate center of the test article. The ballast mass was represented in the Aft Section FE model using point masses rigidly fixed to the composite sandwich elements through constrained CNRBs defined at the c-channel mounting locations. Representative belly and ceiling accelerometer models were fixed to the composite skin using CNRBs while the ballast accelerometer models were fixed to the ballast mass CNRBs. A schematic of the Aft Section test article with fixed mass and instrumentation is shown in Figure 90. The Aft Section test article weighed 490 lb. with all ballast mass and instrumentation included. The developed Forward Section FE model weighed 484 lb., closely matching the mass of the physical test article.

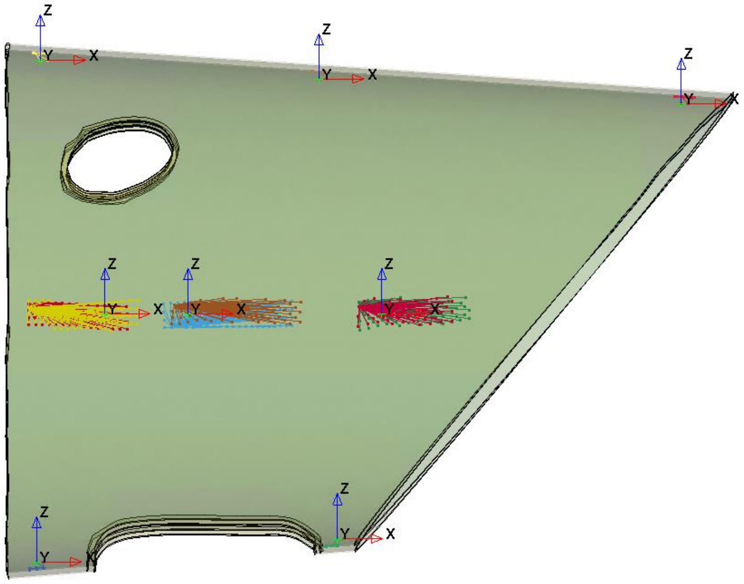

Figure 90 – Schematic of aft test article model showing instrumentation and mass CNRB locations.

The measured impact conditions of the aft test article were 26.7 ft./s. vertical velocity with a downward pitch of 17.9 degrees were applied to the Aft Section FE model in order to simulate the test. Simulation was conducted on a Linux computer cluster using LS-DYNA SMP version R13.10 single precision, as was done for the Forward Section simulation. Simulations were carried out to a termination time of 0.25 s. using eight processors. The aft test section model had an approximate run time of 3 hours. The Aft Section FE model took less time to simulate than the Forward Section FE model due to size differences of the models.

During impact, damage to the Aft Section test article composite structure along the impacting edge was observed. The center of the impacting edge showed delamination and brittle failure of the composite skin and sandwich material extending across the length of the structure in this area. Failure of the material along the length of the impacting structure caused the fuselage to fold inward at the failure point producing a distinct triangular shape. The inward folding also led to sandwich delamination along the width of the impacting edge of the fuselage. An image of the aft test model and test article peak deformation is shown in Figure 91. The composite failure of the impacting structure was predicted by the Aft Section FE model. The model predicted composite failure and sandwich delamination across the length of the impact region and accurately replicated the inward folding which resulted in the distinct triangular peak around the failure point.

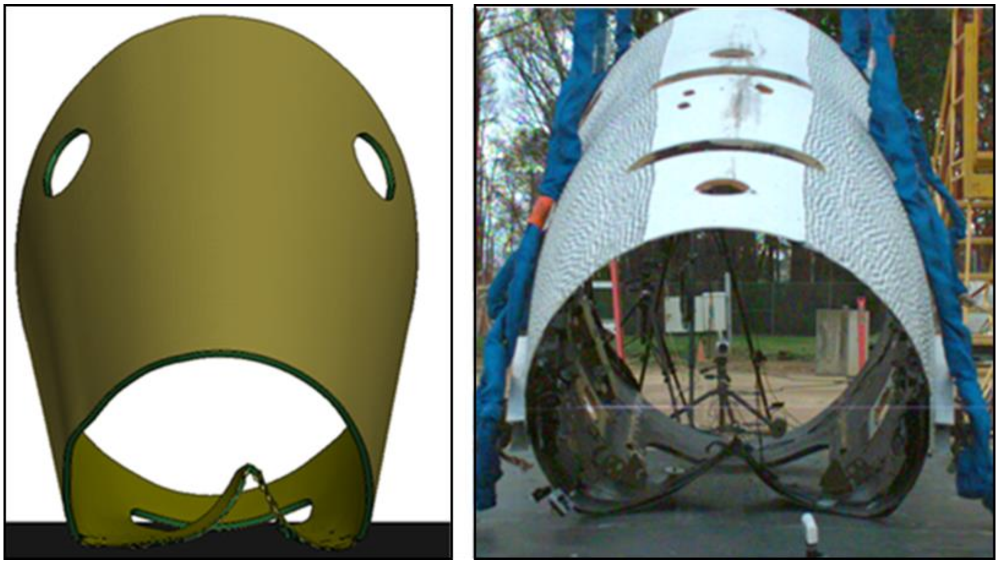

Figure 91 – Composite damage observed in Aft Section test article and predicted in Aft Section FE model.

Comparison of vertical displacement at peak deflection measured on the Aft Section test article and representative model is shown in Figure 92. The Aft Section FE model was found to predict similar vertical displacement to what was measured across the surface of the test article. Close prediction of structural displacement by the reverse engineered model corresponded with the accurate prediction of damage. Prediction of displacement across the compared surface also indicates realistic estimation of structural stiffness of the test article by the reverse engineered model.

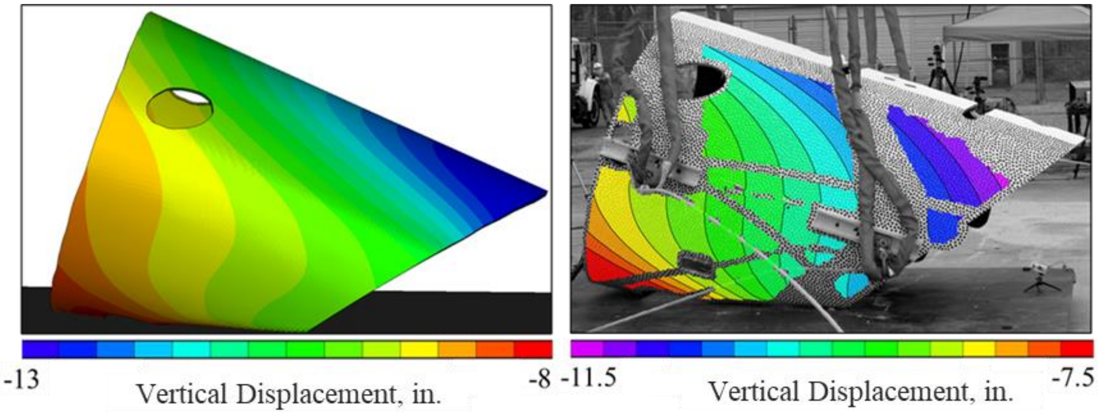

Figure 92 – Vertical displacement measured in Aft Section test article and predicted in the Aft Section FE model.

Horizontal acceleration time histories measured in test and predicted using simulation at the aft, middle, and aft ballast locations are shown in Figure 93. Acceleration shape and peak was well predicted across all ballast locations. The initial rise in horizontal acceleration was predicted in the forward and middle locations, while it was slightly underpredicted in the aft location. Outside of this underprediction in initial acceleration rise in the aft location, horizontal acceleration was closely predicted in the aft test article model. These results indicate effective representation of longitudinal stiffness within the model.

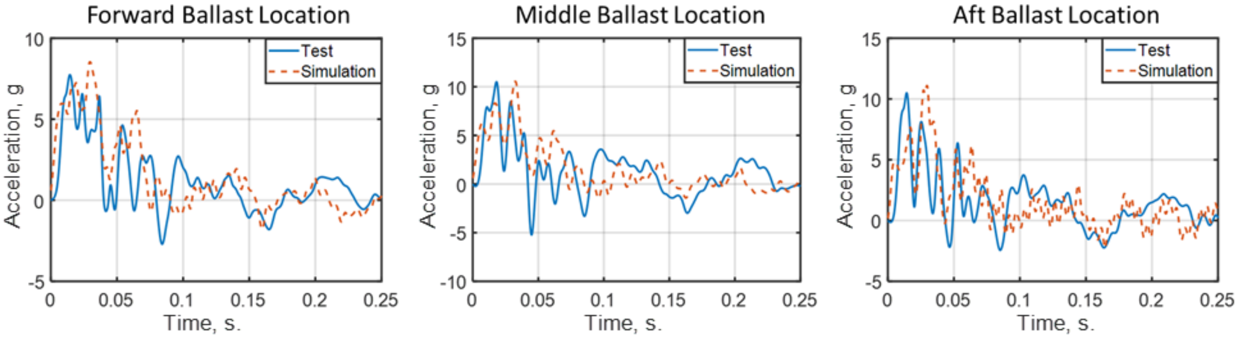

Figure 93 – Aft Section portside ballast horizontal acceleration time history comparisons.

Lateral acceleration time histories measured in test and predicted using simulation at the aft ballast location is shown in Figure 94. Lateral acceleration on the forward and middle ballast locations were not recorded during test. The lateral acceleration time history shape was closely predicted by the model. Interestingly, the aft test article did not experience the high oscillatory response in lateral acceleration which was observed in the Forward Section. Two acceleration peaks, one at the onset of impact and one at approximately 0.1 seconds was recorded. The simulation captures these two events thought it slightly underpredicts peak acceleration on initial impact.

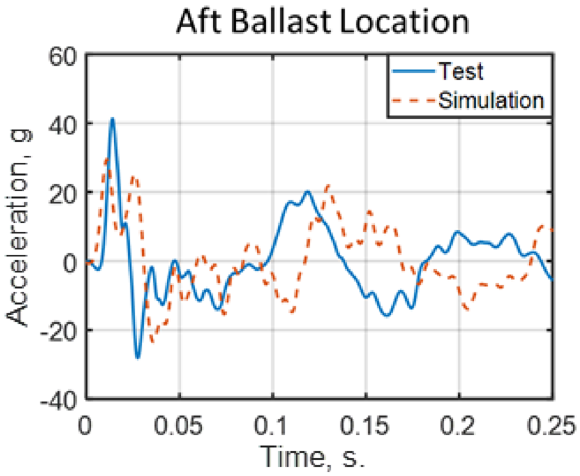

Figure 94 – Aft Section portside ballast lateral acceleration time history comparisons.

Vertical acceleration time histories measured in test and predicted using simulation at the forward, middle, and aft ballast locations are shown in Figure 95. Overall, the model predicted acceleration shape but underpredicted peak value in the vertical direction. Large oscillations in vertical acceleration, particularly towards the front of the test article, were measured in test which but were not captured by simulation. Lack of prediction of the acceleration oscillations resulted in the underprediction of peak acceleration. Because the oscillations diminished towards the aft end of the test article, the model more closely predicted acceleration in the aft location. Although peak vertical acceleration was not captured, the shape of the vertical acceleration pulse and timing of the pulse was accurately predicted.

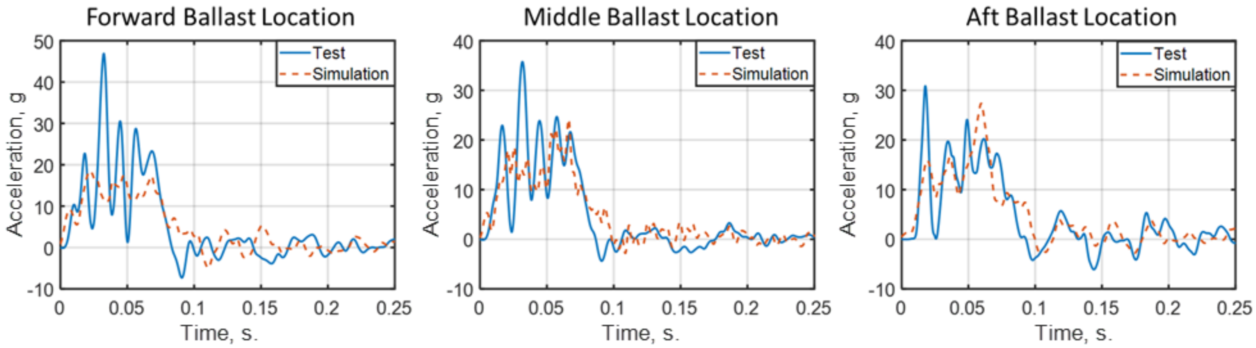

Figure 95 – Aft Section portside ballast vertical acceleration time history comparisons.

## Discussion

Testing of a partial Hawker 4000 fuselage was conducted to study the response of carbon composite aerospace structures in a dynamic loading environment and to characterize predictive capability of FE modeling techniques. Three test articles were created, two for full-scale dynamic impact testing and the third for material model characterization testing. The material model characterization test data were generated utilizing a building block approach to as much of an extent as possible. Care was taking in choosing the specimen designs and extracting them in order to acquire as much material property data and component level data as possible. The material property data were generated using the three-point bend tests of the flange specimens and the crush tests of the honeycomb core. Component level tests were conducted utilizing the static and dynamic three-point bend tests of the sandwich specimens. The full-scale tests were performed with impact conditions selected to induce damage in the composite structure and thus characterize composite failure under load and evaluate the capability of FE models to predict damage and identify effects of damage on overall structural response. Instrumentation and high-speed photogrammetry were used to measure accelerative loads, structural deformation, and damage progression during the full-scale tests. Each test was conducted successfully and all data necessary for FE model evaluations were recorded.

The FE models of the Forward and Aft Sections were developed using component tests and measurements of the test article without information from the fabrication process or manufacturer details. The model geometries were developed from 3D point cloud scans which resulted in inherent simplification of geometric detail. Component material testing performed on the test article allowed for in-depth material characterization. Material characterization testing led to the development of material models which were calibrated to predict component response through failure under both static and dynamic loading within the sandwich composite structure. Though the component material models were calibrated to test, detailed variations in the composite layup throughout the test article could not be replicated without manufacturer specification data. Because the developed model was generated through reverse engineering techniques conducted on the fully fabricated composite, the material models developed represented the response of the combined composite layup and not the constitutive material layers from which it was made. As such, the composite material models were not representative of specific fabric layers and thus could not replicate variations in composite structure across the test article surface. Lack of composite layup definition data did limit precision in replicating mass distribution and material stiffness variability through the structure.

The FE models were shown to predict the mechanism and location of the composite structural damage observed in both the Forward and Aft Section test articles. Prediction of damage in the Forward Section

FE model was limited by lack of prediction of the “w” shaped indention observed in test and prediction of more damage across the length of the fuselage floor. Increased damage prediction across the floor of the fuselage led to overprediction of peak vertical displacement of forward fuselage section. The Aft Section closely predicted the triangular shape of the damaged section and the extent of damage measured in test. Close prediction of damage extent led to close prediction of peak vertical displacement by the Aft Section FE model. Differences in the prediction of damage extent and resulting displacement in the Forward and Aft Section models in can be attributed to different effects of imprecision within the composite layup distributions between these two sections of the test article. Thus, the simplification of the composite skin as a single part in the reverse engineered models was more significant in the Forward Section.

Acceleration time history was well predicted by the Forward and Aft Section FE models. The models captured acceleration shape and peak acceleration in most locations across the length of the test article. The one consistent limitation of the acceleration predictions by the models was that initial the acceleration spike recorded in test was not consistently captured. Improved mass distribution and composite layup definition from manufacturer specifications would likely improve acceleration prediction in the reverse engineered models.

## Conclusion

The data generated in this report were a result of multi-year effort to acquire data on large scale composite aircraft structures. The data represented the form of material coupon and component level data, along with data from two full-scale dynamic impact drop tests. This data was successfully collected and satisfied the first objective of the research effort.

In addition to the composite material data generation effort, significant resources were expended in the development of large-scale composite FE models, which were utilized to evaluate the applicability and accuracy of using reverse engineered geometry and material property data in accurately capturing composite dynamic response. The model development did not include details which would require knowledge of the manufacturing design such as composite layup properties, detailed thickness variations and localized geometrical imperfections, but rather evaluated the structure more at the macro level using reverse engineered geometries and generalized material property data characterized through testing. Since the second objective of the research effort was to evaluate the applicability and accuracy of utilizing such techniques, care was taken to focus efforts in these areas.

Overall, the developed FE models of the Hawker 4000 fuselage were found capable of predicting general composite damage location and mechanism. The models were limited in their prediction of damage extent which is hypothesized to be driven by simplification of composite layup variation through the vehicle structure. The developed models were able to effectively predict peak accelerative loads measured within the vehicle cabin, which indicated effective representation of the structural stiffness within the model. This analysis demonstrates that the described reverse engineering process can generate an FE model of a composite fuselage structure that is capable of predicting structural damage and accelerative loads imparted to the occupant cabin within a crash loading environment. To produce a more refined prediction of composite damage extent within the structure, details on composite layup and material variation through the vehicle is needed.

The research presented and objectives noted can help in identifying the necessary parameters needed in capturing large-scale composite aircraft response undergoing dynamic loading conditions. As with many new aircraft designs now containing the majority of composite materials as their primary structure, knowledge on how the materials affect the aircraft's response to emergency events such as hard landings or crashes are critical in moving the knowledge base forward. The full-scale test and FE model data presented are intended to help further these efforts.

## References

1. Jackson, K.E. et al., "Impact Testing and Simulation of Composite Airframe Structures," NASA TM 2014-218169. February 2014.

2. Huber, M., "Hawker 4000," Business Jet Traveler. https://bjtonline.com/business-jet-news/hawker-4000-0 Accessed August 16, 2023.

3. Olivares, G. et al., "Crashworthiness by Analysis: Vertical Drop Test and Simulation of a Composite H4000 Fuselage Section," 9th Triennial International Fire and Cabin Safety Research Conference. Atlantic City, NJ. October 28-31, 2019.

4. Jackson, K.E. and Putnam, J.B., "Simulation of a Full-Scale Crash Test of a Fokker F28 Fellowship Aircraft," NASA TM 2020-220435. February 2020.

5. Putnam, J.B. and Littell, J.D., "Simulation and Analysis of NASA Lift Plus Cruise eVTOL Crash Test," Proceedings from the Vertical Flight Society 78th Annual Forum and Technology Display. West Palm Beach, FL. May 2023.
6. Society of Automotive Engineering, "J211-1 Instrumentation for Impact Test – Part 1 – Electronic Instrumentation," SAE International, 400 Commonwealth Drive, Warrendale, PA, 1995.